Non-magnetic Optical Metamaterials: Fundamentals and Applications

Leonid Alekseyev

A Dissertation
Presented to the Faculty
of Princeton University
in Candidacy for the Degree
of Doctor of Philosophy

Recommended for Acceptance
by the Department of
Electrical Engineering
Adviser: Evgenii Narimanov

May 2011

Abstract

The ability to manipulate light with materials has been a crucial component of technological progress, revolutionizing human existence in a countless number of ways. In the past decade, a new paradigm has emerged for controlling light-matter interactions: that of metamaterials. Unprecedented advances in micromanufacturing and computational techniques have allowed researchers to shape the electromagnetic response functions of materials by structuring them on the scale smaller than the wavelength of light. Optical characteristics thereby attained can transcend anything found in nature, leading to a host of unconventional and, potentially, technologically important phenomena. These include negative refraction, diffraction-free imaging, and cloaking.

In the present dissertation, we develop the subject of non-magnetic optical metamaterials. We show that many phenomena that were originally thought to require control over the magnetic response can be found in strongly anisotropic dielectrics where one of its principal components becomes negative. We discuss the design of such a response in artificial and natural materials and show that these structures often offer simpler manufacturing and lower losses compared to traditional metamaterial designs. At the same time, they show many unconventional optical properties owing to the unique form of the photonic density of states. We explain the implications of this phenomenon for electromagnetic wave propagation, and describe several devices enabled by such materials with numerous prospective applications in light guiding and confinement, imaging, control of dipole emitters, and optical detection.

Acknowledgements

Acknowledgements.....

Contents

Abstract iii

Acknowledgements iv

1 Introduction **1**

1.1 Why metamaterials? 1

1.2 History of metamaterials 3

1.3 The quest for optical metamaterials 5

1.4 Nonmagnetic metamaterials 7

2 Hyperbolic metamaterials **9**

2.1 Introduction 9

2.2 Emergence of negative refraction from strong anisotropy 12

2.3 Possible implementations 20

2.3.1 Natural anisotropy 20

2.3.2 Artificial nanostructured systems 23

2.4 Conclusion 37

3 Hypersingularity **38**

3.1 Introduction 38

3.2 The hyperlens 39

3.2.1 Hyperbolic dispersion in cylindrical coordinates 39

3.2.2 Angular momentum states as information channels 43

3.3 Emergence of broadband singularity 45
3.4 Radiative decay engineering 47
3.4.1 Introduction 47
3.4.2 Radiative lifetime and spontaneous decay rates: general theory 47
3.4.3 Dipole lifetime near an interface: effects of metals, dielectrics, and hyperbolic materials 50
3.4.4 The role of geometry: dipole lifetime near waveguides 53
3.5 Conclusion 55

4 Guided waves in hyperbolic metamaterials 57
4.1 Introduction 57
4.2 Mirror waveguide 58
4.3 Planar dielectric waveguides and slow light 64
4.3.1 Dielectric waveguide basics 64
4.3.2 Slow light in TM modes using ϵ anisotropy 65
4.3.3 Slow light in TE modes using μ anisotropy 70
4.3.4 Slow light in hyperbolic bilayers 71
4.4 Hyperbolic slabs and imaging 74
4.5 Conclusion 78

5 Subwavelength resolution: alternative approaches 79
5.1 Introduction 79
5.2 Super-resolution via scattering on phonons 82
5.2.1 Motivation 82
5.2.2 Proposed setup 84
5.2.3 Mathematical description 85
5.2.4 Reconstruction of the input spectrum via iterative computation 88
5.2.5 Limitations of the iterative computation method 89

5.2.6 Differential detection 92
5.2.7 Reconstruction of the input spectrum with a secondary optical signal 94
5.2.8 Some practical considerations 96
5.2.9 Potential further improvements of the setup 98
5.3 Optical fingerprinting beyond the diffraction limit 99
5.3.1 Motivation 99
5.3.2 Proposed setup 100
5.3.3 Solving the scattering problem in the Born approximation . . 101
5.3.4 Simulation results 117
5.4 Conclusion 118

6 Conclusion **120**

A Reflection and transmission of dipole radiation **124**
A.1 Field of an electric dipole 124
A.1.1 Space domain 124
A.1.2 Spatial frequency domain 126
A.2 Reflection and transmission of dipole radiation 130

B Dirac trick **134**

C Transfer matrix formalism for the slab lens problem **136**
C.1 Transfer matrix analysis 136
C.2 Superlens and its limitations 140

Bibliography **144**

Chapter 1

Introduction

1.1 Why metamaterials?

The art and science of optics is centered upon our ability to control the dielectric response of materials, thereby directing the flow of light. From the stained-glass windows of Gothic cathedrals to modern LCD projectors, from Galileo's telescope to modern optical communication systems, devices made possible by skillful manipulation of the refractive index have resulted in countless technological and cultural breakthroughs. Our ability to build these devices has always been a combination of both luck and ingenuity. Ingenuity is required to harness the power of electromagnetism and quantum mechanics for communications, imaging, machining, and a myriad of other applications. Indeed, is it not a testament to human cleverness that we are able to create strands of silica thinner than human hair and many kilometers long, as well as all the hardware required to transmit and receive vast quantities of information at terabit rates? And yet, the whole endeavor might have been moot if we did not have the good luck of finding a material that only absorbs 0.2 dB/km (at a wavelength of 1.55 μm) – and is amenable to being drawn into a fiber. Likewise, in laser sources (particularly, before the advent of tunable semiconductor lasers), we

have had little control over the emission wavelength, relying instead on the abundance of various dielectric and semiconductor crystals we find in nature to provide us with something that will produce light at the frequency of interest.

It has been realized long ago that while the optical response of naturally occurring materials is, in principle, fixed, it is possible to alter this response by combining and processing materials. By using composites it is possible to remove some of the elements of luck from the spectral dependence of absorption and scattering and make these phenomena more controllable. Stained glass windows, dating back to the middle ages, serve as one of the earliest examples of this approach. Present-day advances include complex heterostructures used in the fabrication of quantum cascade lasers, as well as various photonic bandgap devices.

A little more than a decade ago, a new set of techniques for customizing material response burst onto the scene, quickly captivating the minds of researchers, science journalists, funding agencies, and prospective graduate students. In short order, these techniques grew into a full-fledged field under the name of metamaterials research. The term *metamaterials*, without a formal definition, first appears in a paper by Smith et al. [1] which presented the first realization of a composite medium with simultaneously negative permeability and permittivity. Because of this context, the name metamaterial became firmly attached to the medium with $\{\epsilon < 0, \mu < 0\}$-type response (also called a double negative, or DNG material). This definition later broadened to include all media deriving their macroscopic optical properties from an artificial subwavelength structure (note that such terminology specifically excludes photonic crystals, which operate via Bragg reflection and must therefore be patterned on the scale of optical wavelength). Operationally, however, metamaterials often became a catch-all term, referring to all artificial media with unusual electromagnetic properties.

Regardless of the definition one chooses to use, the reason to study metamaterials is clear: their development opens many new chapters in the fields of optical physics and device engineering. It does so by greatly expanding parameter space accessible for manipulating light, potentially paving the way for devices with unprecedented capabilities – for example, imaging systems with subwavelength resolution, ultra-small waveguides, ultra-efficient energy concentrators, and may others. A no less significant reason to study metamaterials is simply the fact that the field provides a playground to explore many fun topics in physics, both classical and contemporary. Within the context of metamaterials one can reexamine and challenge mainstream interpretations of diffraction theory [2, 3, 4], study fields in curved spacetime, and contemplate black holes [5], quantum foams, and exotic metric signatures [6].

Let us now briefly review the recent history of metamaterials, and put in context the body of work presented in this thesis.

1.2 History of metamaterials

The many techniques of manipulating materials through doping, patterning, and creating structured composites has resulted in an impressive coverage of the electromagnetic parameter space. By the end of the 1990s, however, one area of that parameter space remained thoroughly unexplored, namely, the $\{\epsilon < 0, \mu < 0\}$ materials. The reasons for this are simple: first, negative magnetic response in the optical domain does not occur in nature, and second, materials with these parameters were not thought to have great technological importance. Nonetheless, it had been known for several decades that this particular combination of material parameters has some rather intriguing properties. Specifically, waves propagating through such medium have negative phase velocity, and undergo negative refraction at an interface with vacuum or an ordinary dielectric.

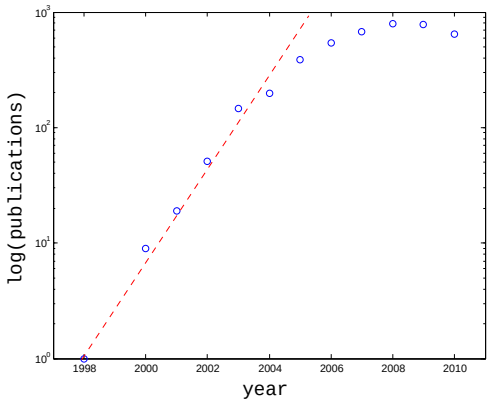

Figure 1.1: Number of research articles on negative refraction and metamaterials from 1998 to 2010 (semi-log plot). (Source: *ISI web of knowledge*)

In the early 2000s – the early years of metamaterials research – negative refraction had become the marquee property of these novel structures [2, 7, 8]. As a result, it may seem to be a decidedly 21st century research area; however, we must recognize that the origins of the subject date back many decades. Indeed, as a general wave propagation phenomenon, negative refraction has been known since the early 1900s [9, 10]. It was noted, in particular, that negative refraction naturally occurs at the interface with a medium characterized by negative phase velocity. No such materials were known in the electromagnetic domain, and so the early discussions involved only mechanical oscillations. The first detailed treatment of negative refraction in electromagnetism was provided by Veselago in 1968 [11]. He showed that to attain negative phase velocity for EM waves, the material response must be of the form $\epsilon < 0$, $\mu < 0$. When this condition is satisfied, the $\boldsymbol{E}$, $\boldsymbol{H}$ and $\boldsymbol{k}$ vectors form a left-handed triplet. As a result, the wave vector $\boldsymbol{k}$ and the Poynting vector $\boldsymbol{S}$ are oriented in opposite directions: the system has negative phase velocity, the condition for negative refraction. Indeed, negative phase velocity serves as a definition of negative index materials [12]. While mechanical and radio frequency devices exhibiting such effective negative indices were known at the time of Veselago's writing, bulk materials with negative phase velocity were not found in nature and not readily attainable [12].

Veselago's discovery remained a forlorn electromagnetic curiosity until the year 2000, when interest in negative refraction and related phenomena experienced a major surge, owing to major theoretical and experimental advances. On the theoretical side, Pendry has proposed negative refractive media as a platform for subwavelength resolution and aberration-free imaging [2]. In particular, Pendry showed that a slab of Veselago's "left-handed" material with $\epsilon = \mu = -1$ acts as a perfect lens: it does not suffer from aberrations and is not subject to the diffraction limit. The proposed "superlens" stimulated enormous interest in negative index materials, but generated some initial controversy regarding their experimental realizability [13, 14]. This controversy was soon resolved by Smith and colleagues, who fabricated a material with $\epsilon < 0$, $\mu < 0$ in the microwave band and explicitly demonstrated negative refraction [15] These early studies sparked an explosive interest in metamaterials, and for the first seven years, the number of research papers published in this area grew exponentially, doubling approximately every ten months (Fig. 1.1). This is not surprising, as many avenues of exploration laid wide open. First, of course, was the problem of designing custom macroscopic electromagnetic response by controlling the local response of micro- and nanostructured assemblies. In addition, many results in the optical sciences, accumulated over centuries, could be adapted to accommodate the newly available set of material parameters, sometimes leading to surprising new results. Finally, the complete freedom to manipulate material response functions created entirely new research directions, such as transformation optics and electromagnetic cloaking [16, 17, 18].

1.3 The quest for optical metamaterials

The most exciting prospective applications of metamaterials lie in the optical domain. As a result, much effort has been directed into bringing their operating wavelengths

ever lower, from centimeters in early 2000s [15], to the infrared range in 2005 [19, 20], to visible in 2007, when negative refraction was demonstrated experimentally for wavelengths as short as 772 nm [21].

Despite the tremendous advances in nanofabrication techniques that made those experiments possible, manufacturing metamaterials that exhibit negative refraction and related phenomena at such high frequencies presents many difficulties. The most challenging aspect of the engineered electromagnetic response is the required negative magnetic permeability. Negative permeability is a result of a resonant response by a miniature conductive structure. For an effective negative permeability response, these micro-resonators must reside in subwavelength unit cells. Thus, to attain negative permeability for THz and higher frequencies, one must resort to lithographic methods in structuring the materials. For the optical frequencies, fully three-dimensional subwavelength patterning is currently unfeasible.

Aside from the manufacturing difficulties, negative magnetic response presents another significant challenge. The resonance in the real component of magnetic permeability which leads to negative values of μ is necessarily accompanied by a spike in its imaginary component. This leads to high absorption at the operating frequencies of magnetic negative index metamaterials, which can significantly impair device performance [22].

In the quest to minimize losses, it became prudent to examine ways of obtaining negative refraction without resorting to optical magnetism. Several groups showed that negative refraction can arise for light in suitably designed photonic crystals [23, 24, 25, 26]. From the standpoint of losses, photonic crystals are generally superior to magnetic metamaterials [26]. However, photonic bandgap devices present many of the same fabrication challenges as magnetic metamaterials, especially for 3D structures. While the characteristic features of photonic crystals are simpler and larger (and

hence easier to produce), the photonic band behavior is strongly sensitive to disorder, necessitating high manufacturing precision.

1.4 Nonmagnetic metamaterials

In the present thesis, we address the issues of designing and studying metamaterials which do not exhibit optical magnetism. Although $\{\mu < 0\}$-type response has attracted the most attention in the early years of metamaterials research, it is only one out of a multitude of available (and potentially controllable) material parameters. Indeed, the most general formulation of linear electromagnetic material response has 36 complex scalar constitutive relations [27] (18 of which come from the tensor nature of ϵ and μ in crystals, and the other 18 characterize *bianisotropic* materials, where electric fields can induce magnetic response and vice versa). Given this large parameter space, it is not surprising that only certain parts of it had been thoroughly explored by studying naturally-occurring materials. For example, uniaxial dielectric anisotropy is a common phenomenon, mentioned in every introductory optics textbook, and having important technological applications (e.g. angle-tuning of refractive index in nonlinear devices). In studying uniaxial crystals, the usual assumption had been that the dielectric tensor is positive definite. Even after the negative values of ϵ and μ made the headlines, it took several years for researchers to start exploring materials in which one of the components of the dielectric tensor had a negative sign [28, 29, 30, 31]. Such materials were known as *indefinite media* [29] in some early works. We prefer to call them *hyperbolic media*, or hyperbolic metamaterials (HMMs) (this terminology comes from the fact that the wave vector surfaces in such materials form hyperboloids).

Hyperbolic metamaterials have many appealing properties. First, they are vastly simpler than typical magnetic metamaterials, and are therefore potentially more

amenable to bulk fabrication. For certain frequencies, materials with the desired hyperbolic anisotropy can even be found in nature [30]. Additionally, hyperbolic materials are not sensitive to disorder and operate far from resonances, thus helping minimize absorption losses.

HMMs were originally introduced as a way to achieve all-angle negative refraction without resorting to optical magnetism. Since then, it has been shown that many other effects originally studied in $\{\epsilon < 0, \mu < 0\}$ metamaterials can be reproduced in hyperbolic materials. These include negative phase velocity waveguides [32, 33], negative Goos-Hänchen shift [34], and subwavelength focusing [4, 33]. But HMMs turned out to have unique properties that put them in a metamaterial league of their own. These properties originate in the unbounded nature of the hyperbolic wave vector surfaces, which fundamentally changes certain aspects of light propagation in HMMs and leads to an entirely new class of exciting devices.

The work described in this thesis is, for the most part, dedicated to exploring the physics and applications of hyperbolic metamaterials. In Chapter 2 we describe in detail the role of anisotropy in creating all-angle negative refraction and discuss natural and artificial materials that can be used to demonstrate this phenomenon. We proceed, in Chapter 3, to study the deep physical implication of the unbounded wave vector hyperboloids: a diverging photonic density of states. This *hypersingularity* can be exploited to create *the hyperlens* – a novel device that enables far-field subwavelength-resolved imaging – and to control the lifetime of an emitter, thereby enabling a sort of cavity-less Purcell effect. Chapter 4 describes further potential applications of HMMs, including negative phase velocity waveguides, slow light waveguides, and planar imaging devices. Finally, in the last chapter, we broaden our discussion of subwavelength imaging and describe nanophotonic devices which use subwavelength structure for optical detection and fingerprinting significantly below the diffraction limit.

Chapter 2

Hyperbolic metamaterials

2.1 Introduction

The tremendous upsurge of interest in Veselago's theory of left-handed materials in the late 1990's – early 2000's was driven primarily by two factors. First was the realization that artificial magnetism may be attainable at frequencies approaching optical. The second factor was the theoretical discovery of new effects associated with left-handed propagation, some of which could have a disruptive technological impact (superlensing being the prime example) [2]. Much effort was concentrated on achieving high-frequency magnetic response. This is a non-trivial task; in fact, the conventional wisdom (supported by none other than Landau and Lifshitz in their classic textbook) suggests that at optical frequencies we must always put $\mu = 1$. Indeed, for an isotropic medium, the magnetic susceptibility is defined (in cgs units) as

$$\mu = 1 + 4\pi \frac{|\boldsymbol{M}|}{|\boldsymbol{H}|}, \tag{2.1}$$

with $\boldsymbol{M}$ ordinarily interpreted as magnetic moment per unit volume. It can be argued that at optical frequencies, this concept loses its meaning and we are justified in ignoring $\boldsymbol{M}$ [35]. However, such arguments typically assume non-exotic natural

materials with diamagnetic susceptibility. For metamaterial composites, especially the ones involving high-permittivity inclusions, these conclusions need to be reexamined [36]. One finds that magnetic response at optical frequencies is, in fact, a meaningful concepts in such materials. On the other hand, relating this response to the usual macroscopic material parameter $\mu(\omega)$ may be nontrivial.

In 2004, Agranovich et al. pointed out that wave propagation in media, both linear and nonlinear, can be fully described without explicitly mentioning the magnetic permeability μ or the field $\boldsymbol{H}$. The only constitutive relation needed was

$$\boldsymbol{D} = \tilde{\epsilon}(\omega, \boldsymbol{k})\boldsymbol{E}, \tag{2.2}$$

where the generalized dielectric tensor $\tilde{\epsilon}(\omega, \boldsymbol{k})$ contains the effects due to bound currents that are normally associated with magnetic response. This description has a one-to-one correspondence with the conventional treatment of waves in media, but the resultant equations only contain the fields $\boldsymbol{E}, \boldsymbol{D}$, and $\boldsymbol{H}$; in addition, μ appears nowhere except, possibly, the definition of $\tilde{\epsilon}$. This description necessarily forces $\tilde{\epsilon}(\omega, \boldsymbol{k})$ to be anisotropic and spatially dispersive [37]. Agranovich et al. were able to use the generalized dielectric tensor to describe $\{\epsilon < 0,\ \mu < 0\}$ materials at optical frequencies, where the traditional physical meaning of $\mu(\omega)$ becomes unclear. This approach retains its power even when no magnetic dipole type response takes place in the medium [38].

The notion that it is possible to formally substitute magnetic response of the medium with a more complicated dielectric response stimulated further research. In particular, it motivated Podolskiy and Narimanov to come up with an example of a system that mimicked, mathematically, the dispersion relation of a Veselago $\{\epsilon < 0, \mu < 0\}$ medium by exploiting dielectric anisotropy. This was achieved by considering a metallic waveguide with a uniaxial anisotropic core: the material re-

sponse was different along the waveguide and perpendicular to it. This is a quasi-two-dimensional system with the wave vector confined to the waveguide plane. It is straightforward to show that the relation between this wave vector's magnitude and frequency is given by

$$|k| = \sqrt{\epsilon\nu}\frac{\omega}{c}, \tag{2.3}$$

where ν is a function of $\boldsymbol{\epsilon}$ and waveguide parameters. For the TM modes, propagation is possible for $\{\epsilon, \nu\} < 0$. Furthermore, it was shown that the phase and group velocity have different signs and that if an interface were set up between some isotropic dielectric and the uniaxial medium inside the waveguide, negative refraction would arise [30].

This was not the only motivation that guided researchers towards considering anisotropic effects. Around roughly the same time, several groups were working on improving the performance of Pendry's "poor man's" superlens – a non-magnetic metallic slab with $\epsilon < 0$ which amplifies evanescent waves via plasmon coupling. Any realistic device, however, suffers from significant losses. It turns out that these losses can be decreased while retaining the superlens resolution by replacing the metallic slab with a metal-dielectric stack [39, 40]. Such a configuration is, effectively, an anisotropic uniaxial form-birefringent crystal.

Finally, based on simple geometrical arguments, several other groups realized that negative permittivity in uniaxial crystals along the anisotropy axis leads to backwards waves and negative refraction [28, 29, 31].

It became clear that a special kind of anisotropy, where one sign of the dielectric tensor is negative, zero, or infinity, started to emerge as a solution to a diverse range of problems in metamaterials research. This raises several natural questions: what particular features make these materials so appealing, and how do we go about the practicalities of obtaining them?

In this chapter, we will examine the role of strongly anisotropic metamaterials in enabling negative refraction and related phenomena. We will see that much can be understood simply by examining the shape of isofrequency curves as a function of wave vector components.[1] Crucially, we will see that the hyperbolic form of the dispersion relation is central to facilitating unconventional optical behavior. After describing the various aspects of negative refraction and wave propagation enabled by hyperbolic dispersion, we turn our attention to the realizability of the desired dielectric response in natural or artificial materials. We finish by describing two specific artificial metamaterial system with hyperbolic anisotropy that were studied experimentally. The results of these experiments closely match theoretical predictions made for hyperbolic metamaterials in the framework of the effective medium approximation.

2.2 Emergence of negative refraction from strong anisotropy

For a plane wave with wave vector $\boldsymbol{k}$, incident on some surface, translational invariance demands that $k_{\|}$, the component of $\boldsymbol{k}$ along the surface, be preserved for the refracted wave. So long as the direction of the energy flow (given by the Poynting vector $\boldsymbol{S}$) and the direction of the wave vector $\boldsymbol{k}$ are the same, negative refraction cannot occur. Thus, negative refraction is only possible in media where the unit vectors $\hat{\boldsymbol{k}}$ and $\hat{\boldsymbol{S}}$ do not coincide. More specifically, for the transmitted wave we must have $S_{\|} < 0$ when $k_{\|} > 0$ and vice versa. For a medium with negative phase velocity, $\hat{\boldsymbol{S}} = -\hat{\boldsymbol{k}}$ holds, and the condition $S_{\|} < 0$ and $k_{\|} > 0$ are then satisfied automatically. Material parameters $\epsilon < 0$, $\mu < 0$ lead to exactly this scenario. More generally, however, we

[1] Since such plots are simply a representation of the dispersion relation, i.e. the $\omega(\boldsymbol{k})$ dependence, we will most often use the term "dispersion" to characterize functional form of these isofrequency curves (as opposed to e.g. spectral dependence of material response).

may inquire what material parameters lead to negative refraction without requiring negative phase velocity.

The simplest answer to this question comes from considering wave propagation in anisotropic crystals and noting that the directions of $\boldsymbol{S}$ and $\boldsymbol{k}$ are, generally, different. To see how this comes about, we consider plane wave propagation in a uniaxial medium. Depending on polarization, the waves can be characterized as *ordinary* or *extraordinary*. For extraordinary waves, the electric field vector has a non-vanishing component along the optical axis, and therefore the different components of the electric field $\boldsymbol{E}$ experience different dielectric constants. Furthermore, the relationship between $\boldsymbol{E}$ and $\boldsymbol{D}$ (the electric displacement vector) depends on the propagation direction. Ordinary waves, on the other hand, are not affected by the anisotropy and are of no special interest. For this reason, in the subsequent discussion we treat only the extraordinary polarization.

Taking $\hat{\boldsymbol{x}}$ as the direction of the optical axis, we may characterize the extraordinary wave in a uniaxial crystal by the dispersion relation[35]

$$\frac{k_x^2}{\epsilon_z} + \frac{k_{y,z}^2}{\epsilon_x} = \frac{\omega^2}{c^2}. \tag{2.4}$$

For sufficiently weak absorption, the direction of the Poynting vector is identical to the direction of the group velocity vector $\boldsymbol{v}_g = \nabla_{\boldsymbol{k}}\omega(\boldsymbol{k})$ [35]. This means that $\boldsymbol{S}$ is normal to the isofrequency curves given by Eq. (2.4).

What does this imply for the relative angle between $\boldsymbol{S}$ and $\boldsymbol{k}$? In the isotropic case, the wave vector surfaces are spheres, and therefore $\boldsymbol{S} \propto \nabla_{\boldsymbol{k}}\omega(\boldsymbol{k}) \propto \boldsymbol{k}$, i.e. $\boldsymbol{S}$ and $\boldsymbol{k}$ are collinear, as can be seen in Fig. 2.1(a). Consider now the situation in Fig. 2.1(b), where $\epsilon_x \neq \epsilon_z$ and $\epsilon_{x,z} > 0$. The wave vector surfaces become ellipsoidal; as a consequence, the angle between $\boldsymbol{S}$ and $\boldsymbol{k}$ is non-zero; its exact value depends on the direction of propagation and the degree of anisotropy.

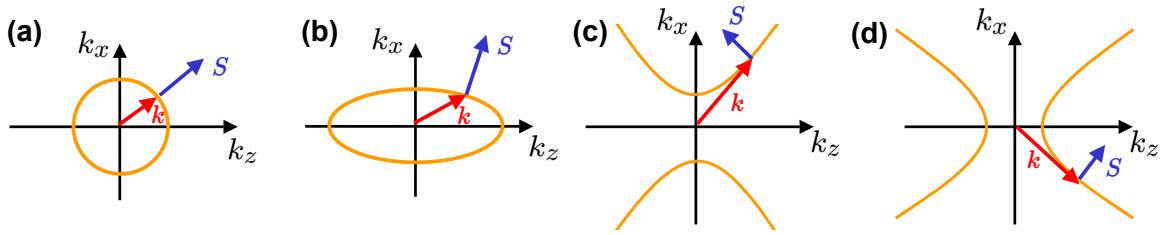

Figure 2.1: Isofrequency curve and relative direction of the wave vector $\boldsymbol{k}$ and the Poynting vector $\boldsymbol{S}$ for (a) isotropic material, (b) material with $\epsilon_x, \epsilon_z > 0$, (c) material with $\epsilon_x < 0$, $\epsilon_z > 0$, (d) material with $\epsilon_x > 0$, $\epsilon_z < 0$.

Finally, we consider the cases shown in Fig. 2.1(c,d), where ϵ_x and ϵ_z are not only non-equal but also possess different *signs*. This drastically changes the nature of the dispersion relation in Eq. (2.4), which we can now write, explicitly, as

$$\frac{k_x^2}{\epsilon_z} - \frac{k_{y,z}^2}{|\epsilon_x|} = \frac{\omega^2}{c^2} \tag{2.5a}$$

$$\frac{k_{y,z}^2}{\epsilon_x} - \frac{k_x^2}{|\epsilon_z|} = \frac{\omega^2}{c^2}, \tag{2.5b}$$

depending on *which* sign is taken to be negative.

For a material with negative transverse dielectric permittivity ($\epsilon_x < 0$) and positive in-plane permittivity ($\epsilon_z > 0$), Eq. (2.5a) describes a hyperbola with foci on the k_x axis. Constructing the vectors $\boldsymbol{S}$ and $\boldsymbol{k}$, as before, we see that the signs of S_z and k_z are opposite for all admissible values of $\boldsymbol{k}$.

This result can also be obtained by directly examining the expression for the Poynting vector of the extraordinary (TM) wave. The magnetic field for the TM wave is

$$\boldsymbol{H}(\boldsymbol{r}) = -H_0 e^{i\boldsymbol{k}\cdot\boldsymbol{r}}\hat{\boldsymbol{y}}, \tag{2.6}$$

and using the familiar expressions $\boldsymbol{\nabla} \times \boldsymbol{H} = -i\omega\boldsymbol{\epsilon}\boldsymbol{E}$ and $\boldsymbol{S} = \frac{1}{2}\boldsymbol{E}(\boldsymbol{r}) \times \boldsymbol{H}^*(\boldsymbol{r})$, we obtain

$$\boldsymbol{S} = \frac{H_0^2}{2\omega\epsilon_0} \begin{pmatrix} k_x/\epsilon_z \\ 0 \\ k_z/\epsilon_x \end{pmatrix}. \tag{2.7}$$

Evidently, if $\epsilon_x < 0$, S_z is negative, i.e., opposite to the direction of the wave vector component k_z.

What about the dispersion relation of Eq. (2.5b)? It also describes a hyperbola, but with a different orientation. We illustrate this other type of hyperbola in Fig. 2.1(d). As expected, the mathematical properties of this curve are nearly identical to the one in panel (c); the angle between the $\boldsymbol{k}$ and $\boldsymbol{S}$ vectors behaves in the same manner. The major difference arises when we consider refraction at an interface between a dielectric and a material exhibiting this kind of dispersion. Letting k_x be the normal to the interface, we can see that this configuration does not imply negative refraction – but due to the conservation of energy flux, it implies negative phase velocity in the hyperbolic medium. It is worth pointing out that the notion of negative phase velocity in this situation arises due to the fact that the preferred propagation direction in this system was chosen to be along the x axis (normal to the interface). We will see in Chapter 4 a different situation, where due to a different choice of system geometry and the "preferred" propagation direction, the negative phase velocity phenomenon in uniaxial dielectrics is associated with the dispersion relation of Fig. 2.1(c).

In Fig. 2.2 we compare refractive behavior originating from the different types of dispersion relations. Panel (a) illustrates the usual refraction at a dielectric interface; panel (b) shows the case of perfectly impedance-matched $\{\epsilon < 0, \mu < 0\}$ medium. Panels (c) and (d) show the two types of hyperbolic negative refraction corresponding to the dispersion curves of Fig. 2.1(d) and (c) respectively. The large angle between

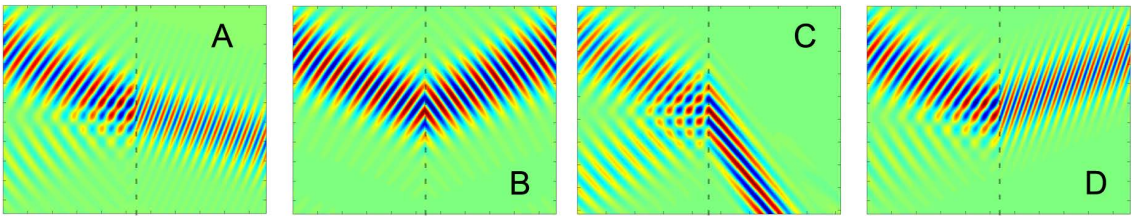

Figure 2.2: The different of refractive behavior corresponding to different types of materials: (a) the usual refraction at a dielectric interface; (b) negative refraction with impedance-matched $\{\epsilon < 0, \mu < 0\}$ medium; (c) $\{\epsilon_x > 0, \epsilon_z < 0\}$ material: positive refraction of the beam, negative refraction of the wavefronts; (d) $\{\epsilon_x < 0, \epsilon_z > 0\}$ material: negative refraction of the beam, positive refraction of the wavefronts.

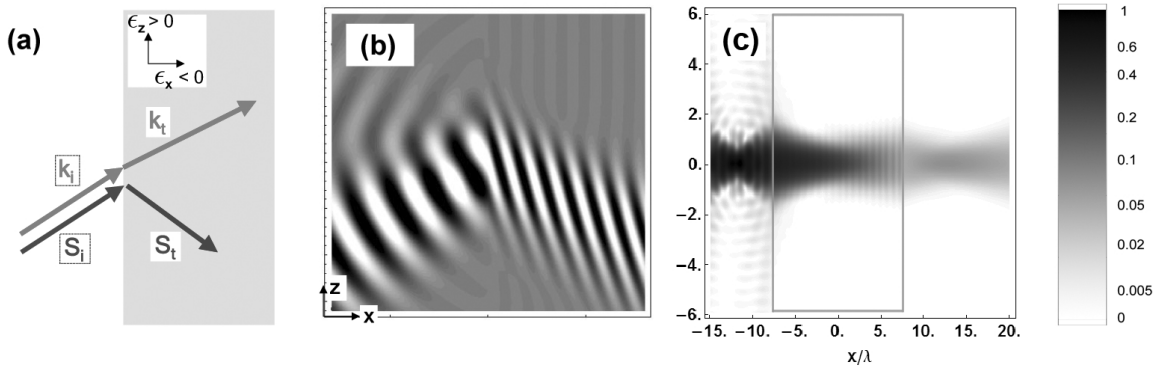

Figure 2.3: (a) The ray diagram and (b) the electric field for the refraction of a light beam at the boundary of air with an $\epsilon_x < 0$, $\epsilon_z > 0$ material ($\epsilon_z = 3$, $\epsilon_x = -1.5$). Note negative refraction of the beam and the direction of the wavefronts. (c) The intensity distribution of a beam propagating through a slab made of such material. Here, we use a particular example of an artificial layered metamaterial (SiC/SiO_2 stack) and realistic losses are considered.

the phase fronts and the direction of energy flow can be clearly seen in the plots. Furthermore, it can be seen that the $\{\epsilon_x > 0, \epsilon_z < 0\}$ anisotropy leads to the positive refraction of the beam, but the apparent negative refraction of the phase fronts.

Finally, in Fig. 2.3(c), we simulate the behavior of a strongly diverging beam impinging on a slab with $\{\epsilon_x < 0, \epsilon_z > 0\}$ anisotropy. Each spatial frequency Fourier component of this beam undergoes negative refraction as described above [illustrated schematically in panels (a) and (b)]. As a result, the material slab can function as a planar lens – an application that was originally heralded for the $\{\epsilon < 0, \mu < 0\}$ ma-

terials. The system illustrated here corresponds to an artificial layered material (see Sec. 2.3.2) made out of a SiC/SiO_2 stack, with realistic losses used in the simulation.

Two other aspects of the $\omega(\boldsymbol{k})$ dependence need to be considered: first, we were assuming that $\nabla_{\boldsymbol{k}}\omega(\boldsymbol{k}) > 0$. This determined the direction of the vector $\boldsymbol{S}$ (e.g., towards the inside of the hyperboloid sheets). This is the most common situation, but this need not always be the case. We can imagine a dispersive medium where increasing the frequency would shift the isofrequency contours towards *lower* values of k_x and k_z. In this case, we would have to flip the direction of the $\boldsymbol{S}$ vector in the diagrams of Fig. 2.1.

In addition, the interface between the media can be tilted with respect to the principal axes of one or both dielectric tensors. This implies that it is possible to pick a coordinate system $x'z'$ in which $S_{z'} < 0$, $k_{z'} > 0$. If the material is cut such that $\hat{\boldsymbol{x}}'$ defines the surface normal, negative refraction occurs. This situation is illustrated in Fig. 2.4(a). Note, however, that this arrangement, known as *amphoteric* refraction, is only realizable for a finite range of $\boldsymbol{k}$ values, and, hence, a finite set of incidence angles. Amphoteric refraction can be considered an intrinsic property of uniaxial crystals, and has been demonstrated experimentally [41, 42].

Beyond geometric optics: aspects of wave propagation in hyperbolic materials

The hyperbolic dispersion relation in Eq. (2.5) has a profound impact not just on refraction behavior at the interface, but also on the general properties of wave propagation. Indeed, one crucial difference between the curves of Fig. 2.1(a,b) and Fig. 2.1(c,d) is the fact that for the first two, corresponding to regular dielectrics, the domain of allowed $\boldsymbol{k}$ values is restricted. On the contrary, for hyperbolic materials, this domain is unbounded. The consequences of this on wave propagation can be immediately seen. Consider the propagation of a particular plane wave field

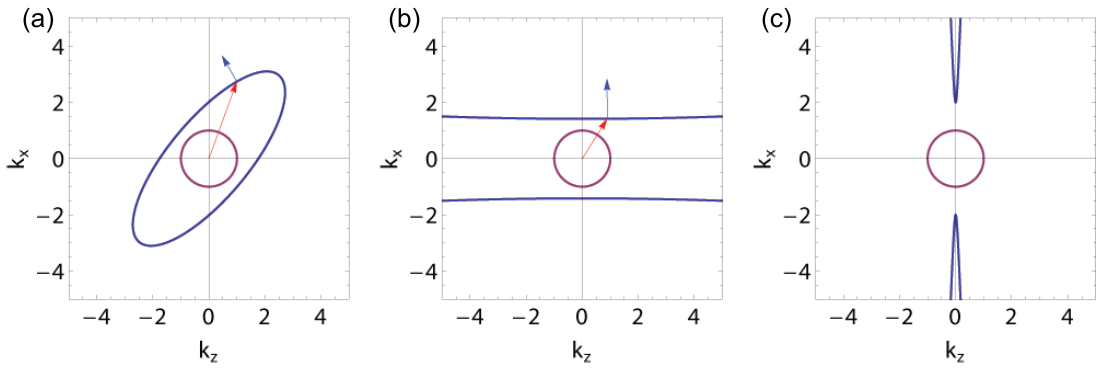

Figure 2.4: Special cases of negative refraction at an interface with an anisotropic medium: (a) amphoteric refraction; (b) channeling regime ($|\epsilon_x| \gg \epsilon_z$); (c) ENZ configuration ($|\epsilon_x| \ll \epsilon_z$). Wave vectors components $k_{x,z}$ are given in units of ω/c.

harmonic, which we write as

$$E(\boldsymbol{r}, t) = E_0 \exp\left[i(\boldsymbol{k} \cdot \boldsymbol{r} - \omega t)\right] = E_0 \exp\left[i(k_x x + k_z z - \omega t)\right], \tag{2.8}$$

where for simplicity we set $k_y = 0$. If we fix ω and k_z, we can easily find k_x from Eq. (2.4):

$$k_x = \sqrt{\epsilon_z \frac{\omega^2}{c^2} - \frac{\epsilon_z}{\epsilon_x} k_z^2}. \tag{2.9}$$

When k_z becomes too large (e.g. in the case of vacuum, when $k_z > \omega/c$), k_x becomes imaginary, and as a result the propagating wave in Eq. (2.8) decays exponentially in the x direction. This, indeed, is the origin of the diffraction limit. The upper bound that is set on the values of wave vector components determines the maximum frequency of spatial oscillations of propagating fields. This, in turn, determines the minimum length scale on which objects can be studied using electromagnetic wave propagation. It can be shown that these considerations imply the conventional $\lambda/2$ diffraction limit [43].

The above argument changes dramatically when the signs of ϵ_x and ϵ_z differ in Eq. (2.9). In this case, k_x remains real for arbitrarily high values of k_z — indeed, for

almost all values of k_z ($k_z < \epsilon_x\,\omega/c$ for the case $\epsilon_z < 0$ is the only exception). This suggests that in hyperbolic media the classical diffraction limit does not apply!

Another hyperbolic dispersion effect that is of particular interest in imaging applications involves directionality constraints on propagating radiation. Fig. 2.1(c) shows that the allowed directions of the wave vector and the Poynting vector are restricted by the asymptotes of the hyperbola. The locus of the allowed $\boldsymbol{S}$ vectors is a cone, with the half-angle θ_c given by

$$\tan\theta_c = \sqrt{\frac{|\epsilon_x|}{\epsilon_z}}. \tag{2.10}$$

For values of k where the branches of the hyperbola lie close to the asymptotes, the direction of the energy flow is perpendicular to the asymptotes, i.e. the refraction angle is given by

$$\cot\theta_S = \sqrt{\frac{|\epsilon_x|}{\epsilon_z}}. \tag{2.11}$$

If we consider a large range of k values, it is easy to see that the refraction angle for most of them would be very close to the asymptotic limit given by Eq. (2.11). If the energy of the beam is distributed equally across many wave vector angles (or, more generally, across many Fourier spatial frequency harmonics), as might be the case for a point source, the angular distribution of energy flow is decidedly different: most energy will be transported in a cone of half-angle θ_S given by Eq. (2.11). Indeed, there are infinitely many wave vectors that are solutions of Eq. (2.5a), and they all contribute to propagation in the same direction. This is in sharp contrast to the behavior of isotropic dielectrics, where the power in a beam's spatial frequencies might get spread out over a narrower or broader spatial frequency range, but not shifted towards some preferred direction. Such beam-like directional radiation patterns have indeed been observed for sources embedded in strongly anisotropic plasmas [44, 45].

In this context, it is interesting to consider two special cases of the hyperbolic dispersion. First, suppose that the asymptotes of the hyperbola are parallel to the interface between two media, which we take to be the z axis.[2] This might be the case in the limit $|\epsilon_x| \gg \epsilon_z$ [Fig. 2.4(b)]. The energy refraction angle, then, is zero; all fields that enter the device propagate in the direction normal to the interface. This allows one to use multibeam interference effects to increase the coupling of energy into the device. Such regime is known as *channeling* [46], and has been suggested for use in sub-diffraction-limited imaging.

The second special case arises in anisotropic epsilon-near-zero (ENZ) materials, e.g. $\epsilon_x \approx 0$ (notice that this is the opposite of the channeling limit). From Fig. 2.4(c) we can see that this implies the energy for all but normal incidence starts flowing in the lateral direction. Later in this chapter, we will discuss this phenomenon in more detail and present experimental evidence that it can serve as a basis for narrow angular filters.

2.3 Possible implementations

2.3.1 Natural anisotropy

As we are starting to see, the special nature of the $\epsilon_x < 0,\ \epsilon_z > 0$ systems leads to a multitude of exotic effects. There arises a natural question: how can we elicit such a response from physical materials?

Perhaps surprisingly, the $\epsilon_x < 0,\ \epsilon_z > 0$ behavior is observed in a number of natural materials where structural anisotropy strongly affects the dielectric response. Examples of such materials can be found in the infrared and THz spectral bands. For

[2] When comparing structures in k-space and in "real" space (r-space), we utilize the canonical isomorphism induced between the two spaces by the plane waves of the form $\exp(i\boldsymbol{k}\cdot\boldsymbol{r})$ (or, more precisely, by the inner product $\boldsymbol{k}\cdot\boldsymbol{r}$). For instance, when we say that a line L_k in k-space is parallel to a line L_r in r-space, we mean that a wave with wave vector $\boldsymbol{k}$ orthogonal to L_k has phase fronts that are parallel to L_r.

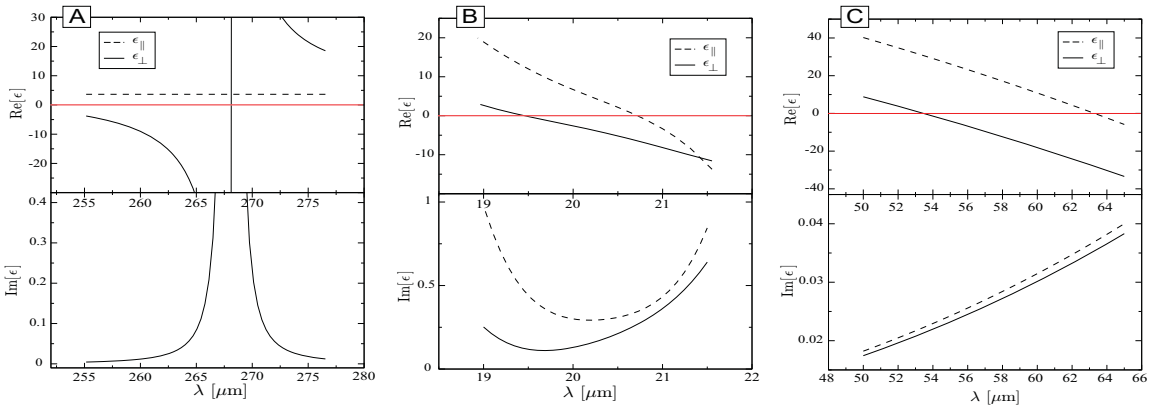

Figure 2.5: (A): The real (top panel) and the imaginary (bottom panel) parts of the dielectric function of TGS; the monoclininc C_2 axis is along the "perpendicular" ($\perp$) direction. (B): Same for sapphire; the crystallographic c axis is along the "perpendicular" ($\perp$) direction. (C): Same for monocrystalline bismuth.

instance, in the far infrared/low THz domain, this behavior is exhibited by triglycine sulfate (TGS), a compound widely used in fabricating infrared photodetectors. Spectroscopic studies of the crystal at low temperature have shown that phonon modes polarized parallel to the crystal's monoclinic C_2 axis significantly differ in frequency from phonons transverse to the axis. This results in a large anisotropy in the dielectric tensor along these directions. In particular, dielectric response for the field polarized *along* the C_2 axis features a resonance at 268 μm, which is absent if the incident field is polarized *transverse* to the C_2 axis [47]. Dielectric function $\epsilon_\perp$ in the vicinity of this resonance can be fitted with the Lorentz-Drude model [48], while $\epsilon_\perp$ in this region can be taken approximately constant [31, 47]. (Here, $\perp$ and $\parallel$ are orientation relative to the C_2 axis.) Lorentz-Drude model parameters from Ref. [48] were used to construct Fig. 2.5(a). As is evident from the figure, $\epsilon_\perp < 0$, while $\epsilon_\parallel > 0$ in the region $250 \leq \lambda \leq 268$ μm. Furthermore, the imaginary part of ϵ becomes small away from the resonance, minimizing absorption.

Whereas the phonon anisotropy of TGS exists in the low-THz domain, for other materials, it may occur in a different spectral band. In particular, the strong anisotropy of the dielectric response of sapphire (Al_2O_3) is also due to excitation

of different phonon modes (polarized either parallel or perpendicular to the c axis of the rhombohedral structure), but occurs around 20 μm. Fig. 2.5(b) shows experimentally-determined [49] $\epsilon_{\|}$ and $\epsilon_{\perp}$ as functions of frequency. As with TGS, a region of $\epsilon_{\perp} < 0$, $\epsilon_{\|} > 0$ is evident in the experimental data. Note that the minimum of the material absorption occurs in the frequency range of interest.

Anisotropic phonon excitations are not the only mechanism that can lead to strong dielectric anisotropy. Bismuth, a Group V semimetal with rhombohedral lattice and trigonal symmetry, exhibits such anisotropy due to a substantial difference in its electron effective masses along different directions in the crystal.

In the frequency region of interest, the spectral dependence of the electric permittivity of bismuth can be adequately described by the Drude model,

$$\epsilon = \epsilon_L \left(1 - \frac{\omega_{\rm pl}^2}{\omega^2 + i\omega\tau^{-1}} \right), \tag{2.12}$$

with ϵ_L the lattice permittivity, $\omega_{\rm pl} = Ne^2/\epsilon_L m_{\rm eff}$ the plasma frequency, and τ the relaxation time. These parameters are known from interferometric and reflectance studies of Bi samples. In particular, plasma frequency of pure bismuth at 4 K was measured to be 158 cm^{-1} for the incident E-field polarized perpendicular to the trigonal axis, and 186 cm^{-1} for the field polarized parallel to the axis [50]. These values are in agreement with other experiments [51, 52]. The lattice dielectric constant ϵ_L for the field perpendicular to the trigonal axis was found to be 110$\pm$10 cm^{-1} [52], in reasonable agreement with Ref. [51]. For polarization parallel to the trigonal axis, ϵ_L=76 [53].

There can be substantial variation in the relaxation time τ depending on the purity of the sample. We take τ=0.1 ns [52], however, this is a conservative estimate; for low temperatures, relaxation times over an order of magnitude greater have been reported as far back as 1975 [53]. Even with τ=0.1 ns, the typical ratio of imaginary and real parts of the dielectric function in Bi is on the order of 0.1% in the frequency interval

of interest, which enables many imaging and transmission applications [30]. It should also be noted that high-quality single-crystal films as thin as 1 μm, with the trigonal axis (C_3) oriented perpendicular to the film plane, have been reported [54], thereby essentially solving the technological issues in fabricating the proposed negative index device.

Fig. 2.5(c) shows the behavior of real and imaginary components of ϵ for Bi based on Eq. (2.12). The most prominent feature of these plots, the transition from $\epsilon > 0$ to $\epsilon < 0$, is determined by the highly anisotropic plasma frequency. This anisotropy creates a window between $\lambda = 53.7$ μm and 63.2 μm where $\epsilon < 0$ for the E-field along the C_3 axis, while $\epsilon > 0$ for E transverse to C_3. The existence of such 10 μm window was confirmed by direct measurement [55].

2.3.2 Artificial nanostructured systems

For spectral domains where natural effects do not result in differing signs of the dielectric tensor components, such anisotropy may be attained in metamaterials. To satisfy the requirement $\epsilon_x < 0$ and $\epsilon_z > 0$, the metamaterials must combine plasmonic or polar materials (with $\epsilon < 0$) with conventional dielectrics in an appropriate geometry.

The $\epsilon < 0$ components of such nanocomposites may come from a variety of sources. For instance, these negative permittivity response can be engineered artificially. One approach involves strongly doping a semiconductor, thereby creating a plasmon resonance. Another possible technique to induce negative permittivity is engineering quantum wells with appropriate intrasubband transitions. Negative permittivity is also quite common in naturally occurring materials. In the visible spectrum, plasmon resonances result in $\epsilon < 0$ for a number of metals. Silver is one example of a relatively low-loss plasmonic material. At longer wavelengths, phonon resonances can yield $\epsilon < 0$, with losses typically lower than those in silver. One such low-loss

material, well-suited for studying negative-index phenomena in the mid-IR, is silicon carbide [56, 57], with $\epsilon < 0$ between 10.3 and 11 μm. In what follows, we shall often refer to the $\epsilon < 0$ phases of nanocomposites as "plasmonic inclusions" or "metallic inclusions", keeping in mind that the actual material may be a metal, a doped semiconductor, or a phonon-polaritonic dielectric.

The key to achieving a very strong bulk anisotropy that can lead to a hyperbolic dispersion relation is to make sure the polarization response of the composite medium varies significantly depending on the direction of the applied field. This can be done by controlling the shape and/or the distribution of the metallic inclusions, thereby introducing anisotropic subwavelength structure.[3] Such structure can be created in a number of different ways. The most common configurations for the plasmonic inclusions are:

- a layered medium with alternative positive and negative permittivities in a particular direction
- aligned nanowires
- metallic particles anisotropically distributed in a dielectric host.

We now proceed to describe the first two systems in greater detail. We will provide the basic theoretical description and present the work done in collaboration with two leading experimental groups.

2.3.2.1 Layered medium: strongly doped semiconductor implementation

A layered medium with alternating signs of permittivities [30, 56, 59] is, perhaps, the simplest artificial arrangement that yields a hyperbolic dispersion relation. This

[3] We should note that the general concept of anisotropic subwavelength patterning in order to achieve birefringence has existed for a number of years under the name of *form birefringence* [58]. However, the use of this approach to create materials with a hyperbolic dispersion relation and unique optical properties is a new, previously unforeseen direction.

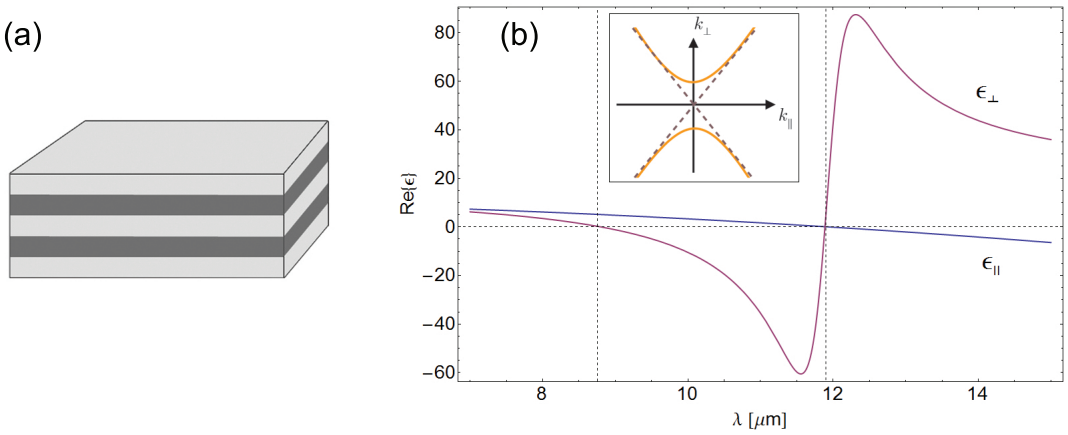

Figure 2.6: (a) Schematic representation of the planar metamaterial. (b) Dielectric function of the layered heterostructure in the effective medium approximation assuming doping levels $n = 7.5 \times 10^{-18}$ cm^{-1}. The $\{\epsilon_\perp > 0, \epsilon_\parallel < 0\}$ anisotropy is apparent between approximately 8.75 and 11.9 μm. Inset indicates the orientation of the dispersion relation hyperbola in that region. Note that for normal incidence this system is expected to have little transmittance.

medium consists of a sequence of "dielectric" layers ($\epsilon_1 > 0$) and "conductive" layers ($\epsilon_2 < 0$) [40]. The effective dielectric tensor of such a structure (with the volume fraction of the conducting layers N_c) is given by [60]

$$\begin{aligned} \epsilon_x &= \frac{\epsilon_1 \epsilon_2}{N_c\, \epsilon_1 + (1 - N_c)\epsilon_2} \\ \epsilon_z &= (1 - N_c)\epsilon_1 + N_c\, \epsilon_2. \end{aligned} \tag{2.13}$$

Provided that $\epsilon_1 > 0$ and $\epsilon_2 < 0$ in a certain frequency range, these equations lead to a well-defined frequency interval with $\epsilon_x < 0,\ \epsilon_z > 0$ (the exact values of the interval are determined from the dispersive characteristics of ϵ_1 and ϵ_2). Early research in multilayer planar metamaterials was motivated by the desire to lower losses in a plasmonic near-field superlens, in particular, Ag/SiO_2 multilayer systems and their imaging properties were actively investigated experimentally [61].

Planar layered systems can also be fabricated using epitaxial semiconductor growth, with selective doping used to attain $\epsilon_2 < 0$ in the "metallic" regions. A particular realization, composed of interleaved 80 nm layers of $In_{0.53}Ga_{0.47}As$ and

$Al_{0.48}In_{0.52}As$, was used by the Gmachl group to create the first experimental demonstration of negative refraction in non-magnetic hyperbolic metamaterials [62]. The layers, approximately 8.1 μm thick, were grown by molecular beam epitaxy on lattice-matched InP substrates; the InGaAs layers were heavily doped in order to attain $\epsilon < 0$ response below the plasma frequency. Several samples were studied, with free electron density ranging from 3.4×10^{-18} cm^{-1} to 7.5×10^{-18} cm^{-1}, and corresponding plasma frequencies ranged from 13.1 to 8.8 μm.

In addition to all-angle negative refraction, this system is predicted to have several interesting features.

Brewster's angle discontinuity

In anisotropic materials, Brewster's angle takes the form

$$\tan\theta_B = \sqrt{\epsilon'_z(\lambda)\frac{\epsilon'_x(\lambda)-1}{\epsilon'_z(\lambda)-1}}, \tag{2.14}$$

where $\epsilon'_{x,z}$ is the real part of the dielectric function and where incidence from vacuum was assumed. This equation features a zero in the denominator when $\epsilon'_z(\lambda) = 1$. One expects to be able to observe this divergent behavior experimentally.

In Fig. 2.7(c) we plot the spectral dependence of Brewster's angle superimposed with the computed ratio of TM and TE intensity reflection coefficients using the dielectric functions of the experimental system. It is apparent that the functional dependence of the dielectric functions not only guarantees the diverging behavior, but also ensures that the typical values of the Brewster's angle for wavelengths that are lower or higher than that critical point are quite different. This discontinuity in the Brewster's angle was clearly seen in the experimental data [see Fig. 2.7(a)], where the ratio of TM and TE intensities was measured as a function of incidence angle and wavelength. The experimental data showed very good qualitative and quantitative

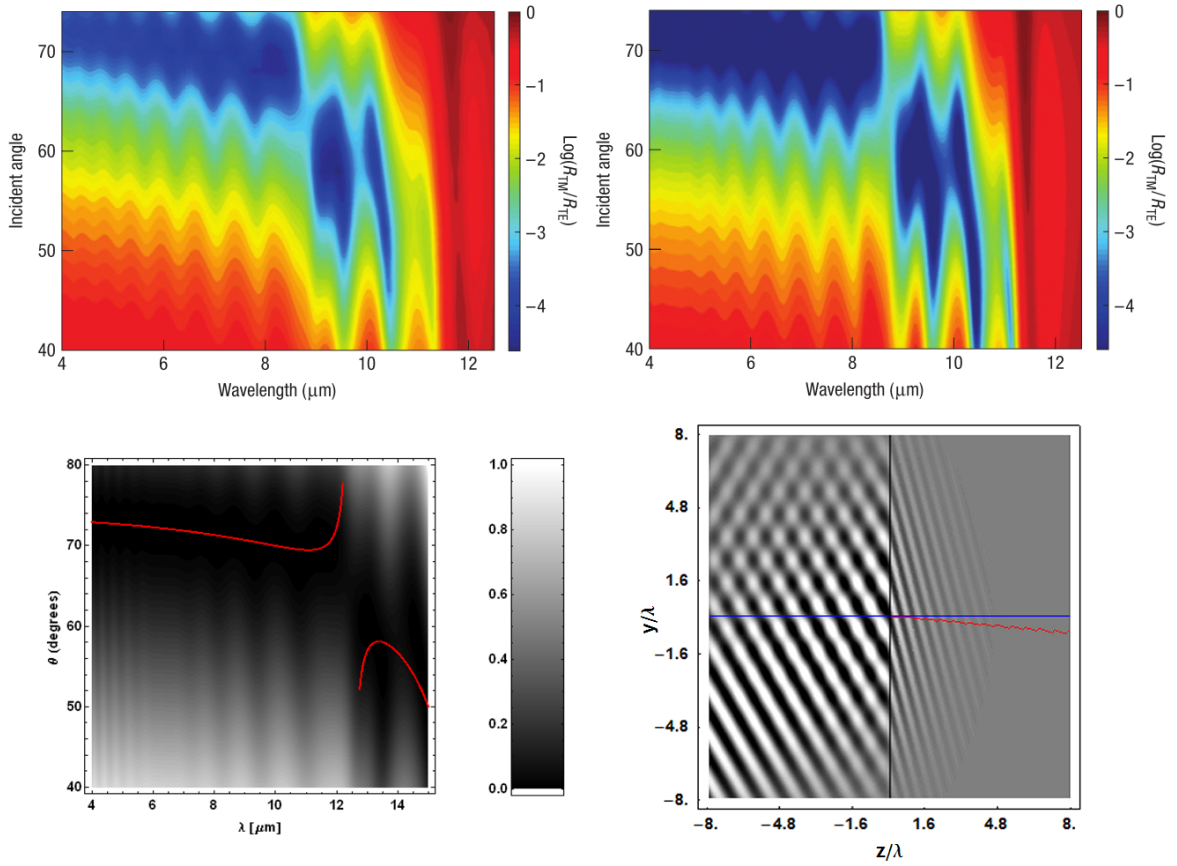

Figure 2.7: (a) Experimental reflectance data (b) Theoretical prediction (c) Brewster's angle discontinuity: Brewster's angle given by Eq. (2.14) superimposed on the theoretically predicted TM/TE reflection ratio curves. (d) Full numerical calculations demonstrating negative refraction of a monochromatic transverse-magnetic-polarized gaussian beam across an air-metamaterial interface (adapted from Ref. [62])

agreement with the theoretical prediction [Fig. 2.7(b)], which used only the reported material doping density and sample thickness and was based on the transfer matrix method (see Appendix C).

Zero-reflection bands

The experimental data exhibited several bands of near-zero reflection bands in the TE polarization as the wavelength of the illuminating light was changed. Although we have been treating this metamaterial in the effective medium approximation, because it is a precisely manufactured multilayer stack, it is amenable to standard transfer matrix analysis.

Let us assume that the medium contains N layer pairs of equal thickness $2d$ (for each pair) and refractive indexes n_2, n_1. If the medium to the left and the right of the structure has the index n_1, the amplitudes of incident and reflected waves are a_0 and b_0 and the amplitude of the transmitted wave is a_N, we can write:

$$\begin{pmatrix} a_0 \\ b_0 \end{pmatrix} = T^N \begin{pmatrix} a_N \\ b_N \end{pmatrix}, \tag{2.15}$$

where T is the transfer matrix for the 2-layer unit cell of our superlattice obtained via boundary conditions at the interfaces of the unit cell. Note that for any diagonalizable matrix, T^N can be computed analytically.

The elements of T are given by

$$\begin{aligned}
t_{11} &= e^{-ik_1 d}\left(\cos(k_2 d) - \frac{i}{2}\left(\frac{k_2}{k_1} + \frac{k_1}{k_2}\right)\sin(k_2 d)\right) \\
t_{12} &= -e^{ik_1 d}\frac{i}{2}\left(\frac{k_2}{k_1} - \frac{k_1}{k_2}\right)\sin(k_2 d) \\
t_{21} &= \frac{i}{2}\, e^{-ik_1 d}\left(\frac{k_2}{k_1} - \frac{k_1}{k_2}\right)\sin(k_2 d) \\
t_{22} &= e^{ik_1 d}\left(\cos(k_2 d) + \frac{i}{2}\left(\frac{k_2}{k_1} + \frac{k_1}{k_2}\right)\sin(k_2 d)\right),
\end{aligned} \tag{2.16}$$

where k_1 and k_2 are defined by

$$\begin{aligned} \epsilon_1 \left(\frac{\omega}{c}\right)^2 &= k_1^2 + k_\parallel^2 \\ \epsilon_2 \left(\frac{\omega}{c}\right)^2 &= k_2^2 + k_\parallel^2. \end{aligned} \tag{2.17}$$

The reflection coefficient for TE fields is given by

$$\begin{aligned} r_N &= \left(\frac{b_0}{a_0}\right)_{b_N=0} = \frac{\left(T_{21}^N\right)}{\left(T_{11}^N\right)} \\ &= \frac{e^{-ik_1 d} \frac{1}{2} \left(\frac{k_1}{k_2} - \frac{k_2}{k_1}\right) \sin(k_2 d)}{\sin(k_1 d)\cos(k_2 d) + \frac{1}{2}\left(\frac{k_1}{k_2} + \frac{k_2}{k_1}\right)\sin(k_2 d)\cos(k_1 d) + i\frac{\sin(\phi)}{\tan(N\phi)}}, \end{aligned} \tag{2.18}$$

where $\phi = \frac{\omega}{c} 2d$.

For the case k_1,$k_2 \ll \frac{1}{d}$, we also have $\phi \ll 1$, and we can use the following approximation for r_N:

$$r_N = \frac{1 - \left(\frac{k_2}{k_1}\right)^2}{3 + \left(\frac{k_2}{k_1}\right)^2 + 2\, i \frac{\phi/k_1 d}{\tan(N\phi)}}. \tag{2.19}$$

Let us assume now that the medium to the left of the layered structure is air, with $\epsilon_0 \equiv 1$ and the dispersion relation

$$\left(\frac{\omega}{c}\right)^2 = k_0^2 + k_\parallel^2.$$

The reflection coefficient of the structure is now

$$r = \frac{r_0 + r_N}{1 + r_0 r_N}, \tag{2.20}$$

where

$$r_0 = \frac{k_0 - k_1}{k_0 + k_1}. \tag{2.21}$$

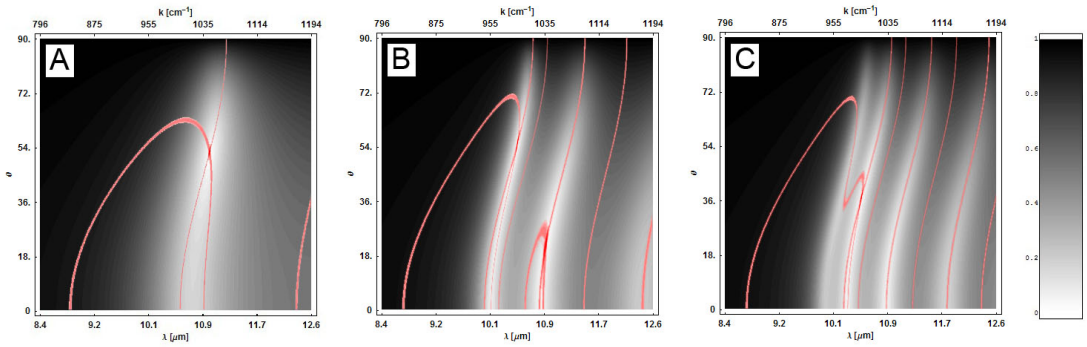

Figure 2.8: Solutions of $\mathrm{Re}(r_0+r_N) \simeq 0$ (red hairpin curves) and $\mathrm{Im}(r_0+r_N) \simeq 0$ (red vertical stripes) superimposed on the grayscale plot of $r(\theta, \lambda)$ (white regions indicate 0 reflection) for 2 μm (a), 5 μm (b) and 8 μm (c) total device thickness.

We seek regions of zero reflection, i.e. regions where (2.20) vanishes. In these regions, $r_0 + r_N = 0$ is satisfied, with r_0 and r_N given by (2.21) and (2.18). With these substitutions, $r_0 + r_N = 0$ is equivalent to

$$2k_0k_1 - k_1^2 - k_2^2 + i\frac{\phi/d}{\tan(N\phi)}(k_0 - k_1) = 0,$$

with $\phi \simeq d\sqrt{2(k_1^2 + k_2^2)}$ for k_1,$k_2 \ll \frac{1}{d}$.

We model our system as a series of metallic–dielectric layers, with no losses in the dielectric layers ($\epsilon_1 = 12.1$) and with a complex dielectric function in the metallic layers given by Drude model ($\omega_{\mathrm{pl}} = 1300$ cm^{-1}, $\tau = 0.2$ ps) as

$$\epsilon_2 \simeq \epsilon_1 \left(1 - \frac{\omega_{\mathrm{pl}}^2}{\omega^2}\right) + i\,\epsilon_1 \frac{1}{\omega\tau}\frac{\omega_{\mathrm{pl}}^2}{\omega^2}.$$

Thus, $r_0 + r_N$ is a complex function, and to identify the regions where $r_0 + r_N \simeq 0$ we plot $\mathrm{Re}(r_0 + r_N) \simeq 0$ and $\mathrm{Im}(r_0 + r_N) \simeq 0$ as a function of incidence angle θ and wavelength λ, looking for areas where the curves intersect. Figure 2.8 shows these curves superimposed with the reflection coefficient calculated via (2.20) for superlattice thickness of 2, 5, and 8 μm. It is evident that regions of near perfect

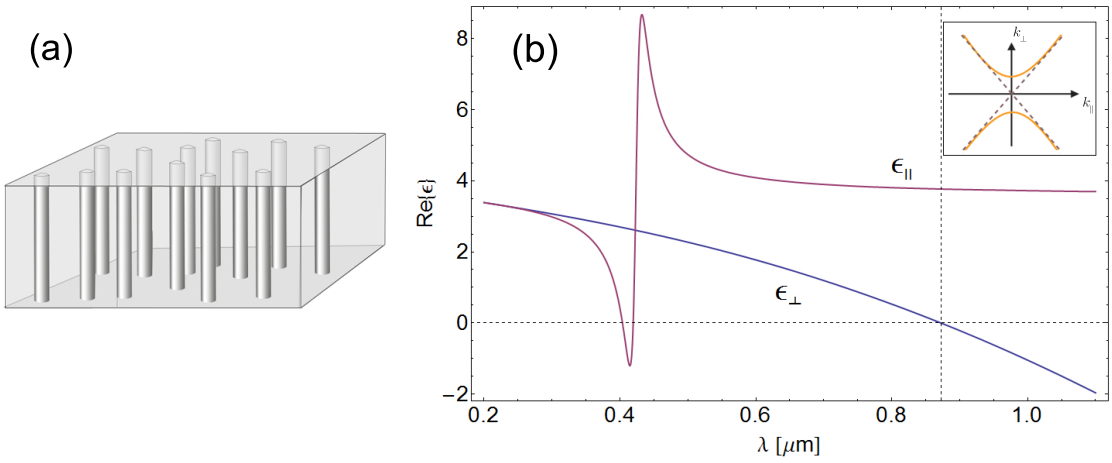

Figure 2.9: (a) Schematic representation of the array of nanowires in a dielectric host. (b) Dielectric function of the nanowire medium (silver embedded in alumina) computed using the Maxwell-Garnett approximation for $N_{\rm pl}$=8.25%. For wavelengths greater than 873 nm, the medium exhibits the $\{\epsilon_\perp < 0, \epsilon_\parallel > 0\}$-type anisotropy. Inset indicates the orientation of the dispersion relation hyperbola in that region. Close to the $\epsilon_\perp = 0$ point, the asymptotes of the hyperbola collapse to a single vertical line.

transmission exist where the solutions to the real and imaginary parts of $r_0 + r_N \simeq 0$ intersect or are in close proximity.

2.3.2.2 Aligned nanowires: Ag-filled alumina implementation

We now turn to another possible implementation of a hyperbolic metamaterial: an array of aligned metallic ($\epsilon < 0$) nanowires embedded in a dielectric host [see Fig. 2.9(a)]. Such materials are usually fabricated as optically thick dielectric plates with the nanowires grown vertically.

In the general case, the full analytical treatment of fields in such a material is complicated. However, the case of small plasmonic inclusion concentration for approximately normal incidence is adequately described by the Maxwell-Garnett approximation as

$$\begin{aligned} \epsilon_\parallel &= \frac{\epsilon_d\left(\epsilon_d + \epsilon_{\rm pl}\right)\left(1 - N_{\rm pl}\right) + 2\epsilon_d N_{\rm pl}\epsilon_{\rm pl}}{2\epsilon_d N_{\rm pl} + \left(\epsilon_d + \epsilon_{\rm pl}\right)\left(1 - N_{\rm pl}\right)} \\ \epsilon_\perp &= \epsilon_d\left(1 - N_{\rm pl}\right) + N_{\rm pl}\epsilon_{\rm pl}, \end{aligned} \tag{2.22}$$

where N_{pl} and ϵ_{pl} are the volume fraction and the permittivity of plasmonic inclusions and ϵ_d is the dielectric constant of the host medium.

We plot the resultant dielectric function in Fig. 2.9(b) for the particular case of silver nanowires embedded in alumina substrate. Wavelength dependence of the dielectric functions was modeled after Refs. [63] and [64]. From this plot we can see that for wavelengths greater than 873 nm, the medium exhibits the $\{\epsilon_\perp < 0, \epsilon_\parallel > 0\}$-type hyperbolic anisotropy. Note that this is the same type of anisotropy that we considered before in the planar metamaterial. This might seem puzzling, as the orientation of the plasmonic components in these two types of metamaterials is different. However, close examination of Fig. 2.6(b) and Fig. 2.9(b) reveals that the general behavior of $\epsilon_\parallel$ and $\epsilon_\perp$ are indeed switched for the planar and the nanowire structure. Due to the resonant-like behavior of one of the dielectric tensor components, both materials support regions with both types of hyperbolic dispersions (i.e. $\epsilon_\perp = 0$ and $\epsilon_\parallel = 0$); the operating frequencies in the two experiments are chosen such that only the $\epsilon_\perp < 0$-type dispersion is in effect.

Close to the $\epsilon_\perp = 0$ point, the asymptotes of the hyperbola collapse to a single vertical line. As a result, only normally-incident light is able to penetrate into the material, which effectively acts as a very narrow angular filter. We can estimate the acceptance angle of the material by plotting the angle between hyperbola's asymptotes as a function of $\text{Re}[\epsilon_\perp]$ [Fig. 2.10(b)] using Eq. (2.10). For $\text{Re}[\epsilon_\perp] = -0.0057$, this result gives 4.2 degrees.

To get a more precise estimate for angular transmission, we can find the exact solution for the transfer function of an anisotropic slab. It can be derived by summing a geometric series arising from multiple reflections, or by explicitly solving Maxwell's equations subject to the standard boundary conditions. Assuming the material is anisotropic and surrounding medium is vacuum, the intensity transfer function for the P and S polarizations is

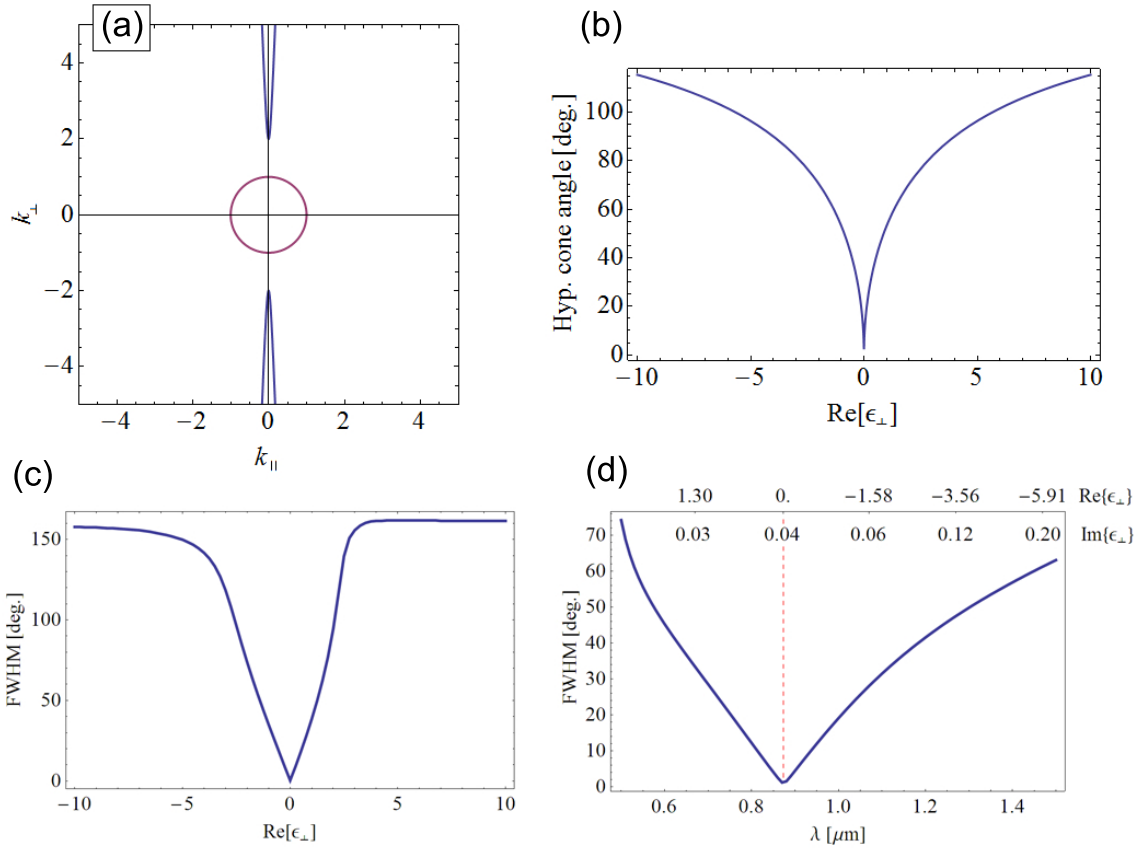

Figure 2.10: (a) Hyperbolic dispersion isofrequency plot for the case $\mathrm{Re}[\epsilon_\perp] \approx 0$ ($\epsilon_\perp = -0.0057 + 0.03i$); wave vector isofrequency plot in vacuum (circle with radius 1) is plotted in comparison. The angular width of the hyperbola branch is 4.2 degrees. (b) Angular width of the hyperbola as a function of $\mathrm{Re}[\epsilon_\perp]$; it can serve as an estimate for FWHM of the transmitted signal. (c) FWHM of the angular transmittance band as a function of $\mathrm{Re}[\epsilon_\perp]$, calculated at $\mathrm{Re}[\epsilon_\parallel] = 3$, $\mathrm{Im}[\epsilon_\parallel] = \mathrm{Im}[\epsilon_\perp] = 0.01$, $d = 40$ μm, and $\lambda = 600$ nm. (d) FWHM of the transmittance peak for p polarization, calculated as a function of wavelength. Note that FWHM is minimal when $\mathrm{Re}[\epsilon_\parallel] \approx 0$. (Adapted in part from Ref. [65])

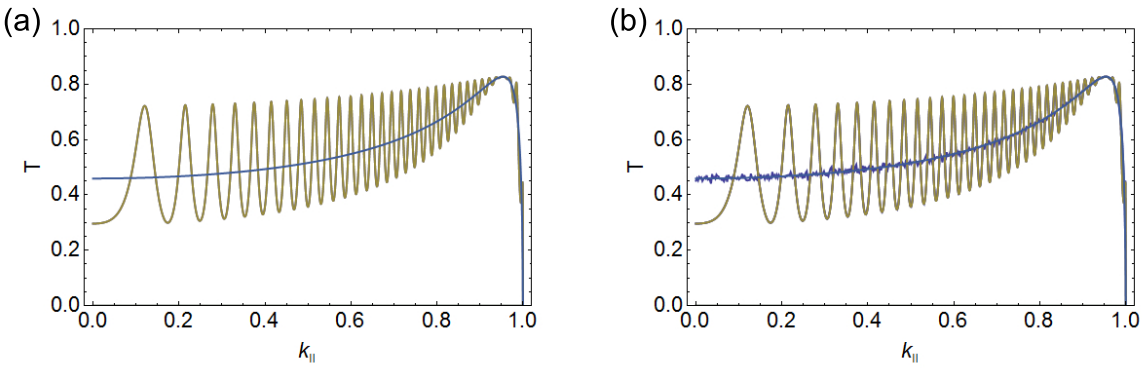

Figure 2.11: Averaging of the multiple beam interference reflection oscillations: (a) analytical result; (b) numerical averaging over many realizations obtained by randomly perturbing device thickness

$$T^{(P|S)}(k_x) = \left| \frac{1}{\cos\left(dk_{z_2}\right) - \frac{1}{2} i \sin\left(dk_{z_2}\right) \left(\frac{K_2^{(P|S)}}{k_{z_1}} + \frac{k_{z_1}}{K_2^{(P|S)}} \right)} \right|^2 . \tag{2.23}$$

Here,

$$\begin{aligned} k_{z_1} &= \sqrt{1 - k_x^2} \\ K_2^{(P)} &= k_{z_2}^{(P)} / \epsilon_{\parallel}, \qquad & K_2^{(S)} &= k_{z_2}^{(S)} \\ k_{z_2}^{(P)} &= \sqrt{\epsilon_{\parallel} \left(1 - \frac{k_x^2}{\epsilon_{\perp}} \right)}, \qquad & k_{z_2}^{(S)} &= \sqrt{\epsilon_{\parallel} - k_x^2}. \end{aligned} \tag{2.24}$$

When plotted in the regime of weak losses, these equations show rapid oscillations due to interference arising from multiple reflections. In practice, phases of the reflected light are often randomized by variations in the slab thickness and surface imperfections. Intensity transfer function is then obtained by taking an average over the phases; it can be expressed as

$$T_I^{(P|S)}(k_x) = \frac{|t_{12} t_{21}|^2}{\sqrt{|r|^8 e^{-4d \operatorname{Im}\left[k_{z_2}^{(P|S)}\right]} - 2|r|^4 + e^{4d \operatorname{Im}\left[k_{z_2}^{(P|S)}\right]}}}, \tag{2.25}$$

where

$$
\begin{aligned}
t_{12} &= \frac{2}{1 + K_2^{(P|S)}/k_{z_1}} \\
t_{21} &= \frac{2}{1 + k_{z_1}/K_2^{(P|S)}} \\
r &= \frac{1 - K_2^{(P|S)}/k_{z_1}}{1 + K_2^{(P|S)}/k_{z_1}}.
\end{aligned}
\tag{2.26}
$$

It is interesting to compare the curves given by Eqs. (2.23) and (2.25). In Fig. 2.11(a) we superimpose those two curves, while in Fig. 2.11(b) we show the transmission function of Eq. (2.23) together with its averaged value as d is randomly varied over the range of a few λ. Predictably, we see that oscillations due to multibeam interference effects average out completely.

When $\epsilon_\perp \approx 0$, we have $\operatorname{Im} k_{z_2}^{(P)} \approx \sqrt{\epsilon_\parallel/\epsilon_\perp}k_x \gg 1$. In this regime, for $k_x > 0$ (non-normal incidence) the leading term of Eq. (2.25) becomes $\exp(-2d\sqrt{\epsilon_\parallel/\epsilon_\perp}k_x) \ll 1$, which indicates that transmission of P polarization is exponentially suppressed.

In realistic materials, the $\epsilon_\perp \approx 0$ condition is difficult to achieve due to the presence of finite losses. However, the weaker set of constraints $\operatorname{Re}\epsilon_\perp \approx 0$, $\operatorname{Im}\epsilon_\perp \lesssim 1$ still results in exponential suppression of P polarization. The onset of this exponential cut-off, as well as the width of the transmission pass-band (centered around $k_x = 0$) can be quantified by assuming

$$
\operatorname{Re}\epsilon_\perp \ll \operatorname{Im}\epsilon_\perp; \quad \operatorname{Im}\epsilon_\parallel \ll \operatorname{Re}\epsilon_\parallel,
\tag{2.27}
$$

which allows to expand the denominator of Eq. (2.25) while taking the numerator to be constant. The result is

$$
T_I^{(P)}(k_x) \simeq 4\frac{\sqrt{\operatorname{Re}\left(\epsilon_\parallel\right)}}{\left(\sqrt{\operatorname{Re}\left(\epsilon_\parallel\right)}+1\right)^2} \cdot \exp\left(-d\frac{\operatorname{Im}\left(\epsilon_\parallel\right)}{\sqrt{\operatorname{Re}\left(\epsilon_\parallel\right)}}\right) \exp\left(-k_x^2/2\sigma^2\right),
\tag{2.28}
$$

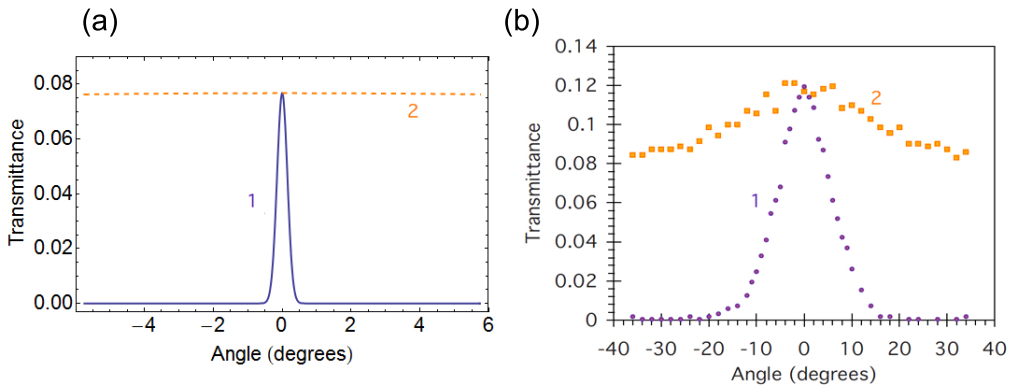

Figure 2.12: (a) Transmittance functions for p polarization (1) and s polarization (2) in the regime $\mathrm{Re}[\epsilon_{\|}] \approx 0$. (b) Experimentally measured angular transmittance profiles in for p and s polarization shows qualitative agreement with theoretical predictions. (Adapted from Ref. [65])

where

$$\sigma^2 = \frac{\left[\mathrm{Im}\left(\epsilon_{\perp}\right)\right]^2 \sqrt{\mathrm{Re}\left(\epsilon_{\|}\right)}}{2d\left(\mathrm{Im}\left(\epsilon_{\perp}\right)\mathrm{Re}\left(\epsilon_{\|}\right) - \mathrm{Re}\left(\epsilon_{\perp}\right)\mathrm{Im}\left(\epsilon_{\|}\right)\right)}. \tag{2.29}$$

The angular spectrum intensity passband for P polarization can be described by a Gaussian curve; lowering the imaginary permittivity contributions while maintaining the conditions $\{\mathrm{Re}\,\epsilon_{\perp} \ll \mathrm{Im}\,\epsilon_{\perp};\ \mathrm{Im}\,\epsilon_{\|} \ll \mathrm{Re}\,\epsilon_{\|}\}$, results in a narrow angular transmittance band centered on $k_x = 0$.

As follows from Eq. (2.25), the full width at half maximum (FWHM) of the transmittance band has a minimum at $\mathrm{Re}\,\epsilon_{\perp} = 0$ [see Fig. 2.12(c,d)]. The transmittance in S polarization, $T_I^S(k_x)$, is found to be nearly independent of the incidence angle [Fig. 2.12(a)]. Such transmission characteristics make the uniaxial ENZ metamaterials particularly suitable for application in narrow-band angular filters and polarizers.

Experimental data from transmission measurements of an array of silver nanowires embedded in an alumina membrane is plotted in Fig. 2.12(b). In a qualitative agreement with the theoretical predictions, it is seen that the transmittance peak in P polarization is rather narrow, while the transmittance band in S polarization is significantly broader. This suggests that after proper optimization, the demonstrated ENZ metamaterial can be used as an angular filter and polarizer. The relatively large

width of the experimental transmittance peak can probably be explained by imperfections of the sample causing scattering and partial depolarization of light inside the membrane's volume [65].

2.4 Conclusion

In this chapter, we introduced the concept of hyperbolic dispersion relation, and discussed the possible material systems (natural and artificial) that support the strong anisotropy required for hyperbolicity. We also presented the theoretical and experimental results related to reflection and transmission of light through these materials. While conceptually simple, those experiments have demonstrated the fundamentally new behavior of hyperbolic metamaterial systems, such as negative refraction, Brewster's angle discontinuity, and narrow angular filtering in the ENZ regime.

However, there is much more to the story of hyperbolic materials than negative refraction and modified transmission properties. Indeed, this is true for metamaterials in general: "negative refraction" was a headlining phenomenon in the early days of metamaterials, but the real interest from the research community focused on the Veselago medium's ability to support unusual waves and/or resonances (which, in particular, enabled Pendry's famous superlens [2]).

In the following sections we will continue describing the novel properties of the hyperbolic materials, focusing on the fundamental ways in which light propagation changes owing to the hyperbolic dispersion relation. This can lead to many prospective applications in a diverse range of nanophotonic devices.

Chapter 3

Hypersingularity

3.1 Introduction

The previous chapter dealt with the role of HMMs in enabling negative refraction and closely related phenomena. Those were important first steps in understanding the optics of this novel medium. However, this is just the beginning of the story. In order to appreciate the potential impact of hyperbolic dispersion in materials, it is enough to recognize that it implies the lack of high spatial frequency cut-offs associated with all conventional optical propagation. It is exactly those cut-offs that limit the resolution of imaging instruments. It is also the reason that integrated optical components are so ponderous and bulky compared to the svelte 20 nm transistor gates or 80 nm interconnects of modern microelectronics. The ability to support high-k propagating waves, guiding and confining light on scales much smaller than the vacuum wavelength, imbues HMMs with great potential in novel nanophotonic devices.

The behavior of light in any optical device is determined both by the properties of materials in which light propagates and by device geometry, which sets up the boundary conditions. Often, it is the interplay of those two factors that determines the

device operation, and it is only in the context of appropriate boundary conditions that some of the unusual features of material response can become apparent. The original superlens [2] is an example of this: only after considering the Veselago medium in the impedance-matched planar slab configuration did it become apparent that unlike conventional materials, it can support degenerate, dispersionless surface polaritons that can potentially be used for subwavelength imaging [66].

The development of hyperbolic metamaterials followed a somewhat similar path. The original reports of negative refraction [28, 31, 30] were followed by proposals to use HMMs for subwavelength-resolved imaging [67, 68, 33, 69, 4]. The key, in each proposal, was the unbounded nature of the hyperbolic dispersion relation. However, all but two of those papers described planar systems. It turned out that treatment of HMMs using curvilinear boundary conditions [69, 4], and the resultant analysis of angular momentum states in the proposed *hyperlens* [4] served as a take-off point for understanding the singularity in the photonic density of states exhibited by hyperbolic materials, a phenomenon that has broad implications beyond super-imaging. Let us, then, proceed with the description of the hyperlens.

3.2 The hyperlens

3.2.1 Hyperbolic dispersion in cylindrical coordinates

To appreciate what is different about the hyperbolic dispersion when we allow the systems to be non-planar, consider the solution to Maxwell's equations in cylindrical coordinates:

$$\boldsymbol{\nabla} \times \left[\boldsymbol{\epsilon}^{-1}(\boldsymbol{\nabla} \times \boldsymbol{H})\right] = \frac{\omega^2}{c^2}\boldsymbol{H}. \tag{3.1}$$

As before, we focus primarily on the TM modes, which, in this geometry, means that the only component of the field $\boldsymbol{H}$ is in the $\hat{\boldsymbol{z}}$ direction. In cylindrical coordinates,

Eq. (3.1) becomes

$$\frac{1}{r}\frac{\partial}{\partial r}\frac{r}{\epsilon_\theta}\frac{\partial H_z}{\partial r}+\frac{1}{r^2}\frac{\partial}{\partial\theta}\frac{1}{\epsilon_r}\frac{\partial H_z}{\partial\theta}+\frac{\omega^2}{c^2}H_z=0. \tag{3.2}$$

The solution to this equation is standard: Ansatz $H_z(r,\theta)=H_z(r)\exp(im\theta)$ converts Eq. (3.2) into the Bessel equation, and requiring finite fields everywhere, the solution is

$$H_z(r,\theta)=J_{m\sqrt{\frac{\epsilon_\theta}{\epsilon_r}}}\left(\sqrt{\epsilon_\theta}\frac{\omega}{c}r\right)\exp(im\theta). \tag{3.3}$$

We can obtain some intuition about the behavior of these solutions in an anisotropic environment by generalizing the dispersion relation of Eq. (2.4) for the case of cylindrical geometry. In particular, we have

$$\frac{k_r^2}{\epsilon_\theta}+\frac{k_\theta^2}{\epsilon_r}=\frac{\omega^2}{c^2}. \tag{3.4}$$

Note that this assumes cylindrical anisotropy, i.e. the wave traveling in the radial direction at an arbitrary angle will induce the same polarization response. We are not simply taking a uniaxial crystal and imposing cylindrical boundary conditions.

Although we are not working in the plane wave basis, the quantities k_r and k_θ have a very similar meaning to the familiar components of the wave vector. Namely, k_r gives the spatial oscillation frequency in the radial direction, and k_θ in the angular direction. Furthermore, we can give an explicit expression for k_θ via

$$e^{im\theta}=e^{ir\theta k_\theta}. \tag{3.5}$$

Together with the usual association $p=\hbar k$, this implies that $m=rk_\theta$ can be interpreted as angular momentum. Periodic boundary conditions ensure that m is an integer. Thus, for every discrete m Eq. (3.3) represents a different angular momentum state.

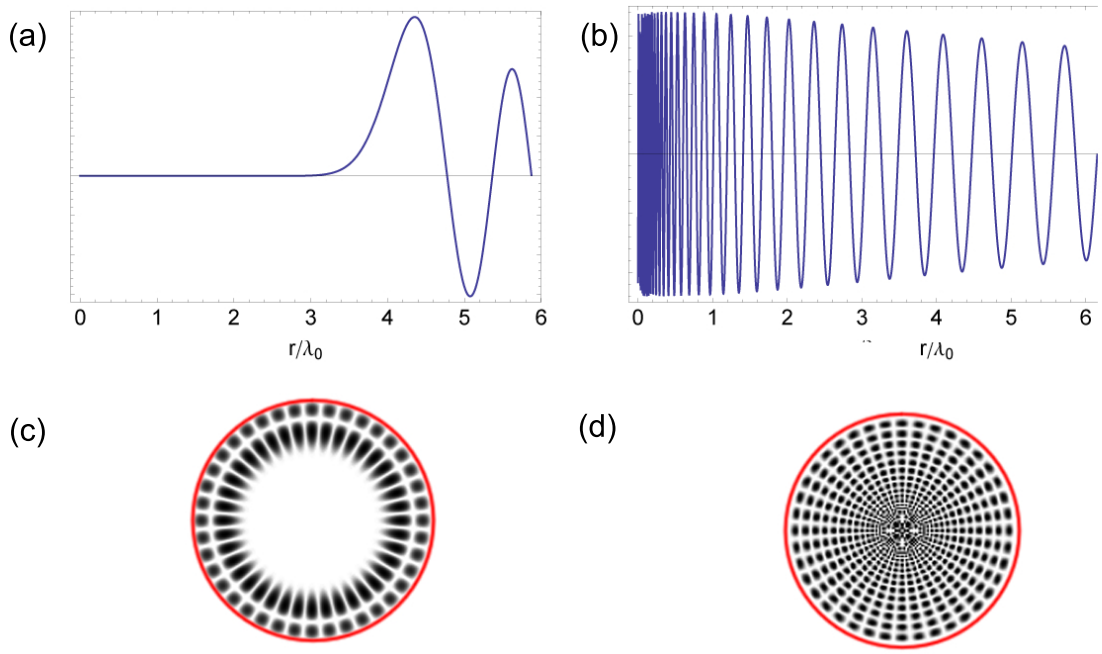

Figure 3.1: Bessel functions [radial part of Eq. (3.3)] and field magnitude of whispering gallery modes in isotropic ($\epsilon = 2$) (a,c) and hyperbolic ($\{\epsilon_r = -2, \epsilon_\theta = 2\}$ (b,d) cylindrical structures for a high angular momentum mode (m=36). (Adapted in part from Ref. [4].)

Eq. (3.4) gives an intuition for the behavior of the Bessel solutions (3.3) for small values of r. Notice that for $m \neq 0$, as r decreases, the tangential wave vector component k_θ grows, while k_r decreases. For some critical value $r = R_c$, this radial component of the wave vector vanishes and then becomes imaginary. This classical turning point – the boundary at which the incoming wave turns back – corresponds to the caustic. Inside the caustic, the angular momentum states become evanescent. Using the condition $k_r = 0$, it is easy to find the radius of the caustic from Eq. (3.4): $R_c = m\lambda/(2\pi\sqrt{\epsilon_r})$. It is interesting to note that the caustic radius increases with angular momentum and the circumference of the caustic corresponds exactly to m wavelengths (since for the wave propagation strictly in the tangential direction, the local wavelength is λ/ϵ_r).

What we just described can be viewed as a statement of the diffraction limit in cylindrical geometry. Indeed, the conventional way to think about diffraction is in

terms of spatial Fourier harmonics of the electric field. The field is expressed as a superposition of plane waves, each proportional to $\exp(i\boldsymbol{k}\cdot\boldsymbol{r})$. Eq. (2.4) shows that in conventional materials, large values of k_x cause this propagation factor to exponentially decay, much in the same way that large values of k_θ in the cylindrical geometry cause the angular momentum states to become evanescent beyond the caustic.

All of the above considerations, while taking into account anisotropy, implicitly assumed $\epsilon_{r,\theta} > 0$. Let us relax this assumption and reexamine the results. By analogy with planar systems, we might expect that a different form of the dispersion relation might enable waves that would have been otherwise cut off to propagate. Indeed, this is exactly what happens.

The existence of caustic, and hence the exponential decay of the field for $r < R_c$, is a consequence of the upper bound on k_θ dictated by the exact functional form of dispersion relation (3.4). What happens when this expression describes a hyperbola?.. We will consider, in particular, the case $\{\epsilon_\theta > 0, \epsilon_r < 0\}$. The dispersion relation of Eq. (3.4), then, allows for very high values of k, limited only by the material scale of the medium. As the tangential component of the wave vector increases towards the center as shown in Fig. 2.1 the radial component also increases; Eq. 3.4 can be satisfied for any radius and any value of m. Thus, as long as the effective medium description is valid, there is no caustic, and, as can be seen in Fig. 3.1, the high angular momentum states have appreciable magnitude of the field at the center ($r \approx 0$). It is evident that the distance between the field nodes (i.e. the effective wavelength) at the center is much less than its vacuum value. The field thus penetrates to the center and acts as the subwavelength probe for an object placed at the origin. Since in the medium with $\{\epsilon_\theta > 0, \epsilon_r < 0\}$ anisotropy these high angular momentum modes are propagating waves, they can carry the information about subwavelength structure of the object to the far field.

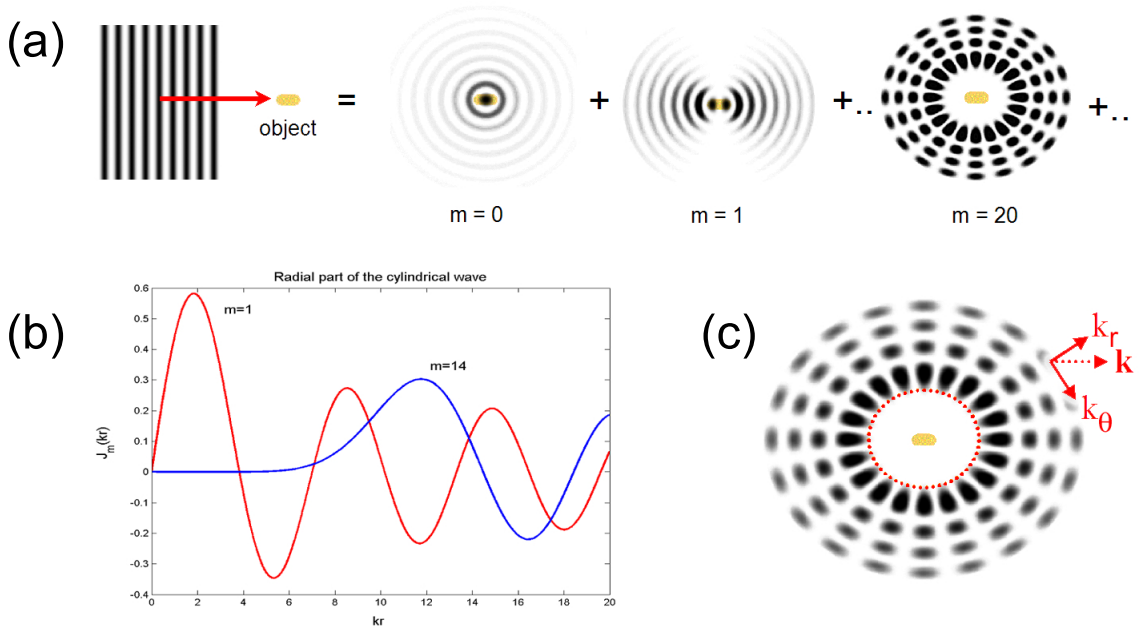

Figure 3.2: Scattering of an incident plane wave (a) can be represented as scattering of various angular momentum modes. Higher order modes are exponentially small at the center (b). This results from an upper bound on values of k_θ and the formation of the caustic shown in red in (c). (From Ref. [4])

Because of the potential imaging applications enabled by hyperbolic anisotropy in cylindrical coordinates, and because the usual description of this problem involves a curved dielectric-metamaterial interface, the device that uses the high angular momentum modes to probe the structure of an object placed at the center was called the hyperlens [4].

3.2.2 Angular momentum states as information channels

Up until now, the discussion of subwavelength imaging in cylindrical hyperbolic materials has been somewhat heuristic. We can put it on a firmer theoretical ground by considering the angular momentum states from the point of view of scattering theory.

In traditional discussions of imaging, waves scattered by the object are examined in a monochromatic plane wave basis with a wide spectrum of spatial frequencies. The choice of basis, however, is dictated by the symmetry of the object under con-

sideration and/or by convenience. Furthermore, we can often conveniently switch between different bases.

In scattering problems, the principal object under consideration is the scattering potential. It is easiest to study its properties by using cylindrical or spherical coordinates with the scatterer at the center. One of the reasons it works so well is the fact that any plane wave illuminating an object can be expanded in a basis of cylindrical waves as

$$\exp(ikx) = \sum_{m=-\infty}^{\infty} i^m J_m(kr) \exp(im\phi), \tag{3.6}$$

where $J_m(kr)$ denotes the Bessel function of the first kind and m is the angular momentum mode number of the cylindrical wave [this decomposition is illustrated schematically in Fig. 3.2(a)]. (Eq. (3.6) is known as the Jacobi-Anger identity; a similar expansion exists in terms of spherical Bessel functions.) In this representation, reconstructing an image is equivalent to retrieving the scattering amplitudes and phase shifts of the various constituent angular momentum modes. The resolution limit in the cylindrical wave basis can be restated as the limit to the number of retrieved angular momentum modes with appreciable amplitude or phase change after scattering from the object.

We may think of the scattered angular momentum modes as distinct information channels through which the information about the object at the origin is conveyed to the far field. However, even though the number of these channels is infinite [m is unbounded in expansion (3.6)], very little information is carried over the high-m channels. As evidenced by Fig. 3.2(b), which shows the exact radial profile of the electric field for m=1 and m=14, for high values of m the field exponentially decays at the origin. This suggests that the interaction between a high-m mode and an object placed at the origin is exponentially small, i.e. the scattering of such modes from the object is negligible. Classically, this corresponds to the parts of an illuminating beam that have a high impact parameter and therefore miss the scatterer.

In the hyperlens, this picture changes dramatically, owing to the fact that high angular momentum modes are able to propagate throughout the device. As a result, the number of information channels is significantly larger – it is, in principle, infinite for an ideal medium. Recall that at a distance r from the center of the device, the tangential wave vector is given by $k_\theta = m/r$. The spatial length scales probed are of the order r/m. The higher-m information channels are able to convey information about arbitrarily fine spatial structures, with the resolution limited only by cut-offs associated with material patterning scale and losses.

3.3 Emergence of broadband singularity

We have seen that an ideal cylindrical hyperbolic medium is able to support arbitrarily high angular momentum modes, which results in an arbitrarily high number of scattering channels. Another way to view this is that the hyperbolic form of the dispersion relation allows photons of a certain energy to occupy states that were previously unavailable to them – in fact, an infinite number of states. We can formalize this notion by introducing the concept of a photonic density of states (PDOS) in hyperbolic metamaterials.

Density of states has been central to understanding the behavior of many condensed matter and photonic systems. Indeed, the standard result

$$\frac{dn}{d\omega} = \frac{\omega^2}{\pi^2 c^3} \tag{3.7}$$

for the density of electromagnetic modes in vacuum enters into virtually all computations involving emission or absorption probabilities (after causing many a sleepless night for the late 19th century physicists grappling with the ultraviolet catastrophe). This vacuum expression can be modified by setting up appropriate boundary conditions. As shown by Purcell, radiative properties of an emitter can be strongly altered

inside a resonance cavity, which can enhance mode density [70]. In recent years, density of states has been extensively used in studying the behavior of light in photonic crystals [71] and other photonic nanostructures [72], particularly in the context of enhancing or inhibiting the rate of spontaneous emission.

The studies referenced above use primarily device geometry to influence the density of states. It is not hard to see, however, that the density of states can be also be altered by material properties – for instance, if one neglects local field corrections, it can be shown that in lossless dispersionless dielectrics, Eq. (3.7) is enhanced by a factor n, the index of refraction [73]. The more general treatment must take those two factors into account.

In the case of hyperbolic metamaterials, the density of states is given by

$$\frac{dn}{d\omega} \approx \frac{K_{\max}^3}{12\pi^2} \left| \frac{\epsilon_z}{\epsilon_x} \left(\frac{1}{\epsilon_x} \frac{d\epsilon_x}{d\omega} - \frac{1}{\epsilon_z} \frac{d\epsilon_z}{d\omega} \right) \right|, \tag{3.8}$$

where $K_{\max}$ is the upper momentum cutoff (determined by either the patterning scale of the metamaterial or by losses), and where the $\{\epsilon_x < 0, \epsilon_z > 0\}$ type anisotropy was assumed.

Eq. (3.8) represents substantial enhancement over the photonic density of states in vacuum. This has immediate consequence for emission and absorption of radiation by dipoles in vicinity of hyperbolic metamaterials. In the next section, we will examine the this problem in some detail, comparing the effects of dielectric, metallic, and hyperbolic substrates on radiative lifetime of an emitter. We will find that, indeed, the nature of the substrate material and the associated density of states has a strong impact on fluorescence.

3.4 Radiative decay engineering

3.4.1 Introduction

Interactions between emitters and nanophotonic structures are of central importance in contemporary optical science. Many devices in the fields of sensing, quantum information processing, and plasmonics, among others, may be modeled as dipoles interacting with some (possibly complex) medium.

An important characteristic of a radiating dipole is its rate of energy dissipation. It has long been known that this rate can be modified by the external environment. Much of the past work focused on studying dipole radiation in resonant cavities. In recent years, due to rising interest in waveguide and metamaterial devices, changes in dipole lifetime in close proximity to planar structures or stratified media are often helpful to consider. In this section, we solve the problem of a dipole in the presence of a hyperbolic slab or half-space and study the effect of the increased photonic density of states in material on dipole lifetime.

3.4.2 Radiative lifetime and spontaneous decay rates: general theory

Up until now, when talking about light propagation or refraction involving metamaterials, we simply considered the field harmonics in plane wave (or, in the case of the hyperlens, Bessel function) basis, setting up boundary conditions as needed and using the $\omega(\boldsymbol{k})$ dispersion relations. In this section, we will explicitly put emitters into the picture. It turns out that the standard methods we just mentioned can be readily used to study changes in the dipole lifetime – a key characteristic of an emitter. As a starting point, we need little more than Fresnel reflection coefficients and the ability to decompose the S and P polarizations of the dipole into transverse spatial frequency harmonics. We review these results in Appendix A.

The general expressions for computing power radiated by the dipole comes from Poynting's theorem for harmonic fields:

$$\frac{dW}{dt} = -\frac{1}{2}\int \mathrm{Re}[\boldsymbol{j}^* \cdot \boldsymbol{E}]d\boldsymbol{r} = \frac{\omega}{2}\mathrm{Im}[\boldsymbol{m}^* \cdot \boldsymbol{E}(h\hat{\boldsymbol{z}})], \tag{3.9}$$

where we used the dipole current defined in Eq. (A.11).

We can now use Eq. (A.20) to obtain the Larmor radiation formula for a dipole in vacuum. For this, we simply take the limit of the integrand as $\boldsymbol{r}_\perp \to 0, z \to h$, rewrite the expression in polar coordinates and take the angular integral. Note that the delta-function term in Eq. (A.20) vanishes when taking the imaginary part in Eq. (3.9). We are left with

$$\frac{dW}{dt} = \mathrm{Im}\left\{\frac{i\omega}{16\pi\epsilon_0}\int_0^\infty \left[\frac{k}{q_z}\left(k^2\left(|m_\perp|^2 + 2|m_z|^2\right) + 2q_z^2\left(|m_\perp|^2\right)\right)\right]dk\right\}, \tag{3.10}$$

where $|m_\perp|^2 \equiv |m_x|^2 + |m_y|^2$. Because we are taking the imaginary part, we require the integrand here to be purely real. Due to the q_z term, the integrand is in fact purely real for $k \in [0, \omega/c]$ and purely imaginary for $k > \omega/c$. Picking ω/c as the upper integration limit, we obtain the familiar Larmor formula:

$$\frac{dW}{dt} = \frac{|\boldsymbol{m}|^2\omega^4}{12\pi\epsilon_0 c^3}. \tag{3.11}$$

The same procedure can be used to compute the power radiated by a dipole in the presence of a homogeneous or stratified medium. To do this, Eqs. (A.25) and (A.27) must be taken as the starting point. The integrals are only somewhat more involved. Because of the complex reflection coefficients, we can no longer decompose the integrand into a purely real and imaginary part, and hence the solution remains as an integral over all values of the transverse wave vector component.

We now proceed to compute a closely related quantity, and one that is often of greater practical importance: the decay rate γ. The radiative power dissipated by the dipole can be related to its decay rate via the semiclassical expression[74]

$$\gamma = P/\hbar\omega. \tag{3.12}$$

For any realistic emitter, particularly in the presence of other media, the total decay rate is a sum of radiative (γ_{rad}) and non-radiative (γ_{nr}) contributions. We can define the quantum efficiency η as

$$\eta = \frac{\gamma_{\text{rad}}}{\gamma_{\text{rad}} + \gamma_{\text{nr}}}. \tag{3.13}$$

We are interested in computing the decay rate as a function of the separation distance h between the dipole and the surface. We normalize the decay rate by that of a dipole in free space [meaning that it still admits non-radiative decay channels, but the radiative power is given precisely by Eqs. (3.11) and (3.12)]. We write this decay rate as

$$\tilde{\gamma}(h) = \frac{\gamma}{\gamma_0} = \frac{\gamma_{\text{nr}} + \gamma_{\text{rad}}}{\gamma_{\text{nr}} + P_0/\hbar\omega}, \tag{3.14}$$

where P_0 is given by the Larmor formula, Eq. (3.11). Because of the presence of scattered fields, the radiative decay rate term in the numerator can be written as $\gamma_{\text{rad}} = (P_0 + P_s)/\hbar\omega$, where P_s gives the radiated power computed via Eq. (3.9) applied only to the reflected fields. Furthermore, assuming the quantum efficiency in Eq. (3.13) is independent of h, we can express γ_{nr} in terms of η and P_0, resulting in a very simple expression for the reduced decay rate:

$$\tilde{\gamma}(h) = 1 + \eta\frac{P_s}{P_0}. \tag{3.15}$$

It is straightforward to compute P_s by starting with Eqs. (A.25) and (A.27), keeping only the terms with the reflection coefficients r_p and r_s. The result is

$$\tilde{\gamma}(h) = 1 + \eta\,\mathrm{Re}\frac{3c^3}{4|\boldsymbol{m}|^2\omega^3}\int_0^\infty k_x\,dk_x\left[r_s(k_x)|m_\perp|^2\left(k_x^2+q_z^2\right) - \right.$$
$$\left. -r_p(k_x)\left(|m_\perp|^2 q_z^2 - 2|m_z|^2 k_x^2\right)\right]\frac{e^{2ihq_z}}{q_z} \quad (3.16)$$

(we emphasize that the integration variable is the transverse wave vector coordinate k_x). It is apparent from Eq. (3.16) that aside from the position and orientation of the emitter, the key contribution to its lifetime (relative to the vacuum case) comes from the reflection properties of the medium. This is not surprising, since these properties determine the total strength of the electric field at the dipole, which, as we have seen, affects the radiated power. More importantly, the coefficients r_p and r_s reveal details about the coupling of energy from the emitter into the medium. Indeed, different materials may predominantly transmit, absorb, or reflect energy; in addition, they may support a variety of guided modes, leaky modes, or surface excitations. All these phenomena can be gleaned from the behavior of reflection coefficients, and can have a dramatic impact on dipole lifetime.

3.4.3 Dipole lifetime near an interface: effects of metals, dielectrics, and hyperbolic materials

We now proceed to illustrate the effects of proximity of different materials on the lifetime of an emitter. In particular, we discuss the differences between dielectrics, metals, and hyperbolic media. The interaction of electromagnetic waves with these three classes of materials reveals rather different physics, which has a direct impact

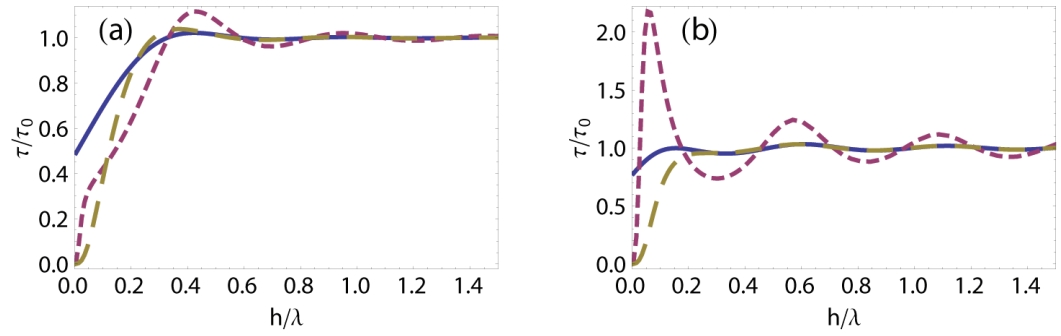

Figure 3.3: Normalized lifetime of a vertically [panel (a)] and horizontally [panel (b)] oriented dipole as dependent on distance h from a half-infinite material in the horizontal plane. Materials considered are dielectric, $\epsilon = 2$ (solid curves), strongly anisotropic metamaterial, $\{\epsilon_x, \epsilon_y\} = \{2, -5\}$ (dashed curves), and metal, $\epsilon = -30+8i$ (finely dashed curves).

on dipole decay rate. We shall see these fundamental differences most dramatically in the limit of very close proximity ($h \ll \lambda$) and low loss.

In Fig. 3.3 we plot the normalized lifetime ($\tau/\tau_0 \equiv \tilde{\gamma}^{-1}$) of a dipole as a function of its height above a substrate. The lifetime of the dipole in the vicinity of a medium (closer than about one vacuum wavelength) is seen to depend strongly on the nature of the material. Here we consider the case of a lossless dielectric, a metal (with loss), and a strongly anisotropic (hyperbolic) metamaterial (lossless). For the metallic substrate, the dipole lifetime approaches zero as the separation between metal and dipole vanishes: the emission is effectively quenched [75, 76]. Likewise, the dipole lifetime tends to zero when metal is replaced with a hyperbolic medium. The dielectric substrate, in contrast, never completely suppresses the fluorescence.

We can understand the origin of this different behavior by examining the integrand of Eq. (3.16) in the limit $h \ll \lambda$. In this limit, contributions to the integrand that arise from large values of the transverse wave vector, $k_x \gg \omega/c$, become important. With this in mind, we assume $k_x \in [\omega/c, \infty]$ and write $q_z \equiv i\kappa = i\sqrt{k_x^2 - (\omega/c)^2}$. For simplicity here (and for the rest of this chapter) we assume the dipole to be vertically

oriented ($\boldsymbol{m} = \hat{\boldsymbol{z}}$). We can then write Eq. (3.16) as

$$\tilde{\gamma}(h) \simeq 1 + \eta \frac{3}{2} \frac{1}{(\omega/c)^3} \int_{\omega/c}^{\infty} \mathrm{Im}(r_p) \frac{k_x^3}{\kappa} e^{-2h\kappa} dk_x. \tag{3.17}$$

Assuming that the leading contribution to the integral in Eq. (3.16) comes from large wave vectors ($k_x \gg \omega/c$) we can write $\kappa \approx k_x$. Furthermore, r_p (as given by Eq. (A.31)) becomes independent of k_x to leading order. We can, therefore, obtain a simple analytical solution for the decay rate. For the case of metallic substrate, it is

$$\begin{aligned} \tilde{\gamma}(h) &\simeq 1 + \eta \frac{3}{4} \frac{1}{(h\omega/c)^3} \mathrm{Im}\left(\frac{\epsilon - 1}{\epsilon + 1}\right) \\ &= 1 + \eta \frac{3}{2} \frac{1}{(h\omega/c)^3} \frac{\epsilon''}{(1+\epsilon')^2 + \epsilon''^2}, \end{aligned} \tag{3.18}$$

where we used the usual definition $\epsilon \equiv \epsilon' + i\epsilon''$.

We conclude that in the vicinity of a lossy substrate (be it metal or dielectric) the emitter lifetime vanishes as h^3 as the separation h between the emitter and the substrate goes to zero. The physical origin of this dependence is the non-radiative transfer of energy into leaky waves propagating along the surface of the substrate, which come to dominate over other decay channels at very close distances [77]. In light of this discussion, it is reasonable that the lifetime of an emitter plotted in Fig. 3.3 tends to zero for a lossy metal, but approaches a finite limiting value in the case of a lossless dielectric. Furthermore, we can understand why a *lossless* hyperbolic metamaterial substrate induces a quenching effect similar to that observed for lossy materials. By examining Eqs. (A.29) and (A.31) we can see that for the hyperbolic material with $\epsilon_x > 0$ and $\epsilon_z < 0$, $\mathrm{Im}(r_p) \neq 0$ even if the dielectric tensor is purely real; as a result, we get a similar h^3 dependence of dipole lifetime on height above the substrate. In this case, the energy is transferred to the bulk propagating waves inside the hyperbolic material. Indeed, one can view this transfer of energy as arising

from the increased (formally infinite) density of photonic states that characterizes the hyperbolic medium [78].

3.4.4 The role of geometry: dipole lifetime near waveguides

In addition to the basic material parameters, device geometry plays a significant role in determining radiative decay characteristics. To provide a simple illustration of this, we turn out attention to slab waveguides (note that a filled half-space can be regarded as a limiting case of a waveguide with thickness $d \to \infty$). To determine radiative decay rate in the vicinity of a waveguide, we use Eqs. (3.16) and (3.17) with r_p given by

$$r_p = \frac{\frac{\epsilon_x^{(2)} q_z^{(1)}}{\epsilon_x^{(1)} q_z^{(2)}} - \frac{\epsilon_x^{(1)} q_z^{(2)}}{\epsilon_x^{(2)} q_z^{(1)}}}{\frac{\epsilon_x^{(2)} q_z^{(1)}}{\epsilon_x^{(1)} q_z^{(2)}} + \frac{\epsilon_x^{(1)} q_z^{(2)}}{\epsilon_x^{(2)} q_z^{(1)}} + 2\,i\cot(dq_z^{(2)})}, \tag{3.19}$$

where $q_z^{(2)}$ is given by Eq. (A.29), $q_z^{(1)} = \sqrt{(\omega/c)^2 - k_x^2}$, and $\epsilon_x^{(1)} = 1$ for the case of dipole in vacuum that we treat here.

In Fig. 3.4 we plot the normalized lifetime τ of the vertically oriented dipole as a function of its height above a metallic or hyperbolic waveguide (note the logarithmic scale on both axes). The different panels correspond to different waveguide thicknesses ($d = \infty$, $d = 0.01\lambda$, and $d = 0.001\lambda$), and metallic and hyperbolic curves are plotted on the same axes for ease of comparison; in addition, we plot the lifetime for several values of material losses ($\epsilon'' \in \{0, 0.01, 1\}$). Since the excitation of lossy waves provides an important decay channel (as shown above), it is instructive to consider the dipole lifetime in the limit of zero losses, gradually increasing them to more realistic values. It is interesting to note that even though the zero loss assumption substantially simplifies many problems in optics and electromagnetics, in this particular case it leads to increased difficulties, since the denominator of Eq. (3.19) acquires infinitely sharp resonances (two, corresponding to the excitation of surface plasmons in the case of the metallic slab, and infinitely many, corresponding to guided

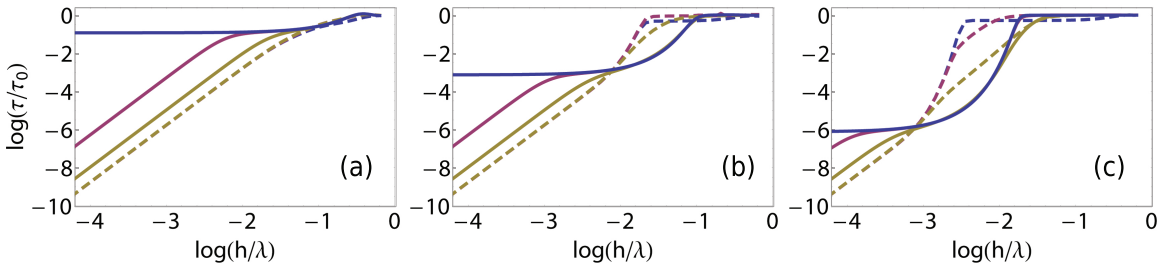

Figure 3.4: Normalized lifetime of a vertically oriented dipole vs. distance from a metallic ($\epsilon' = -5$; solid curves) or hyperbolic ($\{\epsilon'_x, \epsilon'_y\} = \{5, -5\}$; dashed curves) waveguide; note the log-log scale. Different curves correspond to varying the amount of loss ($\epsilon'' \in \{0, 0.01, 1\}$), with higher losses resulting in lower lifetime. Panels (a), (b), (c) and (d) correspond to waveguide thicknesses $d = \infty$, $d = 0.1\lambda$, $d = 0.01\lambda$ and $d = 0.001\lambda$ respectively.

wave modes for a slab of hyperbolic material), causing simple numerical integration techniques to fail. However, the zero-loss limit admits a semi-analytic solution (see Appendix B), simplifying its treatment.

The analysis of Fig. 3.4 yields several interesting conclusions. Panel (a) allows for a clear comparison between half-infinite metallic and hyperbolic substrates as discussed above. The $\tau \sim h^3$ dependence for both types of materials shows clearly on the log-log scale. Furthermore, for the case of hyperbolic medium the dipole lifetime is *independent* of the amount of losses. In contrast, for a metallic substrate the dipole lifetime is a constant (for $h \ll \lambda$) in the zero-loss limit, and decreases with increasing loss (as expected from Eq. (3.18)), matching the lifetime of the hyperbolic medium only for a relatively high loss of $\epsilon'' \approx 5$. This suggests that excitation of propagating high-k_x waves in the hyperbolic material provides a decay channel for the emitter that is more efficient than coupling to lossy surface waves. By examining panels (b) and (d), we can identify two distinct regimes: $h \ll d \ll \lambda$ and $d \lesssim h \ll \lambda$. In the first regime, there is little difference between the waveguide systems and the half-infinite substrate; indeed, the only readily quantifiable effect appears in the lossless limit of a metallic substrate, where lifetime drops with decreasing d ($\log \tau \sim \log d$). Ideal loss-

less hyperbolic waveguides, on the other hand, support an infinite number of modes for an arbitrary thickness; this singularity in the density of states implies that in the $h \ll d$ limit the waveguide thickness has no effect on decay rates even in the case of zero losses.

In the second regime, $d \lesssim h \ll \lambda$, we observe that for metallic waveguides dipole lifetime drops relative to that of a half-infinite substrate, while for hyperbolic systems the lifetime *increases*. In fact, it can be shown (and is evident from the plots, in particular, Fig. 3.4(c)) that the lifetime near a metal slab behaves as h^4 [79] (hyperbolic medium, in contrast, retains the h^3 dependence for sufficiently high losses). The reason for this is that for hyperbolic waveguides the coupling to high-k_x propagating modes is reduced for $d \lesssim h \ll \lambda$, while for the metals, coupling to surface plasmon modes becomes an important non-radiative decay channel, leading to lower lifetimes.

3.5 Conclusion

This chapter explored some of the fundamental features of hyperbolic dispersion. We started with the familiar observation that hyperbolas are unbounded, and discussed its implications in cylindrical geometry. We found that solutions of Maxwell's equations could be represented as discrete angular momentum states with non-vanishing field everywhere for arbitrarily high values of angular momentum – the behavior that is unique to hyperbolic materials. Examining this result from the viewpoint of scattering theory, we found that it readily suggest a platform for super-resolved imaging. In addition, we can view this result as a consequence of divergent photonic density of states, which has implications far beyond the imaging problem. Singularity in PDOS opens the possibility for dramatically modifying emission or absorption properties of materials, leading to many possible applications in communications or energy harvesting.

In the next chapter, we will continue our exploration of novel devices enabled by the hyperbolic dispersion relation. We will give a detailed account of light propagation in HMM-filled waveguides and show that in planar nanophotonic devices, the cut-off free nature of hyperbolic dispersion has a particular chance to shine.

Chapter 4

Guided waves in hyperbolic metamaterials

4.1 Introduction

In the previous chapter, we have alluded to the importance of boundary conditions as we consider ways in which bulk metamaterials could be fashioned into useful devices. The simplest non-trivial boundary conditions are set up by an interface between two half-infinite materials. Indeed, without this boundary condition many of the basic phenomena we have studied in metamaterials (e.g. negative refraction) would be ill-defined. Despite its simplicity, considering a single interface allowed us to learn much about the refractive behavior of light in hyperbolic materials, and allowed us to compute dipole fluorescence enhancement due to the presence of a metamaterial.

Most optical devices, however, are of a finite extent. Discussions of imaging or light guiding and confinement necessarily deal with systems that are bounded in two or three dimensions. In this chapter we will consider planar, quasi-two-dimensional systems made of hyperbolic metamaterials that support (or can otherwise couple to) propagating modes.

4.2 Mirror waveguide

As a simple example, yet one that will capture many of the unusual characteristics of HMM waveguides, let us consider guided mode solutions for a planar slab of thickness d with perfectly conducting walls. (Since these walls are perfectly reflecting, this setup is known as the *mirror waveguide*.) Suppose that the boundaries of the waveguide lie at $x = 0$ and $x = d$, and that guided modes propagate in the z direction. We assume that the waveguide is filled with a uniaxial anisotropic material characterized by dielectric constants $\epsilon_x \equiv \epsilon_\perp$ (for field components transverse to the waveguide) and $\epsilon_{y,z} \equiv \epsilon_\parallel$. In this case, only TM modes are affected by the anisotropy much like only the extraordinary waves are affected by the anisotropy of bulk uniaxial media. (To regulate the propagation of TE modes in a similar manner, magnetic anisotropy would be required.) The solution for TM modes propagating in the waveguide described above is [35]

$$\boldsymbol{E}(\boldsymbol{r},t) = E_0 \left[-i\frac{\beta}{\epsilon_\perp}\cos(\kappa x)\hat{\boldsymbol{x}} + \frac{\kappa}{\epsilon_\parallel}\sin(\kappa x)\hat{\boldsymbol{z}} \right] \exp[-i(\beta z - \omega t)], \tag{4.1}$$

where $\kappa = m\pi/d$, and κ and β satisfy the usual dispersion relation for uniaxial anisotropic media:

$$\frac{\beta^2}{\epsilon_\perp} + \frac{\kappa^2}{\epsilon_\parallel} = \frac{\omega^2}{c^2}. \tag{4.2}$$

We can learn a lot about the behavior of hyperbolic waveguide systems simply by studying how the choice of signs for $\epsilon_\parallel$ and $\epsilon_\perp$ affects the solutions of Eq. (4.2). First, observe that in the isotropic case ($\epsilon_\parallel = \epsilon_\perp$), the above expressions for the field components and dispersion relation reduce to the familiar results for a metallic waveguide. As is well known, the number of allowed modes in traditional waveguides

is limited; this can be easily seen by rewriting Eq. (4.2) as

$$\frac{m\pi}{d} = \kappa = \sqrt{\epsilon_\parallel}\sqrt{\frac{\omega^2}{c^2} - \frac{\beta^2}{\epsilon_\perp}} \tag{4.3}$$

and imposing the conditions that m, d be real and positive. In the isotropic case, this implies that $\kappa \leq \sqrt{\epsilon}\omega/c$, which gives the following value for the maximum supported mode $m_{\max}$:

$$m_{\max} = \left\lfloor \frac{d\sqrt{\epsilon}\omega/c}{\pi} \right\rfloor \tag{4.4}$$

($\lfloor\cdot\rfloor$ and $\lceil\cdot\rceil$ denote floor and ceiling functions).

This expression changes only slightly if the isotropy assumption is relaxed, but both $\epsilon_\parallel$ and $\epsilon_\perp$ are assumed to be positive: we only need to replace ϵ with $\epsilon_\parallel$ in Eq. (4.4). However, if the *signs* of $\epsilon_\parallel$ and $\epsilon_\perp$ differ, the situation changes dramatically. Consider, for instance, the case $\{\epsilon_\perp < 0,\ \epsilon_\parallel > 0\}$. The condition for Eq. (4.2) to be satisfied now reads $\kappa \geq \sqrt{\epsilon_\parallel}\omega/c$, leading to

$$m_{\min} = \left\lceil \frac{d\sqrt{\epsilon_\parallel}\omega/c}{\pi} \right\rceil . \tag{4.5}$$

Rather than having a maximum mode cutoff, the guided modes are now bounded *from below*. By adjusting the values of d and $\epsilon_\parallel$ it is possible to allow *all* modes to propagate in a waveguide, or to elevate the minimum cut-off threshold $m_{\min}$ to admit only high order modes.

Consider now the case where $\{\epsilon_\perp > 0,\ \epsilon_\parallel < 0\}$. It is possible to satisfy Eq. (4.3) for *any* value of d and $\epsilon_{\perp,\parallel}$. In other words, in the idealized system, all modes always propagate. These observations can be readily interpreted in terms of the PDOS singularity discussed in the last chapter. The diverging density of states was entirely due to the hyperbolic form of the dispersion relation. Here, the boundary conditions

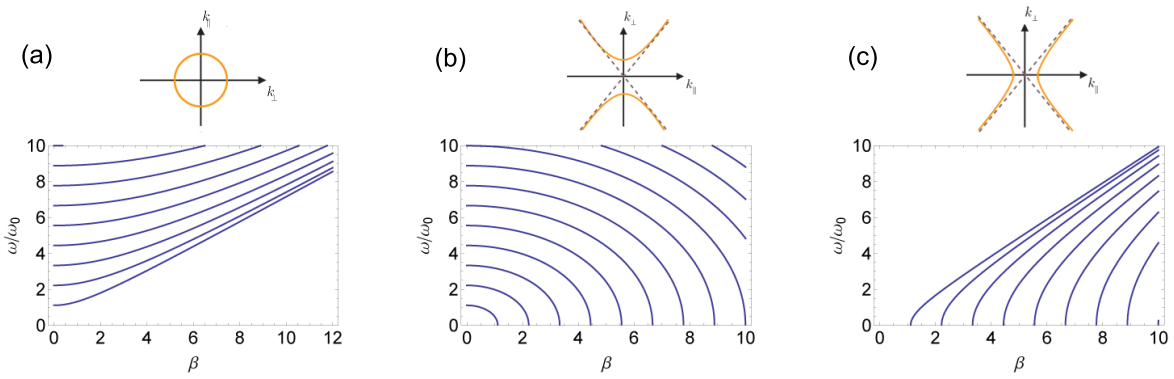

Figure 4.1: Dispersion relations for a metallic waveguide with hyperbolic material core: (a) "regular" waveguide ($\epsilon_\perp = \epsilon_\parallel = 2$), (b) $\{\epsilon_\perp < 0,\ \epsilon_\parallel > 0\}$: $\{\epsilon_\perp,\ \epsilon_\parallel\} = \{-2, 2\}$ (c) $\{\epsilon_\perp > 0,\ \epsilon_\parallel < 0\}$: $\{\epsilon_\perp,\ \epsilon_\parallel\} = \{2, -2\}$. Waveguide propagation vector β is plotted in units of ω_0/c.

discretize the set of allowed wave vectors for a given energy, but there is still an infinite number of them (of course, as before, losses and patterning scale impose an upper bound on the mode density).

In Fig. 4.1 we plot the dispersion curves of Eq. (4.2) for the three material parameter scenarios discussed above. Panel (a) depicts the familiar results for isotropic mirror waveguides, panel (b) treats the case $\{\epsilon_\perp < 0,\ \epsilon_\parallel > 0\}$. The existence of $m_{\min}$ and $m_{\max}$ for a fixed frequency ω_0 can easily be seen in panels (a) and (b), respectively, by drawing a horizontal line $\omega = \omega_0$. Panel (c) illustrates the case $\{\epsilon_\perp > 0,\ \epsilon_\parallel < 0\}$; it is apparent that solutions exist for every mode, regardless of the frequency.

Furthermore, Fig. 4.1 shows unusual behavior of *group velocity* in HMM waveguides. Indeed, since the group velocity for the guided modes, $v_g = \partial\omega/\partial\beta$, corresponds to the slope of lines tangent to the dispersion curves, panel (b) suggests that the group velocity for *all* modes in the $\{\epsilon_\perp < 0,\ \epsilon_\parallel > 0\}$ waveguide is negative! Perhaps even more surprising is that for $\{\epsilon_\perp > 0,\ \epsilon_\parallel < 0\}$ materials, the group velocity can not only exceed the velocity of light inside the waveguide core, but reach arbitrarily high values, becoming infinite for $\omega = 0$, as evident from panel (c). These unusual conclusions can be checked algebraically. Differentiating Eq. (4.2) we obtain

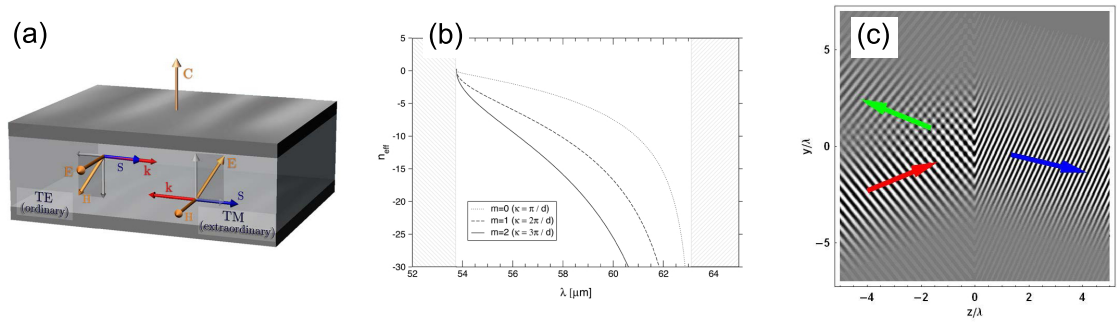

Figure 4.2: Negative refraction with an HMM metallic waveguide: (a) Schematics of a metallic waveguide showing directions of the TE and TM fields (b) Plot of the mode-dependent effective refractive index for a waveguide with bismuth core (c) Illustration of negative refraction inside the waveguide with an interface between bismuth and an isotropic dielectric

$$\frac{\partial \omega}{\partial \beta} = \frac{c^2}{\epsilon_\perp} \frac{1}{\omega/\beta} = \frac{c^2}{\epsilon_\perp} \frac{1}{v_\phi}, \tag{4.6}$$

where v_ϕ is the phase velocity. For $\epsilon_\perp < 0$ we see immediately that the phase velocity and the group velocity are of different signs. This explains the apparent negative sign of the group velocity in Fig. 4.1(b). We can also understand the origins of $v_g > c$: when the signs of the $\boldsymbol{\epsilon}$ tensor components differ, Eq. (4.3) shows that for any given mode it is possible to pick values of β to make the frequency ω arbitrarily small. Accordingly, arbitrarily small values of v_ϕ can be attained. From Eq. (4.6) it follows that this leads to infinitely high values of v_g. [Note that in "regular" mirror waveguides v_ϕ can become arbitrarily large, becoming infinite at cut-off frequencies for a given mode. This corresponds to the line $\beta = 0$ in Fig. 4.1(a).]

It is worth noting that emergence of negative group velocities can be observed by examining the dispersion relation for bulk $\{\epsilon_\perp < 0,\ \epsilon_\parallel > 0\}$ material and considering the ray optics description of the mirror waveguide. Indeed, let us represent the waveguide mode by a plane wave with wave vector $\boldsymbol{k}$ bouncing between the two reflecting boundaries. Due to the $\{\epsilon_\perp < 0,\ \epsilon_\parallel > 0\}$ anisotropy, the components of $\boldsymbol{S}$ and $\boldsymbol{k}$ along the waveguide, S_z and k_z, differ in sign. The guided mode is constructed

out of the multiply reflecting plane waves; it can be seen that S_z represents the net energy flow in the mode, while k_z coincides with the mode propagation constant β. We therefore arrive at the same conclusion as before – that the direction of the phase fronts is opposite to the direction of the energy flow.

In this sense, the guided modes mimic the refractive behavior of magnetic ($\epsilon < 0$, $\mu < 0$) negative-index materials. Indeed, we can rewrite the metallic waveguide dispersion relation (4.2) as

$$\beta_z^2 + \beta_y^2 = \epsilon\,\nu\frac{\omega^2}{c^2}, \tag{4.7}$$

with $\nu = \left(1 - \kappa^2 c^2/\epsilon_{\|}\,\omega^2\right)$ where $\epsilon = \epsilon_{\perp}(\epsilon_{\|})$ for the TM(TE) modes. The effective refractive index for propagating waveguide modes in this system is given by $n_{\text{eff}}^2 = \epsilon\,\nu$. To support propagating modes, ϵ and ν must have the same sign; in the case $\epsilon < 0$, $\nu < 0$ the phase velocity of the waves is negative [30]; accordingly, the refractive index is given by

$$n_{\text{eff}} = -\sqrt{\epsilon_{\perp}\,\nu}. \tag{4.8}$$

In Fig. 4.2(b) we plot the effective index using the material parameters of bismuth, which is a naturally-occurring hyperbolic material for THz wavelengths (see Sec. 2.3.1). Furthermore, if we consider the waveguide which is filled with a regular dielectric on the left and with an $\epsilon_{\perp} < 0$ anisotropic material on the right, we find that a mode with propagation vector $\boldsymbol{\beta} = \beta_y\hat{\boldsymbol{y}} + \beta_z\hat{\boldsymbol{z}}$ incident on this boundary refracts negatively. We illustrate this in Fig. 4.2, where we plot refraction of a two-dimensional wave packet formed by the propagating modes of the waveguide. Notice that not only the energy flow direction, but also the phase fronts reveal negative refraction, unlike the examples we saw in Chapter 2, where negative refraction was only observed in the Poynting vector. In these previous examples, it was the large Poynting vector walk-off that enabled all-angle negative refraction; in contrast, here, it is the negative phase velocity that accounts for the unconventional refractive behavior.

The unusual features of HMM waveguides delineated above hint at many interesting potential applications. First, the optical power in a given mode is proportional to β, which, asymptotically, is linear in the mode number m. Thus, it might be possible to concentrate unusually high fields in a subwavelength waveguide, an impossible feat with conventional materials. Such a capability would be of great interest in developing nonlinear devices.

Secondly, we can observe that mode profiles for high-m solutions exhibit rapid oscillations, i.e. correspond to high spatial frequencies. Such high order modes would be able to couple to evanescent fields of finely structured objects, which are also characterized by high transverse spatial frequencies. These high spatial frequencies carry the information about the object's subwavelength features — the information typically lost as a consequence of the diffraction limit. This ability to guide waves that would exponentially decay in an ordinary medium is of great interest in constructing subwavelength imaging devices.

Third, it is evident from the above discussions that idealized HMM waveguides admit an unbounded number of modes for a fixed frequency. This means that the density of states in such systems is, in principle, infinite. This has important implications for emission and absorption of radiation within (or in the vicinity of) HMM structures.

Finally, the broad range of group velocities supported by HMM waveguides can provide an avenue for designing slow and fast light devices in the solid state. It is important to note that the hyperbolic dispersion relations in the bulk may be considered as a non-resonant effect, which opens the possibility for higher bandwidths and lower losses compared to the traditional ways of implementing slow light devices.

4.3 Planar dielectric waveguides and slow light

4.3.1 Dielectric waveguide basics

Consider the waveguide with $\{\epsilon_\perp < 0,\ \epsilon_\parallel > 0\}$, whose modal dispersion for the "metallic" boundary conditions yields negative group velocities [Fig. 4.1(b)]. In this section, we will discuss effects that arise when the perfectly conducting metallic walls of the waveguide are replaced with a dielectric cladding. The solution of this problem is conceptually similar to that of the isotropic planar slab waveguide, which can be found in standard textbooks [80]. Let us review the key features of the slab waveguide:

- For a given frequency, a finite number of modes is supported. The cut-off mode number is determined by the waveguide thickness. The $m = 0$ mode is always supported.

- The group velocity of the modes lies between the velocity of light in the core and the cladding: $v_{\text{cladding}} < v_g < v_{\text{core}}$. Note that higher order modes travel slower, which is *not* the case in metallic waveguides.

- The above modal dispersion can be explained using the Goos-Hänchen effect: the lateral shift of a mode's classical ray trajectory can be associated with a velocity which decreases with increasing mode number.

What happens to the group velocity of a mode when v_{core} becomes negative? In this case, energy flux in the core is antiparallel to the wave vector. However, the energy flux in the waveguide cladding (which we assume to be made of regular, isotropic dielectric) is, as usual, collinear with the wave vector. It has been suggested by Engheta that balancing positive energy flux in a dielectric with negative energy flux in a DNG material (i.e. medium with simultaneously negative values of dielectric permittivity and magnetic permeability) can be used to effectively slow the group velocity of propagating modes, creating a "resonator without mirrors" [81]. Indeed,

these considerations also hold for HMM waveguides. As we shall see, there exists a value of the light frequency ω (and the waveguide thickness d) such that the negative energy flux inside the waveguide is nearly balanced by the positive energy flux outside, leading to a dramatic suppression of the signal velocity.

4.3.2 Slow light in TM modes using ϵ anisotropy

We first solve the general problem of TM wave propagation in a planar waveguide with uniaxial core. The electric field in the three regions of the waveguide can be expressed as

$$\vec{E}_1 = (A_x\hat{x} + A_z\hat{z})\,\mathrm{e}^{-\kappa_1 x}\mathrm{e}^{-ik_z z} \tag{9a}$$

$$\vec{E}_2 = [(B_x \sin k_x x + C_x \cos k_x x)\,\hat{x} + (B_z \sin k_x x + C_z \cos k_x x)\,\hat{z}]\,\mathrm{e}^{-ik_z z} \tag{9b}$$

$$\vec{E}_3 = (D_x\hat{x} + D_z\hat{z})\,\mathrm{e}^{\kappa_3 x}\mathrm{e}^{-ik_z z}. \tag{9c}$$

Requiring continuity at the boundaries and compliance with Maxwell's equations, we can obtain the guidance condition in the form

$$\frac{\kappa_i}{\epsilon_{d_i}} = f_j(k_x, k_z; \kappa_j), \tag{10}$$

where $(i, j) \in \{(1, 3), (3, 1)\}$ and

$$f_j(k_x, k_z; \kappa_j) = \left(\frac{k_x}{\epsilon_z}\right)\left(\frac{\epsilon_{d_j} k_x - \epsilon_z \kappa_j \cot k_x d}{\epsilon_z \kappa_j + \epsilon_{d_j} k_x \cot k_x d}\right).$$

Dispersion relations in the three regions are

$$\frac{k_z^2}{\epsilon_x} + \frac{k_x^2}{\epsilon_z} = \frac{\omega^2}{c^2} \tag{11}$$

$$\frac{k_z^2 - \kappa_i^2}{\epsilon_{d_i}} = \frac{\omega^2}{c^2}, \quad i \in \{1, 3\}. \tag{12}$$

For the case $\epsilon_{d_1} = \epsilon_{d_3} \equiv \epsilon_d$ these equations can be combined as

$$\frac{\kappa^2}{\epsilon_x} + \frac{k_x^2}{\epsilon_z} = \left(1 - \frac{\epsilon_d}{\epsilon_x}\right) \frac{\omega^2}{c^2}, \tag{13}$$

while the guidance condition becomes

$$\kappa = k_x \frac{\epsilon_d}{\epsilon_z} \begin{cases} \tan \frac{k_x d}{2} & \text{(odd modes)} \\ -\cot \frac{k_x d}{2} & \text{(even modes).} \end{cases} \tag{14}$$

Finally, k_x may be expressed through k_z and ω using Eq. (11). We thereby obtain a set of transcendental equations, which may be solved graphically or numerically to yield ω vs. k_z dispersion curves.

A particular feature of an anisotropic waveguide is that propagating TM modes can exist for various *sign combinations* of ϵ_x and ϵ_z. For $\epsilon_x,\ \epsilon_z > 0$ the modes resemble those in an isotropic waveguide, while for $\epsilon_x,\ \epsilon_z < 0$ propagating solutions vanish. If only *one* of the ϵ_x, ϵ_z is negative, propagating solutions exist, and their behavior is strongly affected by the altered character of the dispersion relation.

The most prominent impact results in the case $\epsilon_x < 0,\ \epsilon_z > 0$. As discussed in the previous section, this leads to $S_z = S < 0$, i.e. negative energy flux in the waveguide core. This choice of signs for ϵ_x and ϵ_z has additional implications for the modes, as evident from Eq. (13). When $\epsilon_x > 0$, this equation describes an ellipse. Consequently, simultaneous solutions of Eqs. (13) and (14) are possible only for a

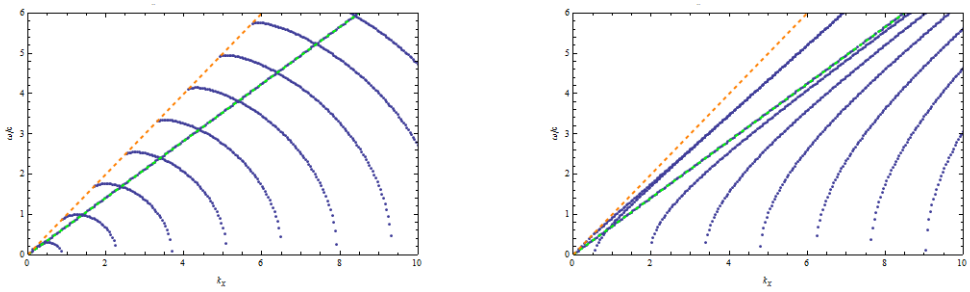

Figure 4.3: Dispersion curves for TM modes of the slow light waveguide (neglecting material dispersion). (a) $\{\epsilon_x < 0,\, \epsilon_z > 0\}$; (b) $\{\epsilon_x > 0,\, \epsilon_z < 0\}$. Light lines in air and in the waveguide are shown as straight lines.

range of k_x values up to some cut-off transverse wave vector $k_{x\,\max}$ (this reflects the fact that high k_x modes of dielectric waveguides cannot meet the guidance conditions). However, as discussed in the previous section, when $\epsilon_x < 0$, Eq. (13) describes a hyperbola. Arbitrarily large values of k_x can now satisfy Eq. (13) and simultaneously solve Eq. (14). We see that this waveguide has *no large k_x cutoff* (instead, there exists a minimum allowed value of k_x). Finally, we note that no-cutoff mode solutions are also possible for the case $\epsilon_x > 0,\ \epsilon_z < 0$, in which case Eq. (13) is still hyperbolic, but with κ as the major axis coordinate.

In Fig. 4.3 we plot dispersion curves of the guided modes resulting from solving Equations (13) and (14) (with a negative value of the transverse permittivity ϵ_x). In panel (a) we consider the $\{\epsilon_x < 0,\, \epsilon_z > 0\}$ anisotropy. For every guided mode we observe regions with both positive group velocity (most of the energy travels in the waveguide cladding) and negative group velocity (most of the energy is in the core). Furthermore, it is evident that for each mode there exists the value of the signal frequency ω_0 corresponding to an extremely strong suppression of the group velocity. Panel (b), which illustrates the $\{\epsilon_x > 0,\, \epsilon_z < 0\}$ anisotropy, shows the unbounded nature of the modes with increasing k_x, but no slow light modes.

While Fig. 4.3 provides a useful qualitative illustration of low group velocity modes in HMM waveguides, realistic models of such devices must take into account the dis-

persive and lossy nature of materials. As discussed in Chapter 2, there exist several possible realizations of $\{\epsilon_x < 0,\ \epsilon_z > 0\}$ materials, the simplest of which is a planar stack of alternating plasmonic and dielectric layers. As we saw, the negative permittivity of plasmonic layers can be obtained from free carriers (in the case of highly doped semiconductors or metals), or from phonon resonances. In our model of the layered waveguide core, we choose silicon carbide (which falls into the latter group) as the $\epsilon < 0$ component of a planar metamaterial. SiC is a wide bandgap, environmentally robust semiconductor with multiple existing and prospective applications in optoelectronics, power electronics, MEMS, sensors, and, of course, metamaterials [56, 57]. Its dielectric function is given by

$$\epsilon_{\mathrm{SiC}} = \epsilon_\infty \frac{\omega^2 - \omega_{\mathrm{LO}}^2 + i\gamma\omega}{\omega^2 - \omega_{\mathrm{TO}}^2 + i\gamma\omega}, \tag{15}$$

where ω_{LO}=972 cm^{-1}, ω_{TO}=796 cm^{-1}, $\epsilon_\infty = -6.5$, and γ=5 cm^{-1} [57, 82]. The resonant behavior results in $\epsilon_{\mathrm{SiC}} < 0$ for the wavelengths of 10.3 – 12.5 μm. Accordingly, we model the anisotropic waveguide core as a metamaterial composed of interleaved SiC and SiO_2 ($\epsilon \simeq 3.9$) layers [Fig. 4.4(a)], with the SiC volume fraction N_c=50%. The dispersive dielectric functions of the layered composite are illustrated in Fig. 4.4(b). For wavelengths between 10.3 and 11 μm we find the $\{\epsilon_x < 0,\ \epsilon_z > 0\}$ region; we denote the center of this frequency interval as ω^*.

In Fig. 4.5(a) we plot the numerically calculated guided mode dispersion curves of the air-clad ($\epsilon_d = 1$) waveguide with the SiC/SiO_2 metamaterial core. Values of $\omega/\omega^* \gtrsim 1.1$ ($\lambda \lesssim 10.3$ μm) cover the region where $\epsilon_x',\ \epsilon_z' > 0$. The mode dispersion curves in this region correspond to the usual guided TM modes of a dielectric waveguide. Curves in the range $0.85 \lesssim \omega/\omega^* \lesssim 0.9$ (λ = 11 – 12.6 μm) represent the $\epsilon_x' > 0,\ \epsilon_z' < 0$ modes, which we do not treat here. Finally, the spectral region

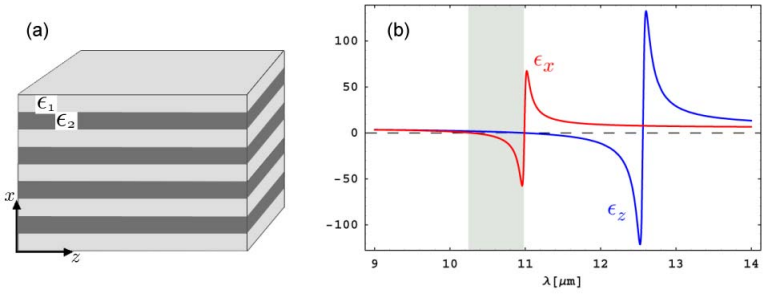

Figure 4.4: (a) Proposed implementation of the slow light waveguide: the core presents a planar stack of SiC/SiO_2 layers, with layer thickness $d \ll \lambda$. (b) Dielectric constants (real parts) for the SiC/SiO_2 stack. Shaded region indicates the regime where $\epsilon_x < 0$, $\epsilon_z > 0$.

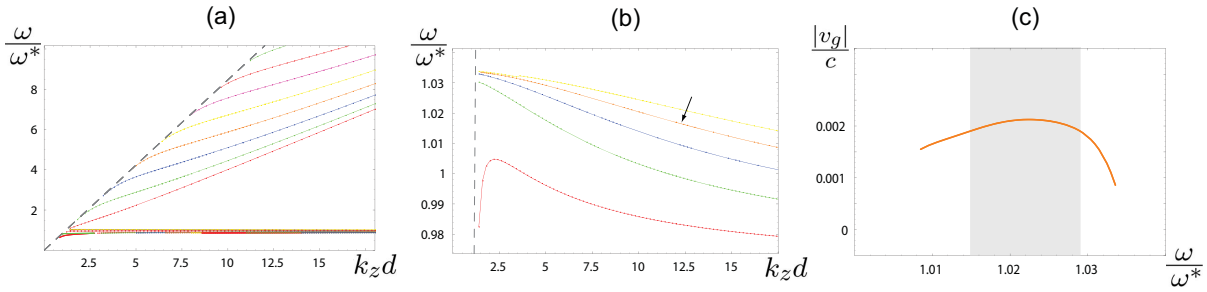

Figure 4.5: (a) Dispersion curves for a waveguide with air cladding ($\epsilon_d = 1$) and SiC/SiO_2 metamaterial core. The characteristic planar waveguide dispersion curves are evident in the region $\omega/\omega^* \gtrsim 1.1$, where ω^* is the center of the $\{\epsilon'_x < 0,\ \epsilon'_z > 0\}$ region. (b) Negative index modes in the $\{\epsilon'_x < 0,\ \epsilon'_z > 0\}$ region. (c) Magnitude of the group velocity of the fourth order negative index mode [indicated by the arrow in (b)]. Shaded region indicates $\lesssim 10\%$ relative change in group velocity. The spectral width of this region is 390 GHz.

$0.9 \lesssim \omega/\omega^* \lesssim 1.1$ ($\lambda = 10.3 - 11$ μm) corresponds to $\epsilon'_x < 0,\ \epsilon'_z > 0$ – the requirement for negative index modes.

This region is examined in Fig. 4.5(b). We note that the dispersion curves of modes in the figure appear qualitatively similar to those of interface plasmon or phonon polaritons of a negative permittivity slab [83, 84]. However, the structure of the modes in our system is markedly different from that of slab-guided polaritons. Guided modes of Fig. 4.5(b) are essentially bulk states and, as such, their dispersion characteristics do not depend on the thicknesses of individual layers.

Frequency-dependent group velocity of a single slow mode [indicated by arrow in Fig. 4.5(b)] is plotted in Fig. 4.5(c). We obtain $v_g \lesssim 0.004c$ over a 1.1 THz frequency range. Such wide bandwidth suggests the possibility of using the proposed system as an optical buffer. Assuming operation around the point of zero second-order dispersion and restricting group velocity deviation from that point to less than 10% (shaded region in the figure), we obtain a usable data transmission bandwidth of 390 gigabits per second, with the required device length of 14.4 μm for a 4-bit buffer. These parameters are comparable to operational characteristics of most currently proposed solid state slow light devices, in particular, those based on electromagnetically induced transparency and coupled resonator systems [85]. The combination of large data bandwidth and compact device size exhibited by our system is similar to that of the recently proposed plasmonic slow light waveguides [83]. Like the plasmonic devices, our system is strongly limited by losses ($\sim$ 4 dB/μm). It should be noted that our device exhibits somewhat lower losses while attaining slower group velocities than the plasmonic slow light structures [83].

4.3.3 Slow light in TE modes using μ anisotropy

Up to this point, the discussion of hyperbolic metamaterials was restricted to non-magnetic systems with strong natural or artificially induced anisotropy of the dielectric tensor. The motivation for this is the fact that homogenization theory of dielectrics has been extensively studied, and that the effective medium approximation for dielectrics often offers a straightforward way to capture the key physics of a HMM system. All features of hyperbolic materials, however, could be implemented with an appropriate anisotropy of the magnetic permeability. Furthermore, there exist material systems where such magnetic anisotropy is easier to attain than the dielectric anisotropy. Although we will not go into details here, it is trivial to recast the results derived above into a form appropriate for magnetic systems. It is easy to

see that just like only the TM modes of planar waveguides are affected by dielectric anisotropy, uniaxial *magnetic* anisotropy is "felt" by the TE modes only. From the symmetry of Maxwell's equations we can conclude that for homogeneous media, TM mode solutions for the $\boldsymbol{H}$ field take the same form as the TE mode solutions for the $\boldsymbol{E}$ field, provided the $\boldsymbol{\epsilon}$ and the $\boldsymbol{\mu}$ tensors are interchanged. Such solutions are important for certain metamaterial designs (e.g. "fishnet" structures [86]), where in-plane and out-of-plane magnetic response strongly differ.

4.3.4 Slow light in hyperbolic bilayers

The previous sections described the emergence of slow group velocity modes in waveguides where the energy flux in the core and the cladding have opposite signs. In the ray optics picture, the slow group velocities could also be explained by a negative Goos-Hänchen shift as the guided rays undergo total internal reflection at the core-cladding interface. The fields in the cladding – responsible for the "positive" energy flux – are simple decaying exponentials. It is natural to ask whether better control over slow light behavior could be achieved with a more sophisticated waveguide structure, which can afford greater variety in the functional form of the positive energy flux fields.

Recalling an earlier discussion of propagation criteria in HMM waveguides, we can observe that both $\epsilon_x > 0,\ \epsilon_z < 0$ and $\epsilon_x < 0,\ \epsilon_z > 0$ scenarios lead, in the idealized case, to modes with an arbitrarily high value of propagation constant β, but with different signs of group velocity. We can conjecture that by constructing a waveguide out of two layers, each corresponding to a different type of hyperbolic material [87], one might achieve low energy velocity modes, with properties different from those in simple HMM waveguides considered in previous sections. To demonstrated this, we will write down the expressions for modes in such hyperbolic bilayers and study the associated dispersion relations.

The procedure for determining modes in the case of dielectric boundary conditions is straightforward, if tedious. We have three interfaces; the unknowns are the five coefficients of the field Ansatz, as well as κ, k_{z1}, and k_{z2}. Using the boundary conditions for the $E_\parallel$ and $D_\perp$ fields, all the coefficients can be determined in terms of system geometry and material parameters; the boundary condition equations can then be combined into one:

$$k_{z1}\epsilon_{x1}\left[\tan\left(d_2 k_{z2}\right)\left(\kappa^2\epsilon_{x2}^2 - k_{z2}^2\right) + 2\kappa k_{z2}\epsilon_{x2}\right] - \\ - \tan\left(d_1 k_{z1}\right)\left[\kappa\tan\left(d_2 k_{z2}\right)\left(k_{z2}^2\epsilon_{x1}^2 + k_{z1}^2\epsilon_{x2}^2\right) + k_{z2}\epsilon_{x2}\left(k_{z1}^2 - \kappa^2\epsilon_{x1}^2\right)\right] = 0, \quad (16)$$

where we assumed that the medium on the boundaries of the bilayer is vacuum ($\epsilon = 1$). Together with the standard dispersion relations,

$$\frac{k_x^2}{\epsilon_{z1}} + \frac{k_{z1}^2}{\epsilon_{x1}} = \frac{\omega^2}{c^2} \quad (17a)$$

$$\frac{k_x^2}{\epsilon_{z2}} + \frac{k_{z2}^2}{\epsilon_{x2}} = \frac{\omega^2}{c^2} \quad (17b)$$

$$k_x^2 - \kappa^2 = \frac{\omega^2}{c^2}, \quad (17c)$$

Eq. (16) yields an implicit solution for the mode dispersion curves $\omega(k_x)$. These solutions must be studied numerically.

Note that the solutions of single-layer hyperbolic waveguides studied in the previous section are special cases of a two-layer system with one of the thicknesses set to zero. Accordingly, it is interesting to study the bilayer dispersion curves for a fixed device thickness d, as the ratio of individual layer thicknesses d_1 and d_2 interpolates between these two limiting cases. In Fig. 4.6 we plot the numerical solutions of Eq. (17) as the $d_1 : d_2$ ratio is varied between 1:9 and 9:1. We see that the waveguide modes indeed interpolate between the limiting behaviors previously seen in Fig. 4.3. The manner in which this evolution happens is rather interesting. Regardless of

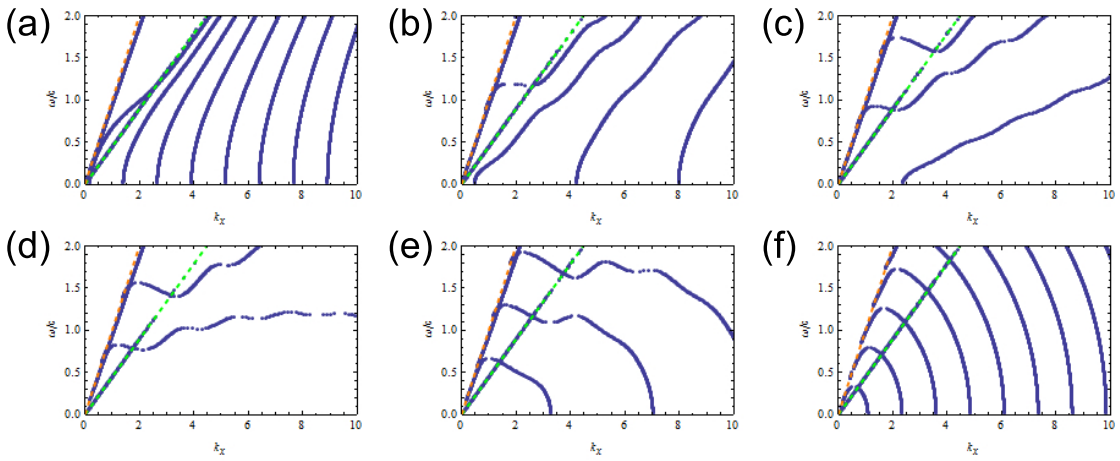

Figure 4.6: Dispersion curves for a hyperbolic bilayer waveguide ($\{\epsilon_{\parallel}^{(1)}, \epsilon_{\perp}^{(1)}\} = \{5, -5\}$, $\{\epsilon_{\parallel}^{(2)}, \epsilon_{\perp}^{(2)}\} = \{-5, 5\}$) with dielectric boundary conditions as layer thickness ratio is varied from 1:9 to 9:1

whether we start with the limit $d = d_1$ or $d = d_2$, as d_1 (or d_2) decreases due to the presence of another layer, the spacing between the waveguide modes grows – just as it would if we were to reduce the thickness of a single-layer device. The mode curves, however, start to become distorted. We can visualize what happens by imagining taking the two limiting cases, with the $\omega(k)$ curves given by Fig. 4.3 (a) and (b) [or by Fig. 4.6 (a) and (f)], and imagining weakly coupling those two waveguides. We expect the mode structure to start developing avoided crossings. Because for each branch in the dispersion relation, many avoided crossings arise, the resultant curve has many inflection points, as well as maxima and minima. For an appropriate device thickness, these extrema correspond to the slow light points, $\partial\omega/\partial k = 0$. We have created a situation where in a small frequency range, many slow light modes can exist simultaneously. Indeed, since a slow light mode can emerge at every avoided crossing point, and since the number of these points is, ideally, infinite, this implies that an infinite number of zero group velocity points exists in our bilayers! This stands in contrast to the "ordinary" slow light waveguide considered before, where for high enough frequencies, due to increased light confinement within the core, the

core-cladding flux balance condition could no longer be achieved, limiting the slow group velocity behavior to only a handful of modes.

The analysis of modal structure that we have performed allowed us to understand the properties of guided waves in hyperbolic nanophotonic structures. We can now use this insight to study the interactions of these structures with external fields. In particular, we can treat the problem of transmission and reflection through planar structures and discuss their potential imaging applications.

4.4 Hyperbolic slabs and imaging

Transmission and reflection characteristics are central to the studies of all optical devices and materials, and we have already discussed certain features of light transmission through hyperbolic metamaterials in both half-infinite and planar slab configurations. In particular, we demonstrated the negative refraction of the Poynting vector at an HMM interface. We also used the Fresnel reflection coefficient for a slab to explore the effects of coupling to waveguide modes on the radiative decay rates. In this section, we would like to elaborate on certain aspects of light transmission through hyperbolic slabs and their potential for super-resolution imaging.

The transmission function of a slab (or, indeed, any planar structure) can be easily computed using the transfer matrix approach (see Appendix C). For a single-layer anisotropic system, the result (for TM modes) is

$$\begin{aligned} T(k_x) &= \frac{2e^{2ihk_{z0}}\csc\left(dk_{z1}\right)}{2\cot\left(dk_{z1}\right) - \frac{ik_{z0}\epsilon_{\parallel}}{\epsilon_0 k_{z1}} - \frac{i\epsilon_0 k_{z1}}{k_{z0}\epsilon_{\parallel}}} \\ k_{z0} &= \sqrt{\frac{\omega^2}{c^2} - k_x^2} \\ k_{z1} &= \sqrt{\frac{\epsilon_{\parallel}}{\epsilon_{\perp}}\left(\mu_1\epsilon_{\perp}\frac{\omega^2}{c^2} - k_x^2\right)}. \end{aligned} \tag{18}$$

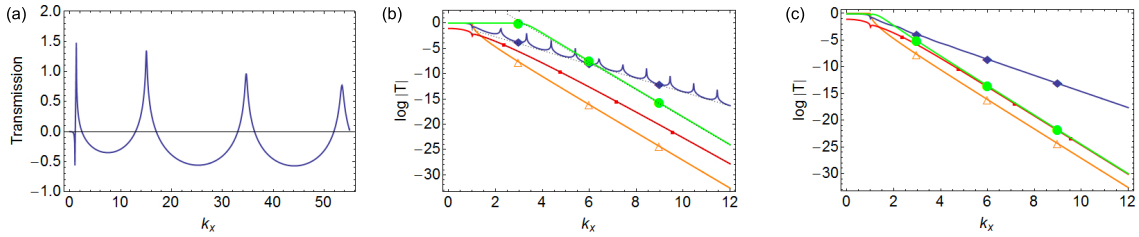

Figure 4.7: (a) Typical field transfer function of a hyperbolic slab. (b,c) Comparison of field transfer functions for impedance-matched slabs of thickness $\lambda/2$ with losses given by $\epsilon'' = 10^{-4}$ (panel b) and $\epsilon'' = 0.1$ (panel c). The input and output planes are located at $h = d/2$ (traditional superlens arrangement). Lines correspond to different metamaterial types. Green/circles: Pendry's superlens ($\epsilon' = \mu = -1$); red/squares: "poor man's superlens" ($\epsilon' = -1$, $\mu = 1$); blue/diamonds: hyperbolic slab ($\epsilon'_\perp = -1$, $\epsilon'_\parallel = 1$); orange/triangles: free space ($\epsilon = \mu = 1$, no losses).

Because this equation maps spatial frequencies k_x from the input to the output plane, we also refer to it as the transfer function. We assume that the fields originate at a distance h in front of the slab (measured from the front surface), and are detected the same distance h behind the slab (this accounts for the $e^{2ihk_{z0}}$ factor in the numerator).

The special case of Eq. (18) with $\epsilon_\parallel = \epsilon_\perp = \mu_1 = -1$ is the famous superlens transfer function. For $h = d/2$ we get $T = 1$ for every value of k_x. This picture changes dramatically if we introduce loss into the system. In particular, if the dielectric function is taken to be $\epsilon_1 = -1 + i\delta\epsilon$, $|\delta\epsilon| \ll 1$, $T(k_x)$ experiences exponential roll-off past the location of the pole:

$$k_x^{\max} \approx \frac{1}{2d}(1 - 2\log|\delta\epsilon|). \tag{19}$$

In the ideal lossless case, this pole moves to infinity, and the transfer function remains constant everywhere.

For a hyperbolic material, the denominator of Eq. (18) features an infinite number of poles, which correspond to coupling with the propagating modes inside the slab. For low losses, the behavior of the transfer function is dominated by these peaks [Fig. 4.7(a)].

It is interesting to compare the high-k_x behavior of transfer functions for the ideal superlens, "poor man's" superlens, and a hyperbolic slab with similar material parameters and the same amount of losses. We perform this comparison in Fig. 4.7(b) and (c), with the general form of the dielectric function given by $\epsilon = \pm 1 + i\,\epsilon''$. Losses were fixed at $\epsilon'' = 10^{-4}$ (panel b) and $\epsilon'' = 0.1$ (panel c). Examination of these curves reveals that in all cases, the dominant behavior of the transfer function is due to free-space decay of evanescent waves. In the case of the superlens, for small enough losses, resonant plasmonic excitations exactly compensate for that decay. However, past the cut-off value for k_x given by Eq. (19), it becomes impossible to couple to the plasmon resonances, and the exponential fall-off of the signal once again dominates.

In the case of "poor man's" superlens (i.e. a metallic slab with no magnetic response), the induced plasmon oscillations are not enough to fully compensate for the free-space decay. Whereas in the ideal superlens, the degenerate resonant plasmons induce exponential enhancement of the field (which makes such compensation possible), to leading order, in the "poor man's" superlens this enhancement obeys a power law: $T(k_x) \propto \exp(-2dk_x)k_x^4$, where $\exp(-2dk_x)$ is the usual free-space decay. This is enough to make it perform noticeably better than vacuum, as experiments have shown [61, 88], but approaching the performance of an ideal superlens is not feasible.

Hyperbolic slabs stand out in these plots rather favorably, since their transfer functions diminish half as fast with increasing k_x. The reason for this is simple: in the traditional superlens arrangement, exactly half of the space between input and output planes is filled with the metamaterial. In hyperbolic slabs, high-k_x waves propagate (with attenuation governed by material absorption). This effectively halves the distance over which the evanescent waves decay.

The second feature of the hyperbolic transfer function is the presence of multiple poles. As often happens in scattering theory, we can relate these poles to internal bound states of the system: in this case, it's the waveguide modes. A convincing

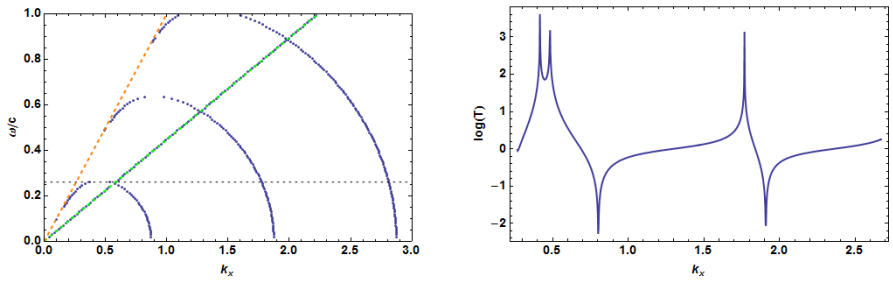

Figure 4.8: Transfer function resonances in the vicinity of the slow light mode for a single-layer waveguide

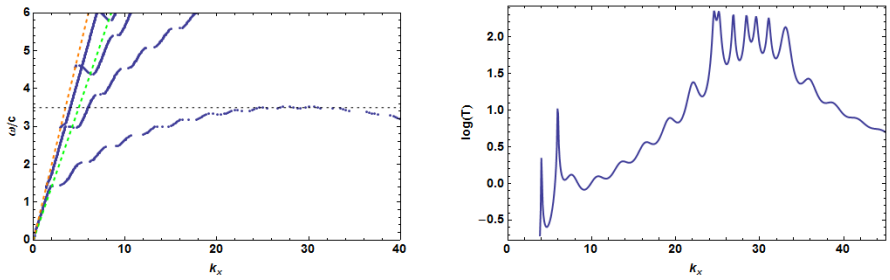

Figure 4.9: An ensemble of slow-light resonances in a bilayer waveguide

illustration of this is shown in Fig. 4.8 and Fig. 4.9, where we compute transmission function of a single and double-layer slow light waveguide of thickness $\lambda/2$. We fix the operating frequency as indicated by the dashed horizontal lines in the figures, and plot the transmission. Indeed, we see that for values of k_x where the waveguide dispersion relation indicates the presence of a mode, a transmission peak occurs. It is particularly interesting to examine the case of a slow light bilayer waveguide, in which for a fixed frequency, multiple slow light points exist. Looking at the transfer function, it is apparent that multiple slow light modes excite many closely-spaced transmission resonances. Because the resultant effective width of the resonance in k_x space far exceeds the width associated with "regular" hyperbolic transmission poles, which may further improve imaging performance of hyperbolic slabs.[1]

[1]We should note that the case of a perfectly impedance matched bilayer was treated in Ref. [87], where such an arrangement was found to *suppress* the transfer function poles. The bilayer waveguide regime evolution plots in Fig. 4.6 can hint at the mechanism behind this: under the right conditions, the first intersection of a waveguide mode and a line $\omega = \text{const}$ can occur at an arbitrarily high value of k_x.

4.5 Conclusion

We have seen earlier, by considering a single interface, that the $\{\epsilon_\perp < 0,\ \epsilon_\parallel > 0\}$ materials enable all-angle negative refraction for incident plane waves. However, for *guided modes*, this form of the dielectric tensor results in negative phase velocities and even negative group delays – phenomena that used to be primarily associated with magnetic ($\epsilon_x < 0,\ \mu < 0$) negative index materials [89].

We have demonstrated that a planar anisotropic waveguide with negative transverse permittivity supports slow light modes. Such modes are made possible by the balance of positive energy flux in the cladding and negative energy flux in the core.

Recognizing that a planar lens is simply a waveguide turned on its side, we proceeded to study the transfer functions of hyperbolic slabs, comparing it to the thoroughly studied problem of Pendry's superlens, both in its ideal variant, as well as in the form of the non-magnetic "poor man's" superlens. We found that the propagating nature of waves in HMMs means that the optical path length over which those waves decay is less, and in that sense they may be considered superior to the other planar lenses considered. Further performance enhancement for imaging may be found by exploiting the resonant coupling to the slow light modes in a single layer or bilayer configuration.

All these devices and methods merely help amplify or guide evanescent waves; as soon as they enter free space, they once again suffer from exponential decay. Yet we have seen in Chapter 3 that it is possible to convert evanescent waves into propagating ones; the hyperlens accomplishes this, effectively, by means of geometrical magnification. In the following chapter we will describe an alternative way to retrieve information from evanescent waves by scattering them into the far field. Although we will not be utilizing hyperbolic dispersion relation, our discussion will be informed by insights into subwavelength imaging, scattering, and anisotropic nanostructures obtained in the earlier chapters.

Chapter 5

Subwavelength resolution: alternative approaches

5.1 Introduction

In previous chapters we examined the applications of metamaterials in the areas of imaging, wave guiding, and radiative decay engineering. Many novel properties described above, as well as by other researchers, derive their existence from specific resonances enabled by the particular combinations of material parameters and device geometry. For example, we have explored the coupling of radiation to plasmons, slow light modes, and cut-off free whispering gallery modes. The fruitfulness of studying resonances is, perhaps, obvious given their central importance in all systems governed by the wave equation.

In this chapter, we will focus on a different set of tools, of equally profound importance in studying wave phenomena: the scattering of waves. In particular, we will explore scattering as a means of broadening the accessible spatial frequency spectrum beyond the usual diffraction cutoff. Our approach can be motivated, in part, by observing that "classical" optical elements that manipulate the spatial frequencies

may be broadly classified into refractive and diffractive devices [43]. In many cases, both of these device classes can be utilized for similar purposes – for instance, prisms and gratings both perform spectral decomposition, thin lenses and Fresnel lenses are both used for focusing, and mirrors and Bragg reflectors both redirect light. In a similar vein, we might ask whether some operational features of the hyperlens or the superlens – both of which can be traced to classical refractive devices – can be implemented in the context of diffractive optics.

As our departure point, we will recall the eigenmode representation of the hyperlens described in Section 3.2. High-order hyperlens modes effectively couple high spatial frequency field variations on the inner surface of the device to lower spatial frequency waves on the outer surface. Indeed, this is conceptually similar to the manner in which a conventional magnifying lens operates. The striking difference, however, comes from the fact that modes of an ideal hyperlens do not suffer from diffraction-induced cut-offs, enabling the high order modes to become extra information channels that can be used for probing subwavelength structure. It is natural to ask what other methods might exist for converting high spatial frequencies to lower ones, and diffraction provides one natural answer.

It is well known from Fourier optics that fields passing through an idealized grating with periodicity d have their spatial frequencies shifted by a multiple of the grating vector $q = 2\pi/d$:

$$k_x' = k_x + jq, \qquad \text{j=...,-1,0,1,...,}$$

where k_x' and k_x are the transmitted and incident transverse wave vector components. It is important to note that this formula is valid for both evanescent and propagating waves. This implies that if the grating is placed in the near field of some object, then for a sufficiently large value of q, the evanescent components of the object's spatial spectrum ($|k_x| > \omega/c$) can be scattered into the propagating waves with $|k_x'| = |k_x - q| < \omega/c$. These fields can then be studied using conventional optics.

This basic idea was proposed and subsequently demonstrated by Durant et al., who called their approach the *far field superlens* (FSL) [90]. Although these experiments were an important proof-of-principle step, they also uncovered several deficiencies inherent in the simple strategy described above that the FSL fails to overcome. First, the FSL essentially presents a grating etched in a plasmonic near-field superlens of the sort described in Section C.2. As such, it is a strongly dispersive and lossy device. More importantly, however, from the relation $|k'_x| = |k_x - jq|$ (where j is the diffraction order), it is obvious that there will always be transmitted spatial frequencies that result from an overlap of two or more diffraction orders – consider, for instance, the case $k_x = 0, j = 0;\ k_x = q, j = 1;\ k_x = -q, j = -1$. Here, three distinct spatial frequencies contribute to the signal at $k'_x = 0$. In addition, the spatial frequency spectrum is merely *shifted*, it is not compressed; the amount of the shift is fixed for each manufactured grating. This means that if, for instance, the effective passband of the original optical system is the usual $[0, 2\pi/\lambda]$, and the spectrum were to be shifted by $2q = 4\pi/\lambda$, then the effective passband becomes $[2\pi/\lambda, 6\pi/\lambda]$. The $3\times$ improvement in resolution comes, at best, at the expense of losing information about features larger than $\lambda/2\pi$. In practice, the passband must be made even smaller in order to minimize the effects from interference of the multiple diffraction orders, even in an idealized system.

This comes in sharp contrast with the characteristics of the hyperlens. Whereas the latter opens up new information channels that can carry subwavelength information, the FSL must discard a portion of the original spectrum.

In the next section, we will describe an alternative approach to far-field imaging and spectroscopy of subwavelength structures, based on a device that converts mid-IR evanescent waves to propagating waves via scattering on acoustic phonons. These scattered and frequency-shifted waves can be easily decoupled from the existing propagating spectrum that forms the regular diffraction-limited image, and with

minimal processing can be used to distinguish subwavelength features. Furthermore, the ability to dynamically tune the period of the acoustic grating makes this system more robust and flexible compared to the FSL approach.

In further sections, it will be shown that the idea of acoustic modulation and the associated frequency shifts goes far beyond fixing operational deficiencies of the FSL and, indeed, provides a rich playground for subwavelength imaging, detection, and fingerprinting in the optical spatial frequency domain. We will describe a device that can perform subwavelength holographic imaging, as well as a hybrid device that borrows ideas from both the fixed-grating approach, as well as the phonon scattering approach, and can be used for subwavelength fingerprinting.

5.2 Super-resolution via scattering on phonons

5.2.1 Motivation

The first system we will describe arose out of a desire to construct a super-resolution system that operates in the mid- to far-IR, as well as terahertz parts of the spectrum. Such a system would present a solution to an important technological problem and open new possibilities in imaging, spectroscopy, and detection. Indeed, while the mid-IR and THz spectral bands are extremely important in chemical analysis [91, 92], the usual $\lambda/2$ diffraction limit severely constrains the spatial resolution of any IR or THz imaging setup. In particular, the scale of the smallest resolved features in biological samples is comparable to the size of cells (5-30 μm). To perform imaging of sub-cellular chemistry and other nanoscale processes in the IR, super-resolution is required. Moreover, it should be emphasized that the potential impact of such super-resolution systems goes far beyond simple imaging applications. For example, in cellular biology, relative localization or relative distribution of organelles can reveal important information about cellular processes. As a result, much of the current

super-resolution research focuses not on "super-imaging," but on the various optical and statistical techniques to precisely locate fluorescent markers attached to structures of interest [93]. We can see, therefore, that detection of high spatial frequencies is a fundamentally important problem in its own right, with imaging being just one of its applications.

To construct a super-resolution system in mid-IR, we start with a diffraction grating approach, outlined in the previous section. In order to shift high spatial frequency components into the propagating part of the spatial spectrum, the grating vector q must be commensurate in magnitude with the spatial frequencies we wish to study. More precisely,

$$q \geq k_x - \omega/c. \tag{5.1}$$

For example, to double the resolution relative to the diffraction limit, one must pick $q \approx \omega/c$. For mid-IR, this means that the grating period should be of the order of a few microns. It is easy to see that this distance closely matches the wavelength of high-frequency ultrasound phonons. Indeed, assuming sound propagation velocity $v \sim 5000$ m/s and ultrasound frequency $f \sim 500$ MHz, we have $\lambda_{\text{phonon}} = v/f \sim 10$ μm.

Acoustic gratings have several significant advantages over microfabricated ones. First, the gratings are easily tunable, which leads to a great deal of flexibility in the experimental design. For example, the system may be optimized for studying a particular range of spatial frequencies by tuning the grating through a particular range of acoustic frequencies. Second, the diffracted waves are shifted by the acoustic frequency due to the energy and momentum conservation of phonon-photon scattering. This means that the high spatial frequencies shifted into the propagation band by scattering are *spectrally separated* from the existing propagating waves. These properties of acoustic gratings solve some of the major problems we identified with the nanofabricated far-field superlens: the interference between diffraction orders and a

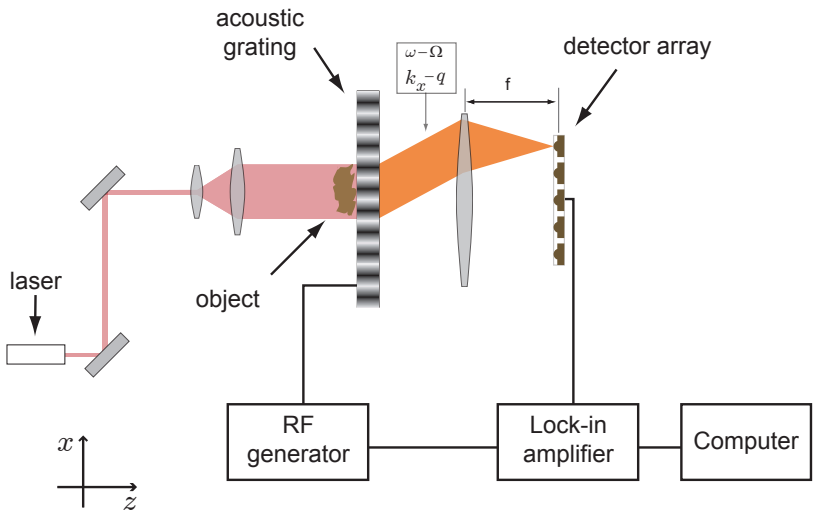

Figure 5.1: Schematics of the proposed super-resolution Fourier spectroscope

limited spatial frequency passband, fixed by the grating period. The phonon grating, in addition, requires no nanofabrication; the device would draw on decades of research in acousto-optic materials.

5.2.2 Proposed setup

The proposed super-resolution Fourier sensing system is shown in Fig. 5.1. The object, placed in the near field of an acousto-optic modulator (AOM), is illuminated by a plane wave from a mid-IR or THz source. The object scatters the illumination into waves with various transverse wave vector components k_x. These waves immediately enter the acousto-optic medium, where a phonon grating is set up by a running acoustic wave at frequency Ω. Due to scattering on the acoustic waves, the transverse wave vector k_x of the incident radiation is shifted by integer multiples of q, while its corresponding frequency is shifted by integer multiples of Ω. This implies that for a sufficiently large q, the evanescent components of the object's spatial spectrum ($|k_x| > \omega/c$) can be scattered into the propagating waves with $|k_x'| = |k_x - q| < \omega/c$. As discussed above, these waves will be shifted in frequency by the acoustic frequency Ω. The amplitudes and phases of these waves still carry the same information about

the fine spatial structure of the object as the original evanescent fields. Upon reaching the far field detector, the scattered waves will interfere with the illuminating radiation, producing a beat note photocurrent of frequency Ω, which can be retrieved using a fast lock-in amplifier. The high spatial frequency information therefore can be uniquely recovered in the far field without interfering with the existing propagating spectrum. Assuming $q \gtrsim \omega/c$, we have $\Omega \gtrsim v\omega/c = 2\pi v/\lambda$, where v is the sound velocity in the acoustic medium, and λ is the wavelength of illuminating radiation. With the typical sound velocity in solids of 5.5×10^3 m/s, the required acoustic frequency for λ=10 μm is $\Omega \gtrsim 550$ MHz, which is within the range of fast RF transducers. For terahertz wavelengths, the needed acoustic frequency is correspondingly lower.

5.2.3 Mathematical description

We model our system as a dielectric slab with surface normal in the z direction. We further assume that the back facet of the slab has been treated to minimize multiple reflections inside the slab, which we neglect in our calculations. The object under study is immediately adjacent to the slab and is illuminated with a plane wave $E_0 e^{i(\boldsymbol{k}\cdot\boldsymbol{r}-\omega t)} = E_0 e^{i(k_0 z-\omega t)}$. Planar acoustic wavefronts propagate along the x direction throughout the bulk of the slab. Due to the photoelastic effect [94], this results in a sinusoidal modulation of the dielectric permittivity:

$$\epsilon(x) = \overline{\epsilon} + \Delta\epsilon \cos(qx - \Omega t), \tag{5.2}$$

which corresponds to a weak spatiotemporal volume grating.

We may write the general form of the field inside the grating as a sum over the discrete diffracted orders:

$$E = \sum_j A_j(z) \exp[i(k_x + jq)x - i(\omega + j\Omega)t]. \tag{5.3}$$

Plugging this Ansatz into the usual source-free wave equation, we obtain a simple recursion relation between the various scattered components of a particular k_x mode:

$$A_j''(z) + k_{z_j}^2 A_j(z) = -\frac{\Delta\epsilon}{2c^2}\omega_j^2[A_{j-1}(z) + A_{j+1}(z)], \tag{5.4}$$

where $k_{z_j} = \left[\bar{\epsilon}\frac{\omega^2}{c^2} - (k_x + jq)^2\right]^{1/2}$, and $\omega_j \simeq \omega$.

The amplitude of the jth diffracted order, A_j, is proportional to $(\Delta\epsilon)^j$, with $\Delta\epsilon/\epsilon \ll 1$, allowing to ignore higher order terms ($j \geq 2$). We can, furthermore, conclude that the amount of energy scattered into the shifted waves is small, thereby permitting to neglect the variation of 0th diffracted order A_0 (the undepleted pump approximation). We note that for propagating waves, this conclusion is valid insofar as there exists no Bragg matching between the incident and diffracted waves. Since the phonon wave vector q is a tunable parameter in our model, it is always possible to pick a range of q values to ensure minimal energy loss in the incident wave. For the evanescent waves, the undepleted pump approximation is justified by the small interaction length.

Keeping terms up to first order in Eq. (5.3), we see that a plane wave with transverse wave vector k_x inside the slab acquires "sidebands" with spatial frequencies $k_x^{\pm} = k_x \pm q$:

$$E = A_0\exp[i(k_x x - \omega t)] + A_+(k_x)\exp[i(k_x^+ x - (\omega+\Omega)t)] + A_-(k_x)\exp[i(k_x^- x - (\omega-\Omega)t)]. \tag{5.5}$$

We can now relate the spatial frequency spectrum entering the slab ($E_{\text{in}}(k_x)$) to the spectrum at the output:

$$E_{\text{out}}(k_x) = \left[\tilde{A}_-\exp(i\Omega t) + \tilde{A}_+\exp(-i\Omega t) + \tilde{A}_0\right]\exp[i(k_x x - \omega t)], \tag{5.6}$$

where we define $\tilde{A}_{\pm} = A_{\pm}(k_x \mp q) = t^{\pm}E_{\text{in}}(k_x \mp q)$; $\tilde{A}_0 = t_0 A_0$. Here, t_0 is a transmission coefficient, while $t^{\pm}$ capture both generation of phonon-scattered waves as well as the transmission characteristics of the dielectric structure:

$$t_0 = \frac{2\sqrt{\epsilon}\sqrt{(\omega/c)^2 - k_x^2}}{\epsilon\sqrt{(\omega/c)^2 - k_x^2} + \sqrt{\epsilon(\omega/c)^2 - k_x^2}}; \tag{5.7}$$

$$t^{\pm} = t_0 \frac{\Delta\epsilon}{2}\left(\frac{\omega}{c}\right)^2 \frac{1}{q(q \mp 2k_x)} \frac{\epsilon\sqrt{(\omega/c)^2 - k_x^2} + \sqrt{\epsilon(\omega/c)^2 - (k_x \mp q)^2}}{\epsilon\sqrt{(\omega/c)^2 - k_x^2} + \sqrt{\epsilon(\omega/c)^2 - k_x^2}.} \tag{5.8}$$

We note that for $q \approx 0$, as well as $q \approx \pm 2k_x$, the perturbative treatment of Eq. (5.4) breaks down. As we shall see below, these regions also correspond to poor noise performance of this system, and thus are to be avoided in experimental setting.

For most choices of q, however, the output spectral component with spatial frequency k_x can be related to the input components with spatial frequencies $k_x' \equiv k_x \pm q$. For values of q such that $|k_x'| > \omega/c$, the input spectrum corresponds to subwavelength spatial features, which cannot be retrieved using ordinary methods.

Equations (5.6), (5.7) and (5.8) explicitly demonstrate that the high spatial frequencies propagate to the far field, and are spectrally separated from the existing signal in the "ordinary" optical passband. However, we can also see that the effective transfer function for these components is somewhat complicated and, furthermore, that care must be taken to decouple "upshifted" and "downshifted" waves.

We now proceed to describe in greater detail the procedure for reconstructing the high spatial frequency components of the input spectrum. We will start by discussing a computational method to reconstruct the data, as well as its limitations. Further on, we show that much information can be derived from using signal "as is". In Section 5.2.7 we describe how an addition of another frequency-shifted optical signal can enable direct unambiguous reconstruction of both the amplitude and the phase of the incident field.

5.2.4 Reconstruction of the input spectrum via iterative computation

Light scattered by the acoustic grating is analyzed using a Fourier optics setup [the simplest such system being a lens with a photodetector array in its focal plane [43], as illustrated in Fig. (5.1)]. We assume that the system has unity numerical aperture, i.e. values of k_x in the range $[-\omega/c, \omega/c]$ are accessible. The photodetector cells obey the usual square law. The output of the detector array is thus proportional to the incident intensity at the given spatial frequencies. The object under study is illuminated by a plane wave $A_i e^{ik_0 z}$, which has the amplitude $\tilde{A}_i$ in the detector plane. There it interferes with waves $\tilde{A}_0$ scattered by the object and waves $\tilde{A}^{\pm}$ scattered by both the object and the acoustic grating. We note that $\tilde{A}_i \gg \tilde{A}_0 \gg \tilde{A}^{\pm}$. Using Eq. (5.6) and neglecting the higher order terms we thus obtain

$$\begin{aligned} I_{\text{out}}(k_x) &= \left| \left[E_i \exp(ik_0 z) + (\tilde{A}^- \exp(i\Omega t) + \tilde{A}^+ \exp(-i\Omega t) + \tilde{A}_0) \exp[i(k_x x + k_z z)] \right] \right|^2 \\ &= |\tilde{A}_i|^2 + \exp[i(k_0 z - k_z z - k_x x)] \left[(\tilde{A}_i \tilde{A}_+^*) \exp(i\Omega t) + (\tilde{A}_i \tilde{A_-}^*) \exp(-i\Omega t) \right] + \text{c.c.} \\ &= |\tilde{A}_i|^2 + |\tilde{A}_0|^2 + 2 \left[|\tilde{A}_i \tilde{A}_-|^2 + |\tilde{A}_i \tilde{A}_+|^2 + 2|\tilde{A}_i^2 \tilde{A}_+ \tilde{A}^-| \cos[\phi(x,z)] \right]^{1/2} \cos(\Omega t + \gamma), \end{aligned} \tag{5.9}$$

where $\phi(x,z) = (k_0 - k_z)z - k_x x$. The $\cos[\phi(x,z)]$ term vanishes when integrated over the finite aperture of the detector. Subtracting the illumination background $\tilde{A}_i$ from our measurements, we are left with the following signal:

$$I_{\text{out}} = |\tilde{A}_0|^2 + 2 \left(|\tilde{A}_i \tilde{A}_-|^2 + |\tilde{A}_i \tilde{A}_+|^2 \right)^{1/2} \cos(\Omega t + \gamma). \tag{5.10}$$

The two terms in this equation can be decoupled using standard techniques: the DC term is isolated with the aid of a low-pass filter, while the term oscillating at the acoustic frequency Ω is recoverable using lock-in detection. For any given k_x,

this second term contains contributions from both $\tilde{A}_+ = t^+ E_{\text{in}}(k_x - q)$ and $\tilde{A}_- = t^- E_{\text{in}}(k_x + q)$. Nevertheless, for a range of k_x values it is possible to recover the magnitude of just the high spatial frequency components of the input field, $|E_{\text{in}}(k_x + q)|$.

In particular, the DC measurement yields $|\tilde{A}_0| = |t_0 E_{\text{in}}(k'_x)|$ for $k'_x \in [-\omega/c, \omega/c]$, making it possible to deduce $|E_{\text{in}}(k_x - q)|$ (as long as $|q| \leq \omega/c + |k_x|$). This allows to determine $|\tilde{A}_+|$. The magnitude of illumination background $|\tilde{A}_i|$ can also be obtained from the DC measurement. It then becomes possible to use Eq. (5.10) to compute $|\tilde{A}_-|$ and, thereby, $|E_{\text{in}}(k_x + q)|$:

$$|E_{\text{in}}(k_x + q)| = \sqrt{\frac{\left(|\tilde{A}_i \tilde{A}_-|^2 + |\tilde{A}_i \tilde{A}_+|^2\right) - |\tilde{A}_i \tilde{A}_0|^2 |t^+/t_0|^2}{|\tilde{A}_0|^2 |t^-|^2}}. \tag{5.11}$$

Assuming that the detector (or a detector array) can be placed so that signal with $k_x \in [-\omega/c, \omega/c]$ can be measured and that q can vary from 0 to $2\omega/c$ by tuning the acoustic frequency we see that $|E_{\text{in}}(k_x)|$ can be determined for $k_x \in [-3\omega/c, 3\omega/c]$. This means that $|E_{\text{in}}(k_x - q)|$ is now known for $\omega/c + |k_x| \leq |q| \leq 3\omega/c + |k_x|$, in turn making it possible to compute $|E_{\text{in}}(k_x)|$ for $k_x \in [-5\omega/c, 5\omega/c]$. Note that in principle, this process can be continued iteratively, yielding $|E_{\text{in}}(k_x)|$ for $|k_x| \leq (1 + 2n)\omega/c$, $n = 1, 2, \ldots$ – i.e. an arbitrarily large value of k_x.

5.2.5 Limitations of the iterative computation method

In a realistic setting, the retrieval of high spatial frequency information will be limited at a certain stage by measurement errors. We proceed to examine the effects of these errors on the computed value of $|E_{\text{in}}(k_x)|$. To do so, we assume that the two measured terms in (5.10) contain a normally distributed error with variances $\tilde{\sigma}_0^2$ and $\tilde{\sigma}_\Omega^2$ for the DC and the acoustic term respectively. We fix these measurement error levels by

specifying an overall signal-to-noise ratio. We then have

$$\sigma = \frac{\overline{\text{signal}}}{\text{SNR}},$$

where

$$\overline{\text{signal}} = \begin{cases} \frac{1}{2\omega/c}\int_{-\omega/c}^{\omega/c} |\tilde{A}_0|^2 dk_x, & \sigma = \tilde{\sigma}_0 \\ \frac{1}{2\omega/c}\int_{-\omega/c}^{\omega/c} \frac{1}{1+|k_x|}\int \left(|\tilde{A}_i\tilde{A}_-|^2 + |\tilde{A}_i\tilde{A}_+|^2\right)^{1/2} dq dk_x, & \sigma = \tilde{\sigma}_\Omega \end{cases} \tag{5.12}$$

As a result, the computed $|E_{\text{in}}(k_x+q)|$ term acquires the errors σ_0 and σ_Ω:

$$\begin{aligned} \sigma_0^2 &= \frac{1}{4}\left|\frac{t^+}{t^-}\right|^4 \frac{1}{|t_0|^4|E_{\text{in}}(k_x+q)|^2}\tilde{\sigma}_0^2 \\ \sigma_\Omega^2 &= \left(1+\left|\frac{t^+E_{\text{in}}(k_x-q)}{t^-E_{\text{in}}(k_x+q)}\right|^2\right)\frac{1}{|t^-|^2|\tilde{A}_i|^2}\tilde{\sigma}_\Omega^2. \end{aligned} \tag{5.13}$$

These expressions reveal that three factors determine the overall reconstruction error: this error becomes large when $t^+ \gg t^-$, when $|E_{\text{in}}(k_x+q)| \ll \overline{|E_{\text{in}}|}$, and/or when $|E_{\text{in}}(k_x+q)| \ll |E_{\text{in}}(k_x-q)|$. From Eq. (5.8) it is apparent that $|t^+/t^-| \gg 1$ when $q = 2k_x$. This corresponds to phasematching. As this regime is approached, the undepleted pump approximation ceases to be accurate. To minimize the effect of phasematching in the spectral region of interest, we must choose $k_x \approx \omega/c$ and $q < 2\omega/c$. The second error-determining factor, $\overline{|E_{\text{in}}|}/|E_{\text{in}}(k_x+q)| \ll 1$, reflects the fact that the system is most sensitive to spectral features whose power equals or exceeds the average spectral power of the object. In addition, the requirement $|E_{\text{in}}(k_x+q)/E_{\text{in}}(k_x-q)| \ll 1$ indicates that the spectral features at k_x+q must be stronger than those at k_x-q. Because both k_x and q are experimentally controlled variables, it is reasonable to assume that this requirement can be met for most spectral distributions of interest.

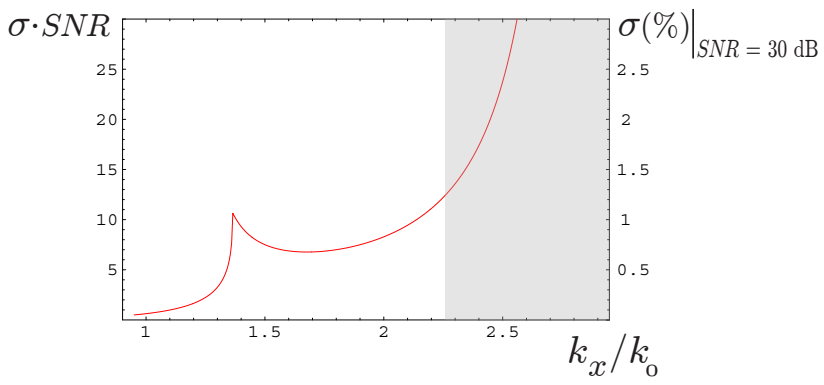

Figure 5.2: Accumulated fractional error in the reconstructed signal for measurement parameters $k_x = 1$, $0 < q < 2k_0 \equiv 2\omega/c$, $\epsilon = 2$. Error grows rapidly in the phasematching region (shaded gray).

In analyzing the error budget, it is useful to assume $|E_{\rm in}(k_x+q)| \approx |E_{\rm in}(k_x+q)| \approx \overline{|E_{\rm in}|}$ and that $k_x \approx \omega/c$. Furthermore, we assume that SNR is the same for both direct and acoustic measurements. In this case, the leading term in the overall fractional error is given by

$$\sigma = \frac{1}{2}\left|\frac{q+2\omega/c}{q-2\omega/c}\right|^2 \left|\frac{\epsilon\sqrt{2(\omega/c)(\omega/c-k_x)}+\sqrt{(\epsilon-1)\omega/c-q(q-2)}}{\epsilon\sqrt{2(\omega/c)(\omega/c-k_x)}+\sqrt{(\epsilon-1)\omega/c-q(q+2)}}\right|^2 \frac{1}{SNR}. \quad (5.14)$$

Using this expression, the overall reconstruction error can be simply related to the SNR of the detected signals. We show the behavior of the error in Fig. 5.2. We note that the error grows rapidly as the reconstructed spatial frequency approaches phasematching. In this region, recovering the signal becomes problematic. In order to discern the input spectrum, we must choose a combination of k_x and q in order to avoid the phasematching peak. It is possible to do so by picking a larger value of q. Recall that the maximum allowed value of q is determined by the knowledge of $|E_{\rm in}(k_x-q)|$, where k_x is the measured spatial frequency. The simple measurement of diffraction-limited spatial spectrum gave $|E_{\rm in}|$ for $k_x \sim (-\omega/c, \omega/c)$. Detection of the waves scattered from the acoustic grating expanded that range to the extent allowed by phasematching; in the example of Fig. 5.2 the recovered spectrum was increased

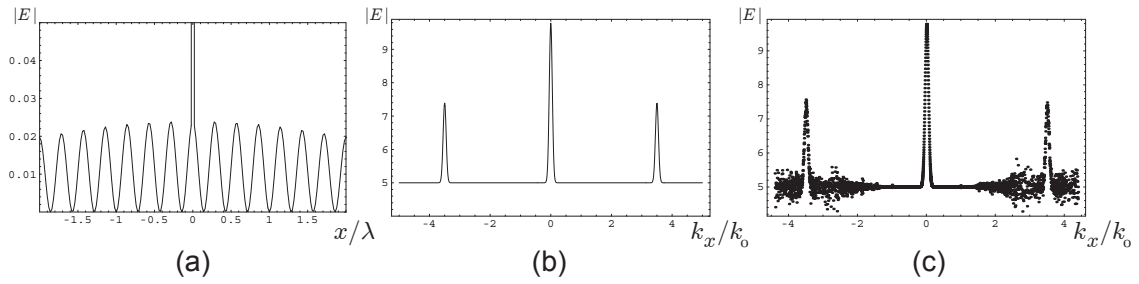

Figure 5.3: (a) Spatial dependence of the field (subwavelength diffraction grating with a point source) (b) Spectral distribution of the field. (c) Recovered spectral distribution (assuming 30 dB SNR)

to $k_x \sim 2.2(-\omega/c, \omega/c)$. Consequently, we can pick a combination of k_x and q to avoid the phasematching divergence. The only penalty associated with this approach is increased noise in the recovered signal (since a part of the noisy recovered signal serves as input). If the initial noise floor is sufficiently low, however, the recovery of many strong spatial spectrum features is possible.

In Fig. 5.3(a) we plot a sample field distribution featuring a subwavelength pattern (which includes both a subwavelength grating and a point source). It is clear from Fig. 5.3(b) that the main features of the spectrum are far above the diffraction limit cut-off. The input SNR is assumed to be 30 dB for both the DC and the lock-in signals. Reconstructed spectrum is show in Fig. 5.3(c). Although the presence of noise is evident, the main spectral features of the spatial distribution are well-preserved.

5.2.6 Differential detection

We have seen that it is possible to decouple the "upshifted" and "downshifted" signals and use the computed high spatial frequencies to generate a super-resolved image. We have also seen that due to the iterative nature of the procedure, the results may suffer from poor SNR in the wings of the spatial spectrum under non-ideal noise conditions. Before we go on to describe an alternative setup that will make it possible to avoid the problem of the coupling of diffraction orders, it is worth pointing out

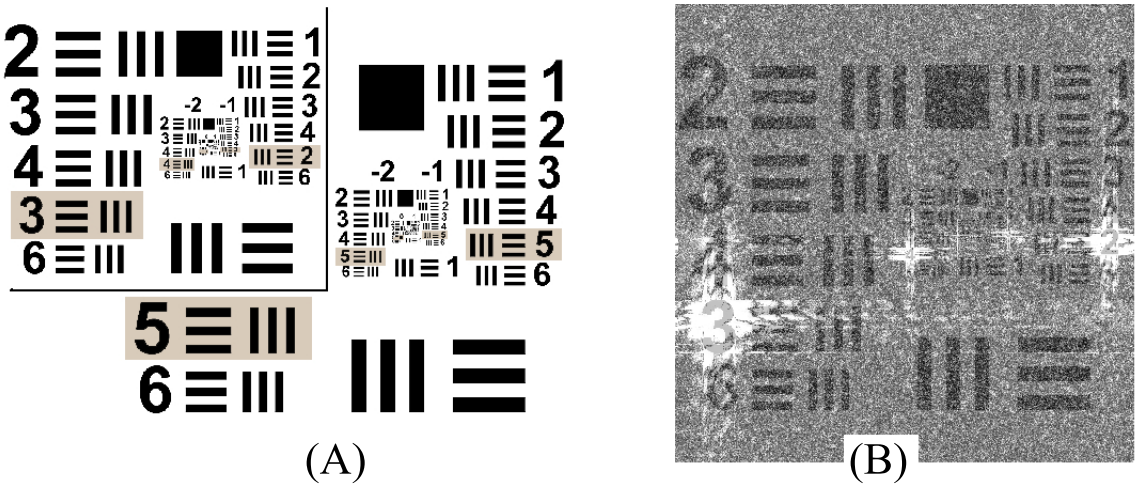

Figure 5.4: (a) Optical test target and its modified version (inset). In the modified target, the "5" label of every column has been replaced by another digit. (b) Computed output of the system in the presence of noise (shown in grayscale) assuming a realistic, noisy detector with 400 active photocells. The modified optical target is superimposed for illustration purposes. The output of the system clearly identifies the location of every modified digit, even for regions far below the diffraction limit.

that the simple system described above can, without further modifications and with good noise performance, be used in detecting subwavelength morphological changes between different samples.

To illustrate this, we utilize Eq. (5.10) to perform a comparison between the standard optical target of Fig. 5.4 and a modified target, where the label of every 6th line group has been randomly replaced. The first replacement corresponds to the last resolvable line group ($\lambda/2.5$ line separation); the subsequent replacements correspond to halving the size of the line groups ($\lambda/5,\ldots,\ \lambda/40$). We assume the measurement is performed by selecting an element of a photodetector array in the observation plane and using two orthogonal acoustic transducers to scan the acoustic wavevector within the range $q_{x,y} \in [-25\,\omega/c, 25\,\omega/c]$.

It should be emphasized that any method that relies on digital processing of raw data can suffer form rapid – sometimes exponential [22] – accumulation of noise. To address this potential issue, in our computations we add a normally-distributed random term to the AC amplitude of Eq. (5.10) in order to simulate noise in the system.

Because SNR is expected to be lowest for maximum values of the acoustic wavevector q, we consider SNR=10 for $q = 25\,\omega/c$ [1]. Assuming a practical 20×20 element photodetector array, we compute the signal given by Eq. (5.10) for the standard target, as well as the modified target [Fig. 5.4(a)]. Fig. 5.4(b) shows the result of subtracting the two datasets and performing an inverse Fourier transform, with the resulting plot superimposed onto the modified optical target. Evidently, every change in the original image is manifested in this difference diagram. Furthermore, it is largely localized in the vicinity of the actual changed pixels. It is possible to discern the difference signal even from the $\lambda/40$ line group label.

The ability to distinguish between fine spatial features of optical targets makes the system described above uniquely suited for identifying objects based on their subwavelength spatial features. As a result, it may find applications in fingerprinting and/or detection of chemical and biological structures.

5.2.7 Reconstruction of the input spectrum with a secondary optical signal

A straightforward modification of the setup just described not only allows to measure the "downshifted" $\tilde{A}_-$ component directly, but also provides a method for retrieving phase information, making it possible to perform phase-contrast microscopy, as well as 3D imaging on subwavelength scales.

To this end, a portion of the illuminating radiation is shifted in frequency by Ω_b using a second AOM. Unlike the modulator that interacts with light scattered from the sample in the Raman-Nath regime [94], this second AOM utilizes an appropriately oriented and longer cell to produce Bragg scattering. This results in a strong optical signal at frequency $\omega + \Omega_b$, $|\tilde{A}_b| \exp[i(k_b \cdot r - (\omega + \Omega_b)t)]$, which is projected onto the detector [see Fig. 5.5(a)]. Interference between the two optical signals produces beat

[1] Acoustooptic diffraction efficiency, and hence the signal-to-noise ratio varies as $1/q$.

note photocurrents with frequencies Ω, Ω_b, $\Omega_b + \Omega$, $\Omega_b - \Omega$:

$$
\begin{aligned}
I_{\text{out}}(k_x) &= \\
&= \left| E_i \exp(ik_0 z) + \tilde{A}_b \exp(i\boldsymbol{k}\cdot\boldsymbol{r}) + [\tilde{A}^- \exp(i\Omega t) + \tilde{A}^+ \exp(-i\Omega t) + \tilde{A}_0] \exp(i\boldsymbol{k}\cdot\boldsymbol{r}) \right|^2 \\
&= \ldots + 2|\tilde{A}^- \tilde{A}_b| \cos[(\Omega_b + \Omega)t + \Delta\Phi^-] + 2|\tilde{A}^+ \tilde{A}_b| \cos[(\Omega_b - \Omega)t + \Delta\Phi^+] + \ldots ,
\end{aligned}
\tag{5.15}
$$

where $\Delta\Phi^{\pm} = (k_b - k)\cdot r - \phi^{\pm}$ is the phase difference between the signal from the Bragg cell, $|\tilde{A}_b| \exp(ik_b \cdot r)$, and the Raman-Nath-scattered signal $\tilde{A}^{\pm} \exp(ik \cdot r) = |\tilde{A}^{\pm}| \exp[i(\phi^{\pm} + k \cdot r)]$.

Of special interest is the component at frequency $\Omega + \Omega_b$, which carries the high spatial frequency information contained in its modulus and its phase $\Delta\Phi^- \simeq (k_x^b - k_x)x - \phi^-$. Both of these quantities can be retrieved using lock-in techniques. To produce the lock-in reference, the RF signals driving the two acoustic cells can be mixed using a nonlinear element (e.g. a diode) and appropriately filtered to produce the sum frequency. As a result, complete information can be obtained about the complex high spatial frequency Fourier component $\tilde{A}^-$, from which it is straightforward to deduce the field $E_{\text{in}}(k_x + q)$. By collecting data from multiple CCD pixels, as well as by varying the acoustic wave vector q, information can be collected about the spatial spectrum of the object. The data can then be digitally processed to produce a spatial-domain image containing subwavelength details, as well as phase contrast.

Because the Bragg-shifted signal we use to decouple the $\tilde{A}_+$ and $\tilde{A}_-$ terms serves as a reference needed to record phase information, and because the image is reconstructed digitally, our technique bears some similarities with digital Fourier holography (DFH) [95, 96, 97]. However, our method contains several key enhancements over DFH. In conventional holography, care has to be taken to isolate the target signal both in real and Fourier space. This constrains reference wave geometry, translating into limitation on the field of view, as well as maximum attainable resolution. The

requirement that the CCD pixel spacing must allow for imaging the reference wave fringes further limits the resolution. By virtue of frequency-shifting the signal, it is possible to isolate the interference term of interest. Furthermore, since the spatial spectrum measurements are performed not only by selecting different CCD pixels, but also by scanning the acoustic wavevector, the limitations of CCD's physical spatial frequency bandwidth (introduced by pixel granularity) [96] can be circumvented.

We simulate the performance of the system by first using Eq. (5.15) to compute the response of the system to a calibration signal having unit amplitude for all spatial frequencies. In practice, such calibration signal might be generated by placing a point source in the vicinity of the AOM. Eq. (5.15) also provides the effective amplitude and phase transfer functions that allow to determine the detected signal for a given input field distribution. Gaussian noise is added to simulate spurious signals in the system. The input signal can then be obtained by dividing out the calibration quantities. In Fig. 5.5(b) we plot the simulated retrieved field magnitude using the same target considered in Fig. 5.3(b). Notice that the noise in the retrieved signal is lower than that observed in Fig. 5.3(c) despite a worse assumed SNR (20 dB vs 30 dB). Furthermore, because the phase information is preserved, the full 3D information about the target is collected.

5.2.8 Some practical considerations

From Eq. (5.8) we can estimate the diffraction efficiency of high spatial frequency input signal $E_{\text{in}}(k_x^{\text{in}})$ as

$$\left|t^{\pm}\right| \approx \frac{\omega/c}{2k_x^{\text{in}}} \frac{\Delta\epsilon}{n(1+n)}, \tag{5.16}$$

with $n = \sqrt{\epsilon}$ (the refractive index of the acoustic medium), and $\Delta\epsilon \propto \sqrt{F}$, the flux of acoustic energy per unit area.

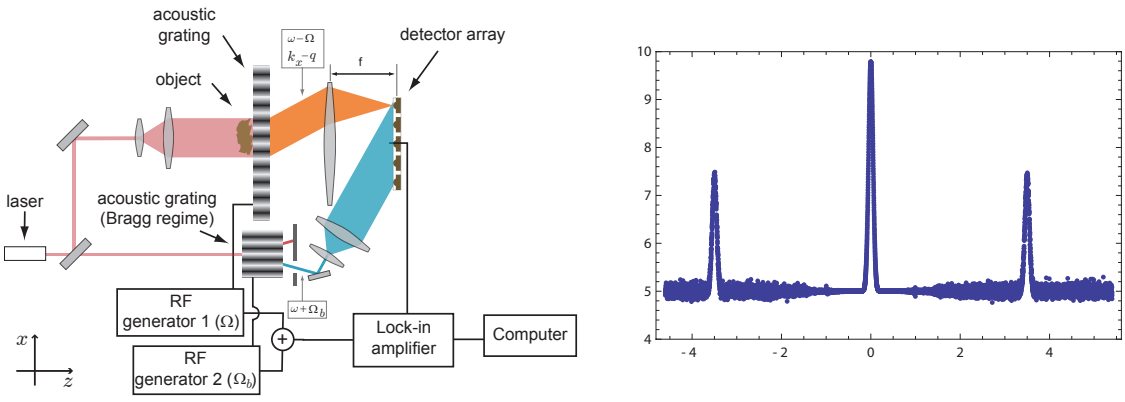

Figure 5.5: (a) Schematics of the system which utilizes a reference optical signal and a second AOM for retrieving high spatial frequency information. (b) Retrieved input field magnitude using the system in (a), assuming 20 dB SNR at the detector.

In our computations, we assume the operating wavelength of 10 μm with germanium as the acoustic medium. We take $\Delta\epsilon = 10^{-3}$ and restrict the magnitude of the acoustic wave vector q to $25\,\omega/c$. To obtain $\Delta\epsilon = 10^{-3}$ the ultrasonic fluence of 33 W/cm^2 is required. Since for high spatial frequencies $k_x^{\text{in}} \approx q$, acoustic driving frequencies up to 8.75 GHz are required to retrieve $k_x^{\text{in}} \approx 25\omega/c$. These parameters are within reach of modern ultrasonic transducers [98], as well as surface acoustic wave devices [99].

The signals are generated by sampling 10^6 points in spatial frequency space. Assuming 400 points can be sampled at once with a detector array, it is necessary to use a focusing lens with N.A. ≈ 0.6 and adjust the acoustic wave vector components $q_{x,y} \in [-25, 25]\,\omega/c$ sequentially, effectively scanning the low N.A. system over a larger spatial frequency spectrum [100, 101]. At KHz readout rates, short (< 1 s) acquisition times can be obtained with this setup.

We simulate the measurements by taking the signal indicated by Eqs. (5.10) and (5.15) and introducing additive Gaussian noise. Assuming a shot-noise limited long-wavelength IR detector with a typical detectivity $D^* \sim 10^6 \text{cm}\sqrt{\text{Hz}}/\text{W}$ [102] we find

that $\approx 20 - 30$ mW of illuminating optical power is needed to obtain SNR of $250/k_x^{\text{in}}$ used in our calculations.

Finally, we note that a potentially substantial source of noise in the proposed system is the detection of zero-order (undiffracted) illumination at the shifted frequencies due to the finite source linewidth. In the measurement region, the Lorentzian lineshape of the source takes the same $1/\Omega$ functional dependence as the diffracted signal of Eq. (5.16). Thus, the zero-order illumination simply adds a constant measurement background that may be subtracted. The noise floor is effectively raised by a factor $1/\frac{\Omega_0}{\Delta\Omega}\frac{\Delta\epsilon}{n(1+n)}$, where $\Omega_0 = v/\lambda$ is the acoustic frequency that yields $q = \omega/c$, and $\Delta\Omega$ is the source linewidth. Assuming the source is a frequency-stabilized quantum cascade laser with a ~ 15 KHz linewidth [103], this increase factor is not significant ($\lesssim 2$).

5.2.9 Potential further improvements of the setup

There exist several possible ways to enhance the functionality and the performance of the proposed devices. For instance, sensitivity may be improved by inserting a planar lens (of the "poor-man's superlens" variety) front of the acoustic wave. In the IR spectral range, such a lens may be implemented as a subwavelength layer of highly doped semiconductor. When the dielectric constant of this layer is equal to -1, the evanescent fields are strongly enhanced due to resonant coupling to surface plasmons [2, 88], increasing their scattering efficiency and leading to better SNR at the detector.

Another possible way to enhance the scattering process is by placing the sample directly in the path of an acoustic wave – for instance, by running the wave through a microchannel containing objects to be studied. Such an approach would be particularly attractive in building compact integrated systems for chemical and biological detection. Motivated by these applications, in the next section we will further develop the idea of evanescent wave scattering from targets embedded inside the grating.

5.3 Optical fingerprinting beyond the diffraction limit

5.3.1 Motivation

In the previous sections we have described a method to retrieve high spatial frequency field components by scattering on an acoustic grating. Among the advantages of this method was the ability to tune the grating period, and, more significantly, the fact that the driving signal for the grating enables the spectral offset and lock-in detection of the scattered signal. The drawbacks included relatively low scattering efficiency (caused by low effective index contrast of the grating), as well as challenges in generating GHz-range ultrasound necessary for scaling this approach from far- and mid-IR to near-IR and visible domains. One way of dealing with these problems is to abandon the idea of using the same acoustic grating for both the spatial and temporal frequency shifts. Phonon scattering can still be used for the purposes of spectral offset and signal retrieval through lock-in detection, but evanescent wave scattering can be performed using a separate nanofabricated element with high scattering efficiency and large grating wave vector. This might make it possible to construct devices that have higher sensitivity and are able to operate at visible wavelengths. In the present section we describe such a device and, using a 2D model, demonstrate that it is able to differentiate between deeply subwavelength structures. Thus, in principle, it is possible to create "fingerprints" of sub-micron-scale objects based on their characteristic spatial frequency spectrum at a particular illumination wavelength. This effectively creates a new detection modality that might join the ranks of such techniques as absorption spectroscopy, NMR, mass spectrometry, and cavity ring-down spectroscopy in identifying chemical and biological agents.

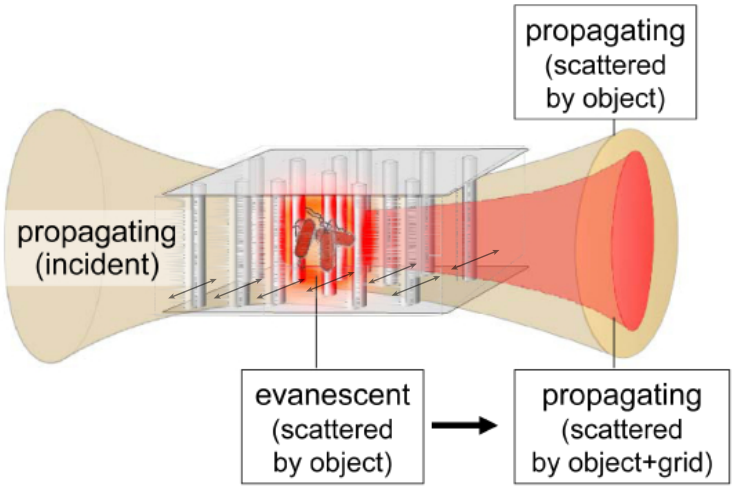

Figure 5.6: Schematics of the proposed system. Evanescent components of radiation from the sample scatter from the nanostructure and propagate into the far field. Modulation of the nanorods (indicated by the arrows) enables unambiguous recovery of the evanescent field contributions.

5.3.2 Proposed setup

The proposed detection system is shown in Fig. 5.6. The target object, embedded in a periodic patterned array, is illuminated with a plane wave. The spacing between the elements of the patterned array determines the resolution of the system, as well as the maximum allowable size of the target object. Because of this, the pictured device is particularly suitable for studying "severely subwavelength" targets.

Portion of the incident radiation that scatters from subwavelength features of the target proceeds to scatter again from the nanorod array, reducing the transverse wave vector of the signal. As a result of this wavenumber reduction, a range of waves that start out as evanescent ($k_x > k_0$) become propagating, contributing to the far-field detected intensity. Inside the nanostructure, the dielectric permittivity is modulated by a running acoustic wave as $\epsilon = \bar{\epsilon} + \Delta\epsilon \cos(qx - \Omega t)$. The frequency of the scattered signal is therefore shifted by Ω, allowing to decouple it from the rest of the propagating waves.

5.3.3 Solving the scattering problem in the Born approximation

For simplicity, we consider a system that is translation invariant in the direction of the cylindrical nanorods, perfectly aligned along the z axis. This setup naturally lends itself to a quasi-two-dimensional treatment. Accordingly, the target objects are also assumed to have infinite extent in the z direction. We will develop a perturbation theory of the scattering phenomenon, in which both the nanorods and the targets are treated as parts of the perturbing potential.

Our approach is based on the integral equation formulation of the Maxwell's equations for the relevant polarization. We will see that this naturally leads to a procedure identical to the Born approximation treatment of the scattering problem in quantum mechanics.

We start by observing that for waves with the electric field polarized in the z direction (i.e. along the nanorods) the vector wave equation reduces to its scalar version for $E \equiv E_z$:

$$\nabla^2 E + \epsilon \left(\frac{\omega}{c}\right)^2 = 0. \tag{5.17}$$

Let $\bar{\epsilon} \equiv \langle \epsilon(x, y) \rangle$ be the average dielectric constant, and we define

$$\delta\epsilon = \epsilon(x, y) - \bar{\epsilon}. \tag{5.18}$$

We can rewrite Eq. (5.17) as

$$\nabla^2 E + \bar{\epsilon} \left(\frac{\omega}{c}\right)^2 E = -\delta\epsilon \left(\frac{\omega}{c}\right)^2 E, \tag{5.19}$$

which can be solved by method of Green's functions:

$$E(\boldsymbol{r}) = E_0(\boldsymbol{r}) + \left(\frac{\omega}{c}\right)^2 \int G(\boldsymbol{r}, \boldsymbol{r'}) \delta\epsilon(\boldsymbol{r'}) E(\boldsymbol{r'}) d\boldsymbol{r'}, \tag{5.20}$$

where $E_0(\boldsymbol{r})$ is the solution to the homogeneous Helmholtz equation (i.e. Eq. (5.19) with $\delta\epsilon = 0$), and where $G(\boldsymbol{r}, \boldsymbol{r'})$ satisfies

$$\nabla^2 G(\boldsymbol{r}, \boldsymbol{r'}) - k^2 G(\boldsymbol{r}, \boldsymbol{r'}) = -\delta(\boldsymbol{r} - \boldsymbol{r'}), \tag{5.21}$$

with $k^2 \equiv \bar{\epsilon}\left(\frac{\omega}{c}\right)^2$. This is the usual Green's function for a 2D Helmholtz equation. Using the standard techniques, it can be shown that

$$G(\boldsymbol{r}, \boldsymbol{r'}) = -\frac{i}{4} H_0^{(1)}(k|\boldsymbol{r} - \boldsymbol{r'}|), \tag{5.22}$$

where $H_0^{(1)}$ is the Hankel function.

The integral formulation of the wave equation solution presented in Eq. (5.20) is identical in form to the integral solutions for wave functions in elementary scattering problems of quantum mechanics, where uniform plane waves impinge on a weak localized potential. Guided by this observation, we will perform a perturbative expansion of Eq. (5.20) and show that crucial features of plane wave propagation through the system, in particular, the "down-shifting" of high spatial frequency components of a target by scattering on the nanorods, are captured by the first two terms of the Born series.

In order for this approach to be valid, we need to assume that plane waves in this system are not strongly affected by the effective perturbing potential $\delta\epsilon(x, y)$. In turn, this means that the spatial dimensions and/or the index contrast of the scattering system are small. As a result, we may write the scattering solution as

$$\begin{aligned} E(\boldsymbol{r}) = E_0(\boldsymbol{r}) &+ \left(\frac{\omega}{c}\right)^2 \int G(\boldsymbol{r}, \boldsymbol{r'}) \delta\epsilon(\boldsymbol{r}) E_0(\boldsymbol{r'}) d\boldsymbol{r'} + \\ &+ \left(\frac{\omega}{c}\right)^4 \int G(\boldsymbol{r}, \boldsymbol{r'}) \delta\epsilon(\boldsymbol{r}) \int G(\boldsymbol{r'}, \boldsymbol{r''}) \delta\epsilon(\boldsymbol{r''}) E_0(\boldsymbol{r''}) d\boldsymbol{r''} d\boldsymbol{r'} \\ &+ O\left((\delta\epsilon)^3\right), \end{aligned} \tag{5.23}$$

where $E_0(\boldsymbol{r}) = \exp(i\boldsymbol{k}\cdot\boldsymbol{r})$. We wish to study the effects of a double scattering process, where the waves scatter from the target and then from the nanorods (or vice versa). To do so, we decompose $\delta\epsilon(\boldsymbol{r})$ as

$$\begin{aligned}\delta\epsilon(\boldsymbol{r}) &= \epsilon(\boldsymbol{r}) - \overline{\epsilon(\boldsymbol{r})} \\ &= \epsilon_{\mathrm{gr}}(\boldsymbol{r}) + \epsilon_{\mathrm{t}}(\boldsymbol{r}) - \overline{\epsilon_{\mathrm{gr}}(\boldsymbol{r}) + \epsilon_{\mathrm{t}}(\boldsymbol{r})} \\ &= \delta\epsilon_{\mathrm{gr}}(\boldsymbol{r}) + \delta\epsilon_{\mathrm{t}}(\boldsymbol{r}).^2\end{aligned} \tag{5.24}$$

Dropping the higher order terms, we abbreviate Eq. (5.23) as follows:

$$\begin{aligned}E(\boldsymbol{r}) &\simeq E_0(\boldsymbol{r}) + \mathrm{I.B.}_1 + \mathrm{I.B.}_2 \\ &\equiv E_0(\boldsymbol{r}) - \frac{i}{4}\left(\frac{\omega}{c}\right)^2 \left(\widehat{\mathrm{I.B.}}_1^{(1)} + \widehat{\mathrm{I.B.}}_1^{(2)}\right) \\ &\quad - \frac{1}{16}\left(\frac{\omega}{c}\right)^4 \left(\widehat{\mathrm{I.B.}}_2^{(1)} + \widehat{\mathrm{I.B.}}_2^{(2)} + \widehat{\mathrm{I.B.}}_2^{(3)} + \widehat{\mathrm{I.B.}}_2^{(4)}\right),\end{aligned} \tag{5.25}$$

where the terms of the form $\widehat{\mathrm{I.B.}}_n^{(k)}$ correspond to the various scattering processes in the nth order of the Born series and involve only $\delta\epsilon_{\mathrm{gr}}$, $\delta\epsilon_{\mathrm{t}}$, plane waves, and Hankel functions resulting from substituting in Eqs. (5.22) and (5.24). For example, we have

$$\begin{aligned}\widehat{\mathrm{I.B.}}_2^{(1)} &= \iint \delta\epsilon_{\mathrm{gr}}(\boldsymbol{r'})\delta\epsilon_{\mathrm{gr}}(\boldsymbol{r''})H_0^{(1)}(k|\boldsymbol{r}-\boldsymbol{r'}|)H_0^{(1)}(k|\boldsymbol{r'}-\boldsymbol{r''}|)\exp(i\boldsymbol{k}\cdot\boldsymbol{r''})d\boldsymbol{r''}d\boldsymbol{r'} \\ \widehat{\mathrm{I.B.}}_2^{(2)} &= \iint \delta\epsilon_{\mathrm{gr}}(\boldsymbol{r'})\delta\epsilon_{\mathrm{t}}(\boldsymbol{r''})H_0^{(1)}(k|\boldsymbol{r}-\boldsymbol{r'}|)H_0^{(1)}(k|\boldsymbol{r'}-\boldsymbol{r''}|)\exp(i\boldsymbol{k}\cdot\boldsymbol{r''})d\boldsymbol{r''}d\boldsymbol{r'} \\ \widehat{\mathrm{I.B.}}_2^{(3)} &= \iint \delta\epsilon_{\mathrm{t}}(\boldsymbol{r'})\delta\epsilon_{\mathrm{gr}}(\boldsymbol{r''})H_0^{(1)}(k|\boldsymbol{r}-\boldsymbol{r'}|)H_0^{(1)}(k|\boldsymbol{r'}-\boldsymbol{r''}|)\exp(i\boldsymbol{k}\cdot\boldsymbol{r''})d\boldsymbol{r''}d\boldsymbol{r'}.\end{aligned} \tag{5.26}$$

[2]This decomposition makes sense only if we specify the role of background permittivity ϵ_{b} in ϵ_{gr} or ϵ_{t}. For instance, we can stipulate that $\epsilon(\boldsymbol{r}) = \{(\epsilon_{\mathrm{nanorods}} - \epsilon_{\mathrm{b}})\mathbb{1}_{\mathrm{nanorods}}\} + \{(\epsilon_{\mathrm{t}} - \epsilon_{\mathrm{b}})\mathbb{1}_{\mathrm{target}} + \epsilon_{\mathrm{b}}\}$, where the indicator functions are nonzero only in the regions of nanorods or targets, and where the terms in braces give ϵ_{gr} and ϵ_{t} respectively.

We proceed to put in explicit expressions for a regular nanorod grid and rewrite $\delta\epsilon_{\mathrm{gr}}(\boldsymbol{r})$ and $\delta\epsilon_{\mathrm{t}}(\boldsymbol{r})$ in Fourier space:

$$\begin{aligned}
\delta\epsilon_{\mathrm{gr}}(x,y) &= \epsilon_1 \sum_{m,n} \delta(x-m\Lambda)\delta(y-n\Lambda) \circledast \operatorname{circ}\left(\frac{\sqrt{x^2+y^2}}{a}\right) - \overline{\delta\epsilon_{\mathrm{gr}}} \\
&= \pi\epsilon_1 \left(\frac{a}{\Lambda}\right)^2 \sum_{m,n} \operatorname{jinc}\left(\frac{a}{\Lambda}\sqrt{m^2+n^2}\right) e^{i\frac{2\pi}{\Lambda}(mx+ny)} - \pi\epsilon_1 \left(\frac{a}{\Lambda}\right)^2 \\
&= \pi\epsilon_1 \left(\frac{a}{\Lambda}\right)^2 \int \left[\sum_{m,n} \delta\left(q_x - m\frac{2\pi}{\Lambda}\right)\delta\left(q_y - n\frac{2\pi}{\Lambda}\right) \operatorname{jinc}\left(\frac{a}{2\pi}\sqrt{q_x^2+q_y^2}\right) - \right. \\
&\qquad\qquad \left. - \delta^{(2)}(\boldsymbol{q})\right] \exp(i\boldsymbol{q}\cdot\boldsymbol{r}) d\boldsymbol{q} \\
&\equiv \frac{a^2\epsilon_1}{4\pi} \int \text{Ш}'\left(\frac{\Lambda q_x}{2\pi}, \frac{\Lambda q_y}{2\pi}\right) \operatorname{jinc}\left(\frac{a}{2\pi}\sqrt{q_x^2+q_y^2}\right) \exp(i\boldsymbol{q}\cdot\boldsymbol{r}) d\boldsymbol{q}; \\
\delta\epsilon_{\mathrm{t}}(\boldsymbol{r}) &= \frac{1}{(2\pi)^2} \int \delta\epsilon_{\mathrm{t}}(\boldsymbol{q}) \exp(i\boldsymbol{q}\cdot\boldsymbol{r}) d\boldsymbol{q},
\end{aligned} \tag{5.27}$$

where we assume that nanorods have radius a, spacing Λ and permittivity $(\epsilon_1+\epsilon_{\mathrm{b}})$,[3] $\operatorname{circ}(r/a)$ defines a cylinder of unit height and radius a, and $\operatorname{jinc}(r)$ is the cylindrically-symmetric analog of the normalized sinc function:

$$\operatorname{jinc}(r) \equiv \frac{J_1(2\pi r)}{\pi r}. \tag{5.28}$$

In addition, we use $\text{Ш}'(x/\Lambda)$ to denote a 2D Dirac comb with spacing Λ and a removed delta function at the central coordinate $\boldsymbol{q}=0$ (hence the prime):

$$\text{Ш}'(x/\Lambda) \equiv \sum_{m\neq 0, n\neq 0} \delta(x-m\Lambda)\delta(y-n\Lambda). \tag{5.29}$$

[3]Note that we implicitly assumed *zero* permittivity outside the nanorods. This made the DC Fourier component of $\delta\epsilon_{\mathrm{gr}}$ identically zero. However, one could perform decomposition in Eq. (5.24) in a way that introduces some background permittivity into $\delta\epsilon_{\mathrm{gr}}$. In this case, a DC term in Eq. (5.27) would appear, but it would not have any time dependence, and we would be justified in dropping it when examining the acoustically modulated signal.

We will furthermore assume that the distance to the detector is large compared with the size of the scattering system. This allows to use the asymptotic form of the Hankel function:

$$H_0^{(1)}(k|\boldsymbol{r}-\boldsymbol{r'}|) \approx \frac{1+i}{\sqrt{\pi}} \frac{e^{ikr}}{\sqrt{kr}} \exp(-ik\hat{\boldsymbol{r}}\cdot\boldsymbol{r'}). \tag{5.30}$$

Finally, we assume that permittivity of the grid is modulated in space and time (e.g. with an acoustic transducer) so that the real-space and Fourier-space expression of Eq. (5.27) become

$$\begin{aligned}\delta\epsilon_{\mathrm{gr}}(x,y) &= \epsilon_1 \sum_{m,n} \delta(x-m\Lambda-\eta_x\cos(\Omega t))\delta(y-n\Lambda-\eta_y\cos(\Omega t)) \circledast \mathrm{circ}\left(\frac{\sqrt{x^2+y^2}}{a}\right) \\ &= \frac{a^2\epsilon_1}{4\pi} \int \text{Ш}'\left(\frac{\Lambda q_x}{2\pi}, \frac{\Lambda q_y}{2\pi}\right) \mathrm{jinc}\left(\frac{a}{2\pi}\sqrt{q_x^2+q_y^2}\right) \exp(i\boldsymbol{q}\cdot\boldsymbol{r}) \exp(i\boldsymbol{q}\cdot\boldsymbol{\eta}\cos(\Omega t)) d\boldsymbol{q},\end{aligned} \tag{5.31}$$

where $|\boldsymbol{\eta}| \ll \Lambda$ and $\boldsymbol{\eta} = 0$ for a static grid (no modulation).

With these approximations and Fourier-space expressions the integrals of Eq. (5.26) become straightforward (albeit cumbersome). For instance:

$$\begin{aligned}\widehat{\mathrm{I.B.}}_2^{(2)} &= \iint \delta\epsilon_{\mathrm{gr}}(\boldsymbol{r'})\delta\epsilon_{\mathrm{t}}(\boldsymbol{r''}) H_0^{(1)}(k|\boldsymbol{r}-\boldsymbol{r'}|) H_0^{(1)}(k|\boldsymbol{r'}-\boldsymbol{r''}|) \exp(i\boldsymbol{k}\cdot\boldsymbol{r''}) d\boldsymbol{r''} d\boldsymbol{r'} \\ &= C_1 \frac{e^{ikr}}{\sqrt{kr}} \iint d\boldsymbol{q'}\, d\boldsymbol{q''}\, \delta\epsilon_{\mathrm{t}}(\boldsymbol{q''}) \text{Ш}'\left(\frac{\Lambda q_x}{2\pi}, \frac{\Lambda q_y}{2\pi}\right) \mathrm{jinc}\left(\frac{a}{2\pi}\sqrt{q_x^2+q_y^2}\right) \exp(i\boldsymbol{q}\cdot\boldsymbol{\eta}\cos(\Omega t)) \\ &\qquad \times \int d\boldsymbol{r'} \exp(i\boldsymbol{q'}\cdot\boldsymbol{r'}) \exp\left[i(\boldsymbol{k}+\boldsymbol{q''})\cdot\boldsymbol{r'}\right] \exp(-ik\hat{\boldsymbol{r}}\cdot\boldsymbol{r'})) \\ &\qquad \times \int d\boldsymbol{u} \exp\left[-i(\boldsymbol{k}+\boldsymbol{q''})\cdot\boldsymbol{u}\right] H_0^{(1)}(ku),\end{aligned} \tag{5.32}$$

where we define $\boldsymbol{u} = \boldsymbol{r'} - \boldsymbol{r''}$. In this expression, the $d\boldsymbol{r'}$ integral produces a delta function:

$$\int d\boldsymbol{r'} \exp(i\boldsymbol{q'}\cdot\boldsymbol{r'}) \exp\left[i(\boldsymbol{k}+\boldsymbol{q''})\cdot\boldsymbol{r'}\right] \exp(-ik\hat{\boldsymbol{r}}\cdot\boldsymbol{r'})) = 2\pi\delta(\boldsymbol{q'}+\boldsymbol{q''}+\boldsymbol{k}-\boldsymbol{k}_{\mathrm{obs}}), \tag{5.33}$$

where $k\hat{\boldsymbol{r}} \equiv \boldsymbol{k}_{\rm obs}$ corresponds to the plane wave going from the system to the detector. The $d\boldsymbol{u}$ integral can be rewritten in polar coordinates as

$$\begin{aligned}\int H_0^{(1)}(ku)\exp\left(-i\boldsymbol{s}\cdot\boldsymbol{u}\right)d\boldsymbol{u} &= \int H_0^{(1)}(ku)e^{-i\frac{s}{k}ku\cos\theta}u\,du\,d\theta \\ &= 2\pi\int H_0^{(1)}(ku)J_0(su)udu = \frac{4}{i}\int K_0(-iku)J_0(su)u\,du \\ &= \frac{4}{i}\frac{1}{s^2-k^2}.\end{aligned} \tag{5.34}$$

where K_0 is a modified Bessel function, and the last line can be found in integral tables. Using the delta function of Eq. (5.33), we write Eq. (5.32) as

$$\begin{aligned}&\widehat{\text{I.B.}}_2^{(2)} = \\ &= C\frac{e^{ikr}}{\sqrt{kr}}\int \text{Ш}'\left(\frac{\Lambda q_x}{2\pi},\frac{\Lambda q_y}{2\pi}\right)\text{jinc}\left(\frac{a}{2\pi}\sqrt{q_x^2+q_y^2}\right)\frac{\delta\epsilon_{\rm t}(\boldsymbol{k}_{\rm obs}-\boldsymbol{k}-\boldsymbol{q})}{|\boldsymbol{k}_{\rm obs}-\boldsymbol{q}|^2-k^2}\exp(i\boldsymbol{q}\cdot\boldsymbol{\eta}\cos(\Omega t))d\boldsymbol{q}.\end{aligned} \tag{5.35}$$

The $\exp(i\boldsymbol{q}\cdot\boldsymbol{\eta}\cos(\Omega t))$ term can be represented as a sum of Bessel functions using the familiar Jacobi-Anger expansion,

$$e^{iz\cos\theta} = \sum_{n=-\infty}^{\infty} i^n J_n\left(z\right)e^{in\theta}. \tag{5.36}$$

Eq. (5.35) then becomes

$$\widehat{\text{I.B.}}_2^{(2)} = \frac{e^{ikr}}{\sqrt{kr}}\sum_{n=-\infty}^{\infty} A_n e^{in\Omega}, \tag{5.37}$$

that is, a set of cylindrical waves at harmonics of the modulation frequency Ω, with the amplitude of the nth harmonic given by

$$A_n = C\int i^n J_n\left(\boldsymbol{q}\cdot\boldsymbol{\eta}\right)\text{Ш}'\left(\frac{\Lambda q_x}{2\pi},\frac{\Lambda q_y}{2\pi}\right)\text{jinc}\left(\frac{aq}{2\pi}\right)\frac{\delta\epsilon_{\rm t}(\boldsymbol{k}_{\rm obs}-\boldsymbol{k}-\boldsymbol{q})}{q^2-2\boldsymbol{k}_{\rm obs}\cdot\boldsymbol{q}}d\boldsymbol{q}, \tag{5.38}$$

where we used the fact that $|\boldsymbol{k}_{\rm obs}| = |\boldsymbol{k}|$ to simplify the denominator.

This gives the amplitude of the detected signal for the angular spectrum component in the direction of $\boldsymbol{k}_{\rm obs}$, with $\boldsymbol{k}$ in the direction of the illuminating plane wave. Note that this term is modulated as $\exp(i\Omega t)$, which allows the signal to be isolated from the rest of the propagating spectrum. In particular, we assume that the field described by Eq. (5.37) illuminates a square-law photodetector, which is a part of a phase-sensitive (lock-in) detection setup, which uses the modulation frequency Ω as a reference. The measured signal, therefore, is proportional to $|A_m|^2$. To write the expression for $|A_m|^2$, let us first rewrite Eq. (5.38) as

$$A_m = C \sum_{\boldsymbol{q}_n}{}' i^m J_m\left(\boldsymbol{q}_n \cdot \boldsymbol{\eta}\right) \operatorname{jinc}\left(\frac{a q_n}{2\pi}\right) \frac{\delta\epsilon_{\rm t}(\boldsymbol{k}_{\rm obs} - \boldsymbol{k} - \boldsymbol{q}_n)}{q_n^2 - 2\boldsymbol{k}_{\rm obs}\cdot\boldsymbol{q}_n}, \tag{5.39}$$

where we've used the Ш function to turn the integral into a sum over the grid reciprocal lattice vectors $\boldsymbol{q}_n \equiv \frac{2\pi}{\Lambda}\{n_x, n_y\}$, with $n_x, n_y \in \mathbb{Z}^*$, the set of non-zero integers (the prime on the sum reminds us of this). The exclusion of the DC term ($\boldsymbol{q} = 0$ in Fourier space) ensures that for sufficiently small (subwavelength) values of the grid lattice constant Λ, the denominator of Eq. (5.39) never blows up.[4]

Let us also assume that the fingerprinting sample is comprised of N target objects randomly distributed in the nanorod grid. This situation is modeled by writing the

[4]What if we weren't so lucky?.. For instance, if the DC term didn't vanish, we could rewrite the $\boldsymbol{q} = \{0,0\}$ contribution to Eq. (5.38) as

$$\begin{aligned} A_m|_{\boldsymbol{q}=\{0,0\}} &\sim \lim_{\boldsymbol{q}\to\{0,0\}} \int J_m\left(\boldsymbol{q}\cdot\boldsymbol{\eta}\right) \delta\epsilon_{\rm t}(\boldsymbol{k}_{\rm obs} - \boldsymbol{k} - \boldsymbol{q}) \frac{\delta(q_x, q_y)}{2k\cos\theta} \left(\frac{1}{q - 2k\cos\theta} - \frac{1}{q}\right) q\, dq\, d\theta \\ &= \lim_{\boldsymbol{q}\to\{0,0\}} \int J_m\left(\boldsymbol{q}\cdot\boldsymbol{\eta}\right) \delta\epsilon_{\rm t}(\boldsymbol{k}_{\rm obs} - \boldsymbol{k}) \frac{\delta(q)}{2\pi k} \left(\frac{\sec^2\theta}{2k} + \frac{\sec\theta}{q}\right) dq\, d\theta, \end{aligned}$$

and looking at the $\sec\theta$, $\sec^2\theta$, and $1/q$ terms, it is clear that the integral diverges. We encounter a similarly divergent integral when q_n is too small, and we h ave $q_n = 2k\cos\theta$. This is not unexpected. A singularity in the source region is a very common feature in Green's function treatment of electromagnetic scattering problems [104, 105], and techniques to deal with the singular integrals by treating them in the principal value sense are well documented [106]. In our theory, however, these divergences do not appear.

dielectric function of the sample as

$$\delta\epsilon_{\mathrm{t}}(\boldsymbol{q}) = \int \sum_{\boldsymbol{r}_i} \delta\epsilon_{\mathrm{t}}(\boldsymbol{r} - \boldsymbol{r}_i) e^{-i\boldsymbol{q}\cdot\boldsymbol{r}} d\boldsymbol{r} = \delta\epsilon_{\mathrm{t}}^{(0)}(\boldsymbol{q}) \sum_{\boldsymbol{r}_i} e^{-i\boldsymbol{q}\cdot\boldsymbol{r}_i}, \tag{5.40}$$

where $\boldsymbol{r}_i$ is the random coordinate of an individual scatterer, and $\delta\epsilon_{\mathrm{t}}^{(0)}(\boldsymbol{q})$ is its spatial spectrum (for simplicity, we take it to be rotation-invariant). We now plug this form of the dielectric constant into Eq. (5.39), working under assumption that the grid lattice constant is $\lesssim 0.1\lambda$. This implies that $|\boldsymbol{q}_n| \gg k$, which allows us to neglect the $\boldsymbol{k}_{\mathrm{obs}}$ and $\boldsymbol{k}$ terms in Eq. (5.39) as small corrections, unless they are contributing to phase. (Observe, in particular, that this assumption disallows the possibility of getting zero in the denominator of Eq. (5.39) when $q^2 = 2\boldsymbol{k}_{\mathrm{obs}} \cdot \boldsymbol{q}$.) Also, neglecting absorption in the sample, its spatial spectrum is real, and its Fourier transform, therefore, symmetric. These approximations allow us to write

$$A_m = C \sum_{\boldsymbol{q}_n} i^m J_m\left(\boldsymbol{q}_n \cdot \boldsymbol{\eta}\right) \mathrm{jinc}\left(\frac{aq_n}{2\pi}\right) \frac{\delta\epsilon_{\mathrm{t}}^{(0)}(\boldsymbol{q}_n)}{|\boldsymbol{q}_n|^2} \sum_{\boldsymbol{r}_i} e^{i\boldsymbol{q}_n\cdot\boldsymbol{r}_i} e^{-i\Delta\boldsymbol{k}\cdot\boldsymbol{r}_i}. \tag{5.41}$$

At first glance, the sum over random phases in Eq. (5.40) has a strong negative impact on the performance of the proposed system. Indeed, $\boldsymbol{q} \cdot \boldsymbol{r}_i \sim L/\Lambda \gg 2\pi$ (where L is the size of the grid). Ordinarily, the superposition of such phases creates a complex and unpredictable interference pattern. However, as we show below, for a broad range of experimental parameters these random contributions average to zero on time and length scales relevant for optical detection.

The measured signal of the kth acoustic diffraction order can be written as

$$
\begin{aligned}
|A_k|^2 &= \left| C \sum_{\boldsymbol{q}_n} i^k J_k\left(\boldsymbol{q}_n \cdot \boldsymbol{\eta}\right) \operatorname{jinc}\left(\frac{a q_n}{2\pi}\right) \frac{\delta\epsilon_{\mathrm{t}}^{(0)}(\boldsymbol{q}_n)}{|\boldsymbol{q}_n|^2} \sum_{\boldsymbol{r}_i} e^{-i\boldsymbol{q}\cdot\boldsymbol{r}_i} \right|^2 \\
&= \left| \sum_{\boldsymbol{q}_n} F(\boldsymbol{q}_n) \sum_{\boldsymbol{r}_i} e^{-i\boldsymbol{q}\cdot\boldsymbol{r}_i} \right|^2 \\
&= \sum_{\boldsymbol{q}_n} |F(\boldsymbol{q}_n)|^2 N + \sum_{\boldsymbol{q}_n \neq \boldsymbol{q}_m} F(\boldsymbol{q}_n) F^*(\boldsymbol{q}_m) \sum_{\boldsymbol{r}_i} e^{-i(\boldsymbol{q}_n - \boldsymbol{q}_m)\cdot\boldsymbol{r}_i} \\
&\quad + \sum_{\boldsymbol{q}_n} |F(\boldsymbol{q}_n)|^2 \sum_{\boldsymbol{r}_i \neq \boldsymbol{r}_j} e^{i\boldsymbol{q}_n\cdot(\boldsymbol{r}_i - \boldsymbol{r}_j)} e^{-i\Delta\boldsymbol{k}\cdot(\boldsymbol{r}_i - \boldsymbol{r}_j)} \\
&\quad + \sum_{\boldsymbol{q}_n \neq \boldsymbol{q}_m} F(\boldsymbol{q}_n) F^*(\boldsymbol{q}_m) \sum_{\boldsymbol{r}_i \neq \boldsymbol{r}_j} e^{-i\Delta\boldsymbol{k}\cdot(\boldsymbol{r}_i - \boldsymbol{r}_j)} \exp\left[i \left(\frac{\boldsymbol{q}_n + \boldsymbol{q}_m}{2} \right) \cdot (\boldsymbol{r}_i - \boldsymbol{r}_j) \right] \times \\
&\qquad \times \exp\left[i \left(\frac{\boldsymbol{q}_n - \boldsymbol{q}_m}{2} \right) \cdot (\boldsymbol{r}_i + \boldsymbol{r}_j) \right].
\end{aligned}
\tag{5.42}
$$

Here, we explicitly separated phase factors from the other terms in the expression by defining

$$
F(\boldsymbol{q}) = i^k J_k\left(\boldsymbol{q} \cdot \boldsymbol{\eta}\right) \operatorname{jinc}\left(\frac{a q}{2\pi}\right) \frac{\delta\epsilon_{\mathrm{t}}^{(0)}(\boldsymbol{q})}{|\boldsymbol{q}|^2}. \tag{5.43}
$$

In addition, when squaring the double sum over the scatterers and the reciprocal lattice vectors, we separated out the diagonal terms. As a result, we have decomposed the measured signal into four components. The first term, diagonal in both $\boldsymbol{q}$ and $\boldsymbol{r}$, contains desired "fingerprinting" signature. As can be seen from Eq. (5.43), this signature is generated from the target object's spatial spectrum by sampling it with period determined by the grid reciprocal lattice vectors and summing the samples with weights given by $1/|\boldsymbol{q}|^2$. Notice that the strength of contributions from high spatial frequencies decreases as q^{-2}.

We will now consider the other terms in Eq. (5.42). There, the fingerprinting function $F(\boldsymbol{q})$ appears in conjunction with phase factors of the form $\exp(\Delta\boldsymbol{k} \cdot \boldsymbol{r})$

and/or $\exp(\boldsymbol{q}\cdot\boldsymbol{r})$. Because $\boldsymbol{r}$ is a random variable, one might expect these exponential factors to follow zero mean distributions. If the measurement process can be made to incorporate an appropriate averaging procedure, the contribution towards the fingerprinting signal from these random components will be negligible.

Inherently, any optical measurement must incorporate some kind of spatial and temporal averaging, since it registers the energy delivered to a finite detector area over a finite time. What does this imply for the system under consideration? We first consider the effects of the detector angular aperture. The finite value of the aperture means that the detector effectively averages the signal over several values of $\Delta\boldsymbol{k}$, where $\Delta\boldsymbol{k}$ is related to the observation angle θ and incidence angle θ_0 by

$$\Delta\boldsymbol{k} \equiv \boldsymbol{k}_{\text{obs}} - \boldsymbol{k} = \frac{\omega}{c}\left[(\cos\theta - \cos\theta_0)\hat{\boldsymbol{x}} + (\sin\theta - \sin\theta_0)\hat{\boldsymbol{y}}\right].$$

We can estimate the result of this averaging analytically by integrating over all possible scattering angles, $\theta \in [0, 2\pi]$. If the angular correlation of the field is much smaller than the angular aperture of the detector, this will be a good approximation for the detector's spatial averaging effects. We have:

$$\left\langle e^{-i\Delta\boldsymbol{k}(\theta)\cdot(\boldsymbol{r}_i-\boldsymbol{r}_j)}\right\rangle_\theta = \frac{1}{2\pi}\int_0^{2\pi} e^{-i\Delta\boldsymbol{k}(\theta)\cdot(\boldsymbol{r}_i-\boldsymbol{r}_j)}d\theta = e^{i\boldsymbol{k}\cdot(\boldsymbol{r}_i-\boldsymbol{r}_j)}J_0\left(\frac{\omega}{c}|\boldsymbol{r}_i-\boldsymbol{r}_j|\right). \tag{5.44}$$

Knowing the $1/\sqrt{x}$ asymptotic behavior of the Bessel function $J_0(x)$, and noting that $|\boldsymbol{r}_i - \boldsymbol{r}_j| \sim L$, we can conclude that for any pair $\{\boldsymbol{r}_i, \boldsymbol{r}_j\}$, Eq. (5.44) describes a random variable whose variance σ^2 is proportional to λ/L. We conclude that due to detector's finite aperture, it is possible to make the typical contribution of two of the terms in Eq. (5.42) small by considering a large enough grid size L.

Consider now the effects of finite measurement time. Recall that the target objects are suspended in a fluid. Their positions $\boldsymbol{r}_i$ are, therefore, time-dependent due to thermal motion, agitation of the fluid from the ultrasonically-modulated nanorods, as

well as the flow of the sample transported through the device. Aside from observation angle-dependent phases treated above, the dependence on $\boldsymbol{r}_i$ in Eq. (5.42) is restricted to terms of the form $\exp(i\boldsymbol{q}\cdot\boldsymbol{r}_i)$, where $|\boldsymbol{q}|$ is of the order $2\pi/\Lambda$. As discussed before, the reciprocal lattice spacing $2\pi/\Lambda$ is assumed to be $\gtrsim 2\pi \times 10/\lambda$. Consequently if every $\boldsymbol{r}_i$ changes by as little as $\lambda/10$, this will effectively give a completely different configuration. What is the typical time for the system to do so?.. If we take into account thermal motion, the rms displacement in time t given by

$$d_{\text{rms}} = \sqrt{6Dt}, \tag{5.45}$$

where the diffusion constant D is given by the Einstein-Stokes formula,

$$D = \frac{k_B T}{6\pi\eta R} = \frac{2.5\times 10^{-19}}{R} \qquad \text{(for water at room temperature)}. \tag{5.46}$$

Here, η gives the fluid's viscosity and R is the particle's radius. For relatively small objects (e.g. $R = 100$ nm at $\lambda = 10$ μm illuminating wavelength), Eq. (5.45) suggests that a new configuration is attained every 50 ms from thermal motion alone. This process occurs much quicker if we take into account the extra "kicks" that particles receive as a result of their proximity to a vibrating lattice. Assuming the vibration amplitude is 10 nm at 100 kHz, the typical velocity attained is $\sim 10^3$ μm/s. In certain circumstances (e.g., turbulent flows) we may expect this to also be the characteristic instantaneous velocity of the particles. In this case, the "reconfiguration" time drops to 1 ms.

The exact functional dependence of the averaging process' convergence to the mean depends on the physical model of particle motion. For instance, given the velocity v of the particle, we can imagine the particle holding static for time δt, followed by a Brownian kick that instantaneously displaces it a distance $v\,\delta t$ in a random direction. For $v\,\delta t \gtrsim \lambda/10$, as discussed above, this effectively results in a

completely new measurement of the phase factor $\exp(i\boldsymbol{q}\cdot\boldsymbol{r}_i)$. Averaging over the time T, then, is approximately equivalent to taking the mean of $T/\delta t \sim 10Tv/\lambda$ discrete measurements. By central limit theorem, this sample mean converges to zero as $\sqrt{\lambda/Tv}$. Alternatively, one might imagine a process where over time T, the particle has, with equal probability, visited all points on a disk of radius R. Time average is then equivalent to a spatial average over this region:

$$\langle \exp(i\boldsymbol{q}\cdot\boldsymbol{r})\rangle_{\boldsymbol{r}} = \frac{1}{\pi R}\int_0^R r\,dr\int_0^{2\pi} e^{iqr\cos\theta}d\theta = \frac{2}{qR}J_1(qR) \sim \frac{1}{(qR)^{3/2}}. \tag{5.47}$$

Motivated, again, by the ideas of Brownian motion, we suppose that $R \sim \sqrt{T}$, in which case Eq. (5.47) suggests that the rate of convergence to the zero mean is $1/T^{3/4}$.

From these considerations, we conclude that as a result of time averaging, terms with $\exp(i\boldsymbol{q}\cdot\boldsymbol{r}_i)$ phase factors do not contribute to the overall signal provided a sufficiently long integration time T is used. The net error from these terms goes to zero, at worst, as $1/\sqrt{T}$. We can rewrite Eq. (5.42), explicitly dropping the quantities that vanish from averaging:

$$\begin{aligned} |A_k|^2 &= \left|\sum_{\boldsymbol{q}_n} F(\boldsymbol{q}_n)\sum_{\boldsymbol{r}_i} e^{-i\boldsymbol{q}\cdot\boldsymbol{r}_i}\right|^2 \\ &= N\sum_{\boldsymbol{q}_n}|F(\boldsymbol{q}_n)|^2 + O\left(\frac{N}{\sqrt{T}}\right) + O\left(\frac{N}{\sqrt{LT}}\right). \end{aligned} \tag{5.48}$$

The above result was derived by assuming the scatterers to be rotationally invariant. This allowed us [in Eq. (5.40)] to decompose the spatial spectrum of a particular random realization into the transform of an individual target multiplied by a sum over random phase factors. It turns out that the procedure of averaging over realizations, motivated above by the finite integration time, can be used to relax the assumption

of rotational invariance. We return to Eq. (5.40) and rewrite it as

$$\delta\epsilon_{\mathrm{t}}(\boldsymbol{q}) = \int \sum_{\boldsymbol{r}_i} \delta\epsilon_{\mathrm{t}}(\boldsymbol{r}-\boldsymbol{r}_i) e^{-i\boldsymbol{q}\cdot\boldsymbol{r}} d\boldsymbol{r} = \sum_{\boldsymbol{r}_i} \delta\epsilon_{\mathrm{t}}^{(0)}(\boldsymbol{R}_{\theta_i}\boldsymbol{q}) e^{-i\boldsymbol{q}\cdot\boldsymbol{r}_i}, \tag{5.49}$$

where $\boldsymbol{r}_i$ is the random coordinate of an individual scatterer, and $\delta\epsilon_{\mathrm{t}}^{(0)}(\boldsymbol{q})$ is its spatial spectrum. Notice that each scatterer is rotated by a random angle θ_i; consequently, the spatial spectrum expression $\delta\epsilon_{\mathrm{t}}^{(0)}(\boldsymbol{q})$ is evaluated at the rotated Fourier coordinates $\boldsymbol{R}_{\theta_i}\boldsymbol{q}$. Now, we return to Eq. (5.42) and write down the average over $\boldsymbol{r}_i$ using the dielectric function of Eq. (5.49):

$$\begin{aligned}
\left\langle \left| A_k \right|^2 \right\rangle_{\boldsymbol{r}} &= \left\langle \left| \sum_{\boldsymbol{q}_n} \tilde{F}(\boldsymbol{q}_n) \sum_{\boldsymbol{r}_i} \delta\epsilon_{\mathrm{t}}^{(0)}(\boldsymbol{R}_{\theta_i}\boldsymbol{q}) e^{-i\boldsymbol{q}\cdot\boldsymbol{r}_i} \right|^2 \right\rangle_{\boldsymbol{r}} \\
&= \sum_{\boldsymbol{q}_n} |\tilde{F}(\boldsymbol{q}_n)|^2 \left\langle \sum_{\boldsymbol{r}_i} \left| \delta\epsilon_{\mathrm{t}}^{(0)}(\boldsymbol{R}_{\theta_i}\boldsymbol{q}_n) \right|^2 \right\rangle_{\boldsymbol{r}} \\
&+ \sum_{\boldsymbol{q}_n \neq \boldsymbol{q}_m} \tilde{F}(\boldsymbol{q}_n)\tilde{F}^*(\boldsymbol{q}_m) \left\langle \sum_{\boldsymbol{r}_i} \delta\epsilon_{\mathrm{t}}^{(0)}(\boldsymbol{R}_{\theta_i}\boldsymbol{q}_n) \delta\epsilon_{\mathrm{t}}^{(0)^*}(\boldsymbol{R}_{\theta_i}\boldsymbol{q}_m) e^{-i(\boldsymbol{q}_n-\boldsymbol{q}_m)\cdot\boldsymbol{r}_i} \right\rangle_{\boldsymbol{r}} \\
&+ \sum_{\boldsymbol{q}_n} |\tilde{F}(\boldsymbol{q}_n)|^2 \left\langle \sum_{\boldsymbol{r}_i \neq \boldsymbol{r}_j} \delta\epsilon_{\mathrm{t}}^{(0)}(\boldsymbol{R}_{\theta_i}\boldsymbol{q}_n) \delta\epsilon_{\mathrm{t}}^{(0)^*}(\boldsymbol{R}_{\theta_j}\boldsymbol{q}_n) e^{i\boldsymbol{q}_n\cdot(\boldsymbol{r}_i-\boldsymbol{r}_j)} e^{-i\Delta\boldsymbol{k}\cdot(\boldsymbol{r}_i-\boldsymbol{r}_j)} \right\rangle_{\boldsymbol{r}} \\
&+ \sum_{\boldsymbol{q}_n \neq \boldsymbol{q}_m} \tilde{F}(\boldsymbol{q}_n)\tilde{F}^*(\boldsymbol{q}_m) \left\langle \sum_{\boldsymbol{r}_i \neq \boldsymbol{r}_j} \delta\epsilon_{\mathrm{t}}^{(0)}(\boldsymbol{R}_{\theta_i}\boldsymbol{q}_n) \delta\epsilon_{\mathrm{t}}^{(0)^*}(\boldsymbol{R}_{\theta_j}\boldsymbol{q}_m) e^{-i\Delta\boldsymbol{k}\cdot(\boldsymbol{r}_i-\boldsymbol{r}_j)} \right. \\
&\qquad \left. \times \exp\left[i\left(\frac{\boldsymbol{q}_n+\boldsymbol{q}_m}{2} \right) \cdot (\boldsymbol{r}_i-\boldsymbol{r}_j) \right] \exp\left[i\left(\frac{\boldsymbol{q}_n-\boldsymbol{q}_m}{2} \right) \cdot (\boldsymbol{r}_i+\boldsymbol{r}_j) \right] \right\rangle_{\boldsymbol{r}}.
\end{aligned} \tag{5.50}$$

Here, $\tilde{F}(\boldsymbol{q})$ is defined as

$$\tilde{F}(\boldsymbol{q}) = i^k J_k(\boldsymbol{q}\cdot\boldsymbol{\eta}) \,\mathrm{jinc}\left(\frac{aq}{2\pi}\right) \frac{1}{|\boldsymbol{q}|^2}. \tag{5.51}$$

We can also rewrite the average over orientations as

$$\left\langle \sum_{\boldsymbol{r}_i} \delta\epsilon_{\mathrm{t}}^{(0)}(\boldsymbol{R}_{\theta_i}\boldsymbol{q}) \right\rangle_{\boldsymbol{r}} = \frac{N}{2\pi}\int_0^{2\pi} \delta\epsilon_{\mathrm{t}}^{(0)}(\boldsymbol{R}_{\theta}\boldsymbol{q})d\theta \equiv N\delta\epsilon_{\mathrm{t}}^{\mathrm{av}}(q) \tag{5.52}$$

Once again, the off-diagonal ($\boldsymbol{r}_i \neq \boldsymbol{r}_j$, $\boldsymbol{q}_n \neq \boldsymbol{q}_m$) terms can be neglected given sufficiently long integration time. We are left, then, with an answer identical to the one before [Eq. (5.48)]; the only change is that $\delta\epsilon_{\mathrm{t}}^{(0)}$ is replaced by the angular average $\delta\epsilon_{\mathrm{t}}^{\mathrm{av}}$ defined in Eq. (5.52).

In summary, the collected signal is represented as the following sum over the grid reciprocal lattice vectors:

$$|A_k|^2 = N\sum_{\boldsymbol{q}}{}' \left| i^k J_k\left(\boldsymbol{q}\cdot\boldsymbol{\eta}\right) \mathrm{jinc}\left(\frac{aq}{2\pi}\right) \frac{\delta\epsilon_{\mathrm{t}}^{\mathrm{av}}(q)}{q^2} \right|^2 + O\left(\frac{N}{\sqrt{T}}\right). \tag{5.53}$$

Recall that the index k represents the signal shifted by k acoustic frequencies as per Eq. (5.37). Without loss of generality, we can select the $k = 1$ term for detection (this is analogous to picking the first diffracted order in the Raman-Nath treatment of the acoustooptic effect). Remembering that the vibrational displacement vector is small ($\boldsymbol{\eta} \ll \lambda$), and hence, $J_1\left(\boldsymbol{q}\cdot\boldsymbol{\eta}\right) \approx \boldsymbol{q}\cdot\boldsymbol{\eta}$, the expression for the signal becomes

$$|A|^2 = N\sum_{\boldsymbol{q}}{}' \left| \boldsymbol{q}\cdot\boldsymbol{\eta}\, \mathrm{jinc}\left(\frac{aq}{2\pi}\right) \frac{\delta\epsilon_{\mathrm{t}}^{\mathrm{av}}(q)}{q^2} \right|^2 + O\left(\frac{N}{\sqrt{T}}\right). \tag{5.54}$$

In other words, this is the sum of samples of the 2D spatial frequency distribution of individual targets, averaged over the angle, with samples taken at spatial frequencies $\boldsymbol{q}$, $\boldsymbol{q} \neq 0$. The jinc term provides an overall envelope that is determined by the transform of an individual nanorod (or, more generally, by the transform of a grid's unit cell).

What are the effects of choosing different periods for the grid?.. We can understand this by examining Fig. 5.7, which shows a typical radially symmetric spatial

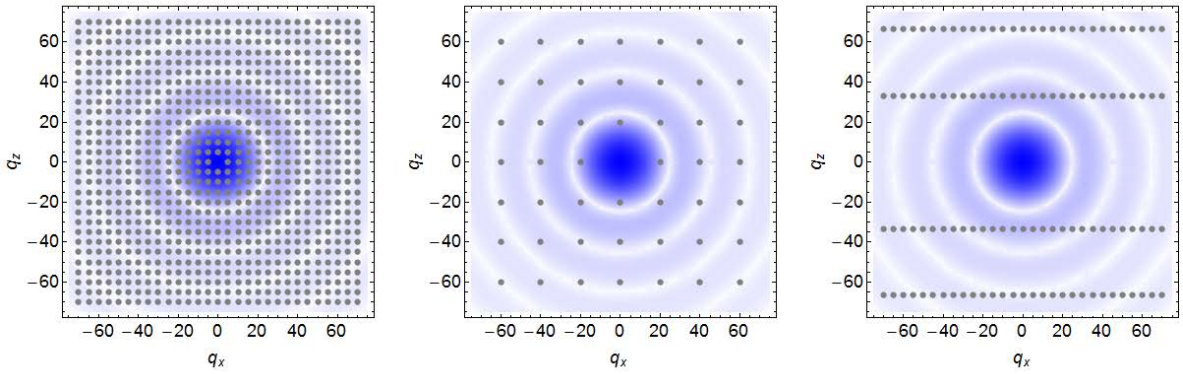

Figure 5.7: Spatial frequency space sampling for a typical target of size $\lambda/20$. (a) Isotropic grid with spacing $\lambda/5$ (b) Isotropic grid with spacing $\lambda/20$ (c) Anisotropic grid with spacing $\{\lambda/5, \lambda/30\}$. The $q_y = 0$ row of sampling points is removed if one assumes the acoustic displacement vector to be $\boldsymbol{\eta} = \eta\hat{\boldsymbol{y}}$, which implies Eq. (5.54) gives 0 for $q_y = 0$.

frequency plot for a target with a diameter $\lambda/20$. The dots represent the sampling points. Panel (a) of Fig. 5.7 shows the sampling point density for a grid of period $\lambda/5$ in either direction. This causes the samples to be concentrated in the central spatial frequency lobe. Technically, this central lobe still contains subwavelength components, and provided the number of targets N is fixed in Eq. (5.54), the relative strength of contributions to these central spatial frequencies could be used to differentiate between various subwavelength particles of different sizes (e.g. $\lambda/20$ vs $\lambda/30$). Fixing, or, more generally, controlling for the number of particles N is not unrealistic and can be done with many techniques, e.g. flow cytometry, but we would like to minimize the complexity of the proposed apparatus. Therefore, we wish to explore setups that are not sensitive to N.

Our first observation is that by decreasing the period of the grid, we effectively spread the sampling points apart in Fourier space. We can imagine tuning the grid size in order to position these sampling points at specific spatial frequencies that we would like to detect. One possible approach is shown in Fig. 5.7(b), where the grid period is the minimum allowed such that the targets still fit inside the structure. One

might imagine that this arrangement might be better at picking up features carried by higher spatial frequencies. However, using such a fine grid carries with itself various manufacturing and experimental challenges.

Three facts may help get around these problems. First, we note that the period of the grid need not be isotropic in the two directions. In particular, we can imagine a very small spacing between the nanorods in the y direction, leading to large values of spatial frequency components q_y, however, a reasonably large spacing in the x direction will still allow the target particles to move through the device. Additionally, this large spacing leads to dense clustering of sampling points along the q_x coordinate. In other words, we can pick a value of q_y to target a particular range of spatial frequencies, and then use dense sampling points in the q_x direction to maximize the signal from these components.

The second feature of our system we would like to utilize is the freedom to pick the acoustic displacement vector $\boldsymbol{\eta}$. In particular, if one assumes the acoustic displacement vector to be $\boldsymbol{\eta} = \eta\hat{\boldsymbol{y}}$, Eq. (5.54) gives 0 for $q_y = 0$. This has the effect of removing a row of sampling points that would otherwise pass through the strong central lobe of the Fourier signal, and allows to focus on the higher (but weaker) spatial frequency components instead. The sampling point arrangement corresponding to this system is illustrated in Fig. 5.7(c).

Finally, we note that while the grid spacing is "hardwired" by the manufacturing process, it is easy to manufacture "chirped" grids, with varying periods. In particular, we can take the grid that gives the sampling points of Fig. 5.7(c) and make the period in the y direction vary smoothly along the grating. Observe that this is also the direction that the sample particles are free to travel in. Thus, by collecting the signal from the different parts of the device, we are effectively sweeping the ($q_y = \text{const}$) rows of sampling points, probing the different regions of the spatial frequency space.

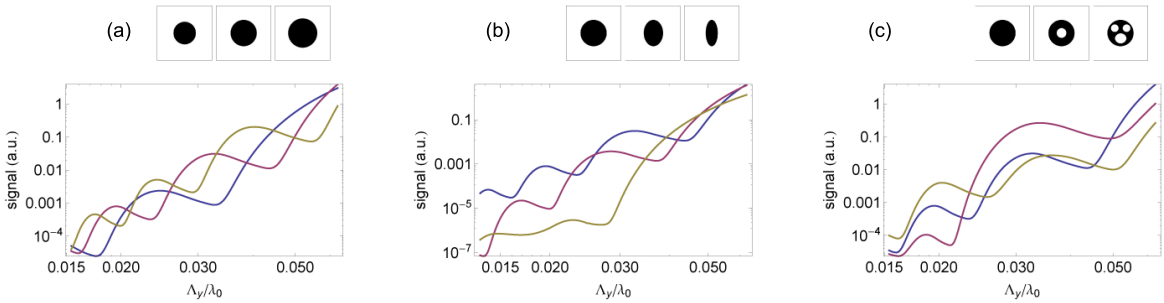

Figure 5.8: Simulated signal as a function of grating period in the y direction.

5.3.4 Simulation results

To illustrate the ability of the proposed system to distinguish between subwavelength particles, in Fig. 5.8 we plot the signal computed from Eq. (5.54) as a function of the grating period in the y direction (Λ_y). As a basic model target, we take a cylinder with diameter $\lambda/20$. We then explore how the computed signal differs as we perturb the target's size, shape, and as we introduce some inner structure to the particle [panels (a), (b), and (c) of Fig. 5.8]. The abscissas indicate the local period of the nanostructure in the y direction in units of $1/\lambda$. This can be thought of as a spatial scale on which the target is probed. The curves, plotted on the log-log scale, illustrate the differences between signals for the different conformations of our model particle, depicted above the panels. We note that the secular trend of the curves indicates a power law decrease of the signal as spatial frequencies increase; in most optical systems this decrease is expected to be exponential.

The clear differences between the curves in each panel of Fig. 5.8 suggest that changes in either the size, shape, or structure of targets on a deeply subwavelength scale can be detected with our proposed approach. We note, however, that due to angular averaging over multiple randomly oriented targets, this scheme is sensitive only to the average radial spatial frequency distributions in the sample, which are not necessarily unique. Thus, these signals do not provide unambiguous signatures for arbitrary targets. However, even with this limitation it should be possible to extract

useful information given some prior knowledge about the sample under study. For instance, given a mixture containing the differently-sized particles of Fig. 5.8(a), we could estimate the size of the smallest component in the mixture by observing the location of the first minimum of the signal as the period Λ_y decreases. Similarly, for a circle/ellipsoid family of Fig. 5.8(b), we could estimate the eccentricity of the "narrowest" ellipsoid.

If it is known that only *one* out of a set of possible targets is present, its identity could be revealed by comparing the data to known calibration signals.

Finally, we can also imagine other experiments, in which the shape or structure of the target is changing in real time under the influence of some external mechanism (e.g. mitochondria undergoing calcium overload [107] or cells undergoing apoptosis [108]). Looking at the curves of Fig. 5.8(b) it's easy to see that as the ellipsoidal targets become deformed into spheres (a good model for the calcium-induced alterations in mitochondrial morphology [107]), the signal changes rather dramatically. Thus, the proposed system could be used to detect real-time target morphology changes on a deeply subwavelength scale.

5.4 Conclusion

Systems described in this chapter provide a new approach towards far-field retrieval of evanescent waves by using diffraction on a modulated subwavelength structure. Several possible implementations of this idea exist: for mid-IR and higher wavelengths, acoustic phonons can serve as a dynamic grating that is tunable and does not require nanofabrication. In the visible range, scattering can be performed using a periodic nanostructure that is modulated via external means. An important point to emphasize is that it is the scale of the patterning that determines the maximum spatial frequencies accessible by this device. Although in our discussions, we assumed that the

nanoparticle targets we are trying to detect are embedded in the nanopatterned grating, we expect the general conclusions to hold for the case of targets deposited on top of the grating. Alternatively, "embedding" may be performed by etching microchannels in the patterned device for the nanoparticles. This would remove constraints on the particle size that exist with the nanorod-based device illustrated earlier.

Existing schemes for nanoparticle detection and differentiation that have been reported in the literature, for the most part, use the spatial frequency information only indirectly: for example, the strong dependence between a particle's scattering cross section and its radius can be used to differentiate individual particles by size [109]. With the methods described in this chapter, it is possible to create a much richer spatial frequency fingerprint for nanoscale objects, creating a new and, potentially, significant detection modality.

Chapter 6

Conclusion

In the introduction to this thesis, we gave one definition of metamaterials as "artificial media with unusual electromagnetic properties". This definition is deliberately vague: what is unusual to one person might seem quite usual to another. Moreover, the qualitative evolution of this perception can differ rather drastically as one gains knowledge about the subject. In some cases, things that seem unusual at the start will become commonplace as the inquiry progresses. In many other cases, the mystery only deepens as knowledge accumulates. The researcher may feel as confused as ever – albeit, on a higher level and about more important things. This is usually a sign of a good research problem.

The study of metamaterials in general, and hyperbolic metamaterials in particular, falls firmly in this latter category of problems. Anisotropic metamaterials with hyperbolic dispersion relations were originally proposed as a simple alternative to negatively refractive media operating via magnetic resonances. The basic operating principles of all-angle negative refraction of hyperbolic materials are easy to understand for anyone that has studied birefringence. Despite this superficial simplicity, this class of metamaterials demonstrates unusual properties that go far beyond the geometry of refraction. For example, we have seen that with appropriate boundary

conditions, negative refraction results in negative phase velocity. We have shown how this phenomenon arises in metallic, dielectric, and bilayer waveguides and studied its implications in creating slow light devices.

Perhaps more importantly, we demonstrated that the unbounded dispersion branches alter the very fundamentals of wave propagation in bulk hyperbolic materials, which, in turn, enables novel devices with a multitude of prospective applications, the most prominent of which we described in this work. We have seen how arbitrarily large values of the wave vector (limited only by the material patterning scale) can be used for subwavelength light confinement and focusing. This is potentially important for nonlinear optical devices, which operate at high field intensities. In the imaging domain, we have seen that the high-k bulk waves can couple to high spatial frequency Fourier field harmonics, which exponentially decay in free space. We can then employ scattering from a subwavelength structure, or magnification in cylindrical geometry, to convert those high-k harmonics into propagating waves, thereby gathering subwavelength information in the far field.

Aside from merely allowing high-k modes, the hyperbolic nature of dispersion suggests that the *density* of such states is (formally) infinite. We studied the resultant singularity in the photonic density of states and its role in creating radiative decay channels that enhance the fluorescence of a dipole emitter. We also discussed its role in enabling the hyperlens, where it allows propagation of high angular momentum states. These extra scattering channels serve as extra information channels carrying subwavelength information.

In the last chapter of this thesis, we focused on the idea of optical detection as a scattering problem and presented a particular approach to optical fingerprinting that relied on detecting high spatial frequency signals scattered from a subwavelength grating. While the proposed devices did not require hyperbolic dispersion, we found

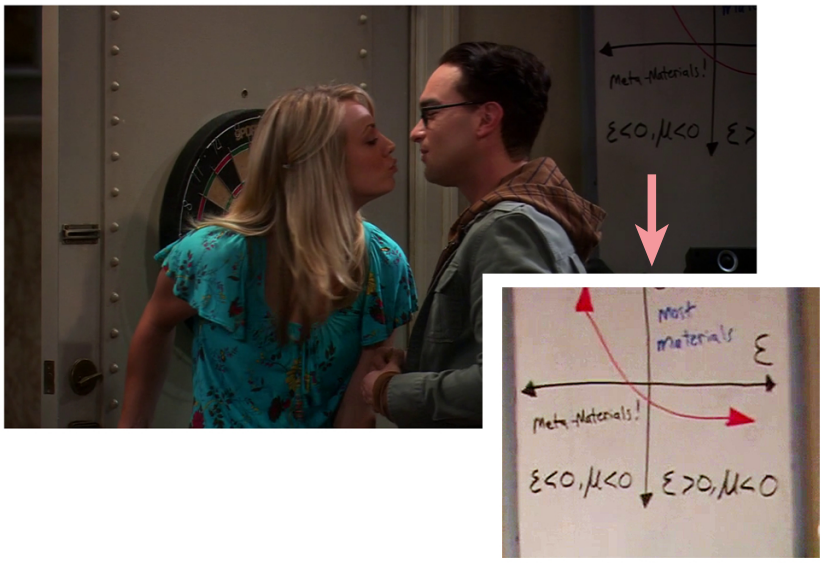

Figure 6.1: A frame from *Big Bang Theory*, season 3, episode 5, first aired on October 19, 2009. Source: CBS/Viacom

that anisotropic patterning was important in determining the spatial frequencies that can be probed by a subwavelength structure.

As we conclude this thesis, it is natural to look ahead and comment briefly on the current evolution of metamaterials in general, and hyperbolic metamaterials in particular. In the introductory chapter, we presented a plot detailing the number of metamaterials-related publications produced over the last 12 years. Re-examining this plot, we see that the initial period of enthusiasm and excitement (and exponential growth, as reflected by the number of publications) has now given way to an era that some commentators have described as "sober assessment" [110]. In the process of this assessment, it has been noted that the focus is shifting from thinking of metamaterials as materials, to thinking of them primarily as devices [110]. This thesis has presented a clear example of this evolution. Indeed, we spent the majority of the time discussing *devices* enabled by the unusual properties of hyperbolic media.

In the coming years, we expect to see the emergence of metamaterial devices with tunable, switchable, or nonlinear response. Hyperbolic metamaterials have every

opportunity to be at the forefront of this research. After all, the ability to tailor electromagnetic response of planar heterostructures which was used to demonstrate the first all-semiconductor hyperbolic metamaterial [62] has become common in active optoelectronic devices (such as quantum cascade lasers), as well as in photonic crystal and plasmonic systems. In addition, we have only begun to scratch the surface in finding applications of the density of states "hypersingularity". Prospective research in this area spans the range from designing materials for energy harvesting, to creating optical analogs of exotic quantum gravity effects such as metric transitions [6].

Finally, we would like to express one more hope for hyperbolic metamaterials. In October of 2009, 13.5 million Americans had a chance to see the "traditional" $\{\epsilon < 0, \mu < 0\}$ metamaterials making a cameo appearance on the whiteboard belonging to the characters of the hit prime time CBS show *The Big Bang Theory* (Fig. 6.1). We firmly believe that hyperbolic metamaterials are equally as deserving to be mentioned on network television, and will make every effort to lobby for their appearance.

Appendix A

Reflection and transmission of dipole radiation

A.1 Field of an electric dipole

A.1.1 Space domain

The electric field obeys

$$\boldsymbol{\nabla} \times \boldsymbol{\nabla} \times \boldsymbol{E} - k^2 \boldsymbol{E} = i\omega\mu \boldsymbol{j}. \tag{A.1}$$

On the other hand, the field (assuming the Lorenz gauge) also satisfies

$$\boldsymbol{E} = i\omega \left[\boldsymbol{A} + \frac{1}{k^2} \boldsymbol{\nabla}(\boldsymbol{\nabla} \cdot \boldsymbol{A}) \right], \tag{A.2}$$

where $k \equiv \omega/c$ and the vector potential $\boldsymbol{A}$ satisfies

$$-(\nabla^2 + k^2)\boldsymbol{A} = \mu \boldsymbol{j}. \tag{A.3}$$

We define a dyadic Green's function $\boldsymbol{G}$ as

$$\boldsymbol{\nabla} \times \boldsymbol{\nabla} \times \boldsymbol{G} - k^2 \boldsymbol{G} = \mathbf{1}\delta(\boldsymbol{r} - \boldsymbol{r'}), \tag{A.4}$$

where the vector operators are understood to act on each column of $\boldsymbol{G}$ separately. Each i^{th} column of $\boldsymbol{G}$ can be regarded as a field due to a point current source $\boldsymbol{j} = (1/i\omega\mu)\hat{\boldsymbol{e}}_i\delta(\boldsymbol{r} - \boldsymbol{r'})$. It follows from Eq. (A.3) that the corresponding vector potential obeys

$$-(\nabla^2 + k^2)\boldsymbol{A} = \frac{1}{i\omega}\hat{\boldsymbol{e}}_i\delta(\boldsymbol{r} - \boldsymbol{r'}). \tag{A.5}$$

The solution of this equation is $\boldsymbol{A} = \frac{1}{i\omega} g(\boldsymbol{r}, \boldsymbol{r'})\hat{\boldsymbol{e}}_i$, where $g(\boldsymbol{r}, \boldsymbol{r'})$ is the well-known scalar Green's function for the Helmholtz equation:

$$-(\nabla^2 + k^2)g = \delta(\boldsymbol{r} - \boldsymbol{r'}); \tag{A.6}$$

$$g(\boldsymbol{r}, \boldsymbol{r'}) = \frac{e^{ik|\boldsymbol{r} - \boldsymbol{r'}|}}{4\pi|\boldsymbol{r} - \boldsymbol{r'}|}. \tag{A.7}$$

Plugging this result into Eq. (A.2) we obtain for the i^{th} column of $\boldsymbol{G}$

$$\boldsymbol{G}_i = \left(\hat{\boldsymbol{e}}_i + \frac{1}{k^2}\boldsymbol{\nabla}\partial_i\right) g(\boldsymbol{r} - \boldsymbol{r'}),$$

which gives for the final form of the dyadic Green's function:

$$\boldsymbol{G} = \left(\mathbf{1} + \frac{1}{k^2}\boldsymbol{\nabla}\boldsymbol{\nabla}\right) g(\boldsymbol{r}, \boldsymbol{r'}). \tag{A.8}$$

The electric field can now be found from the given source current as

$$\boldsymbol{E}(\boldsymbol{r}) = i\omega\mu \int \boldsymbol{G}(\boldsymbol{r}, \boldsymbol{r'}) \cdot \boldsymbol{j}(\boldsymbol{r'}) d\boldsymbol{r'}, \tag{A.9}$$

or [using Eq. (A.7)] as

$$\boldsymbol{E}(\boldsymbol{r}) = i\omega\mu \left(\mathbf{1} + \frac{1}{k^2}\boldsymbol{\nabla}\boldsymbol{\nabla}\right) \int \frac{e^{ik|\boldsymbol{r}-\boldsymbol{r'}|}}{4\pi|\boldsymbol{r}-\boldsymbol{r'}|}\boldsymbol{j}(\boldsymbol{r'})d\boldsymbol{r'}. \tag{A.10}$$

We can use this formula to find the fields due to a Hertzian dipole. To avoid introducing local field corrections [111, 112], the surrounding medium is taken to be vacuum. Such dipole can be represented by a delta-function current source at a height h above the z=0 plane, with $\boldsymbol{m}$ giving its strength and orientation:

$$\boldsymbol{j}(\boldsymbol{r}, t) = -i\omega\boldsymbol{m}\exp(-i\omega t)\delta(\boldsymbol{r} - h\hat{\boldsymbol{z}}). \tag{A.11}$$

The electric field due to this dipole is given by

$$\boldsymbol{E}(\boldsymbol{r}) = i\omega\mu \left(\mathbf{1} + \frac{1}{k^2}\nabla\nabla\right) \left(-i\omega\boldsymbol{m}\frac{e^{ik|\boldsymbol{r}-h\hat{\boldsymbol{z}}|}}{4\pi|\boldsymbol{r}-h\hat{\boldsymbol{z}}|}\right). \tag{A.12}$$

It is straightforward to compute the actual expression. For example, in the case of vertically oriented dipole ($\boldsymbol{m} = m\hat{\boldsymbol{z}}$) the electric field becomes

$$\boldsymbol{E}(\boldsymbol{r}) = \frac{\mu m\omega^2}{4\pi k^2}e^{ikR}\left[\left(\frac{k^2}{R} + \frac{ik}{R^2} - \frac{1}{R^3}\right)\hat{\boldsymbol{z}} + \left(-\frac{k^2}{R^3} - \frac{3ik}{R^4} + \frac{3}{R^5}\right)(z-h)\boldsymbol{R}\right], \tag{A.13}$$

where $\boldsymbol{R} = x\,\hat{\boldsymbol{x}} + y\,\hat{\boldsymbol{y}} + (z-h)\hat{\boldsymbol{z}}$ and $R \equiv |\boldsymbol{R}|$.

A.1.2 Spatial frequency domain

When considering a dipole in the presence of dielectric or conducting media, it is often necessary to compute the reflected and transmitted fields, or to study the effects of surface modes. Such calculations require decomposing the electric field into its spatial

frequency spectrum. We will be using the following Fourier expansion:

$$\boldsymbol{E}(\boldsymbol{r},\omega) = \int \boldsymbol{E}(\boldsymbol{k},\omega)\exp(i\boldsymbol{k}\cdot\boldsymbol{r})d\boldsymbol{k} \tag{A.14}$$

To get the dipole fields, we start with Eq. (A.12), writing it as

$$\boldsymbol{E}(\boldsymbol{r},\omega) = \frac{\omega^2\mu_0}{(\omega/c)^2}\left[(\omega/c)^2\mathbf{1} + \boldsymbol{\nabla}\boldsymbol{\nabla}\right]\boldsymbol{m}\; g(\boldsymbol{r},\boldsymbol{r'})|_{\boldsymbol{r'}=h\hat{\boldsymbol{z}}}\,. \tag{A.15}$$

We can write

$$\begin{aligned}\boldsymbol{\nabla}\boldsymbol{\nabla}\boldsymbol{m}g(\boldsymbol{r},\boldsymbol{r'}) &= \boldsymbol{\nabla}[\boldsymbol{\nabla}\cdot\boldsymbol{m}g(\boldsymbol{r},\boldsymbol{r'})] \\ &= \boldsymbol{\nabla}\times\boldsymbol{\nabla}\times[\boldsymbol{m}g(\boldsymbol{r},\boldsymbol{r'})] - \boldsymbol{m}\left[\delta(\boldsymbol{r}-\boldsymbol{r'}) + (\omega/c)^2 g(\boldsymbol{r},\boldsymbol{r'})\right],\end{aligned}$$

where we used Eq. (A.6). With this substitution, Eq. (A.15) becomes

$$\boldsymbol{E}(\boldsymbol{r},\omega) = \frac{\omega^2\mu_0}{(\omega/c)^2}\left\{-\boldsymbol{m}\delta(\boldsymbol{r}-\boldsymbol{r'}) + \boldsymbol{\nabla}\times\boldsymbol{\nabla}\times[\boldsymbol{m}g(\boldsymbol{r},\boldsymbol{r'})]\right\}|_{\boldsymbol{r'}=h\hat{\boldsymbol{z}}}\,. \tag{A.16}$$

In our Fourier representation, we have

$$\delta(\boldsymbol{r}-\boldsymbol{r'}) = \frac{1}{(2\pi)^3}\int e^{i\boldsymbol{k}\cdot(\boldsymbol{r}-\boldsymbol{r'})}d\boldsymbol{k}.$$

$$\begin{aligned}g(\boldsymbol{r},\boldsymbol{r'}) &= \frac{1}{(2\pi)^3}\int \frac{e^{i\boldsymbol{k}\cdot(\boldsymbol{r}-\boldsymbol{r'})}}{k^2-(\omega/c)^2}d\boldsymbol{k} \\ &= -\frac{1}{(2\pi)^3}\int d\boldsymbol{k}_\perp e^{i\boldsymbol{k}_\perp\cdot\boldsymbol{r}_\perp}\int dk_z \frac{e^{i(k_z(z-h))}}{(\omega/c)^2-k_\perp^2-k_z^2}.\end{aligned} \tag{A.17}$$

We can perform the integral

$$I_0 \equiv \int dk_z \frac{e^{ik_z(z-h)}}{(q_z+k_z)(q_z-k_z)},$$

where we defined $q_z^2 := (\omega/c)^2 - k_\perp^2$. For $z > h$ we close the contour in the upper half-plane, in which case Cauchy's Residue Theorem gives

$$I_0 = -2\pi i \frac{e^{iq_z(z-h)}}{2q_z}$$

as the value of the integral. For $z < h$, we close the contour in the lower half-plane, in which case we get

$$I_0 = -2\pi i \frac{e^{-iq_z(z-h)}}{2q_z}.$$

We therefore obtain

$$g(\boldsymbol{r}, \boldsymbol{r'} = h\hat{\boldsymbol{z}}) = \frac{i}{(2\pi)^2} \int d\boldsymbol{k}_\perp e^{i\boldsymbol{k}_\perp \cdot \boldsymbol{r}_\perp} \frac{1}{2q_z} e^{iq_z|z-h|}. \tag{A.18}$$

To make it more convenient to work with the $|z-h|$ term in our equations, we define $\boldsymbol{k_1} := k_x\hat{\boldsymbol{x}} + k_y\hat{\boldsymbol{y}} + q_z \text{sign}(h-z)\hat{\boldsymbol{z}}$.

We can finally express Eq. (A.16) as an integral over the transverse wave vector $\boldsymbol{k}_\perp$:

$$\boldsymbol{E} = \frac{\omega^2\mu_0}{(\omega/c)^2(2\pi)^2} \int d\boldsymbol{k}_\perp e^{i\boldsymbol{k}_\perp \cdot \boldsymbol{r}_\perp} \left[-\boldsymbol{m}\delta(z-h) - i\boldsymbol{k_1} \times \boldsymbol{k_1} \times \boldsymbol{m} \frac{e^{iq_z|z-h|}}{2q_z} \right]. \tag{A.19}$$

In order to enable separate treatment of the two polarization components, we rewrite this equation as

$$\boldsymbol{E} = \frac{1}{\epsilon_0} \frac{1}{(2\pi)^2} \int d\boldsymbol{k}_\perp e^{i\boldsymbol{k}_\perp \cdot \boldsymbol{r}_\perp} \left\{ -\boldsymbol{m}\delta(z-h) + i\left[(\boldsymbol{m}\cdot\boldsymbol{p})\boldsymbol{p} + (\boldsymbol{m}\cdot\boldsymbol{s})\boldsymbol{s} \right] \frac{e^{iq_z|z-h|}}{2q_z} \right\}, \tag{A.20}$$

where $\boldsymbol{p} = k_\perp\hat{\boldsymbol{z}} + q_z \text{sign}(h-z)\hat{\boldsymbol{k}}_\perp$ and $\boldsymbol{s} = (\hat{\boldsymbol{z}} \times \hat{\boldsymbol{k}}_\perp)\sqrt{k_\perp^2 + q_z^2} = (\hat{\boldsymbol{z}} \times \hat{\boldsymbol{k}}_\perp)\sqrt{\epsilon\mu}(\omega/c)$ (in the case of isotropic medium) are vectors indicating P- and S-polarization.

To make these equations more suitable for numerical computations it is advantageous to rewrite the integral in polar coordinates and integrate over the angle variable. In particular, we make the substitutions

$$\boldsymbol{k}_\perp \cdot \boldsymbol{r}_\perp \to kr\cos(\theta), \;\; d\boldsymbol{k}_\perp \to k dk d\theta, \;\; \hat{\boldsymbol{k}}_\perp \to R_z(\theta)\cdot\hat{\boldsymbol{r}}_\perp, \tag{A.21}$$

with $R_z(\theta)$ being the usual matrix of rotations around the z axis. Performing the θ integral gives:

$$\begin{aligned}\boldsymbol{E} = \frac{1}{\epsilon_0}\frac{1}{(2\pi)^2}\int k\,dk\Bigg\{ & -J_0(kr)\boldsymbol{m}\delta(z-h)+ \\ & + i\left[\begin{pmatrix} -\frac{\tilde{q}_z^2 J_1(kr)\left(m_x\left(x^2-y^2\right)+2xym_y\right)}{kr^3} + \frac{x\tilde{q}_z^2 J_0(kr)(xm_x+ym_y)}{r^2} + \frac{ikxm_z\tilde{q}_z J_1(kr)}{r} \\ \frac{\tilde{q}_z^2 J_1(kr)\left(m_y\left(x^2-y^2\right)-2xym_x\right)}{kr^3} + \frac{y\tilde{q}_z^2 J_0(kr)(xm_x+ym_y)}{r^2} + \frac{ikym_z\tilde{q}_z J_1(kr)}{r} \\ k^2 m_z J_0(kr) + \frac{ik\tilde{q}_z J_1(kr)(xm_x+ym_y)}{r} \end{pmatrix}\right. \\ & \left. + \begin{pmatrix} \frac{J_1(kr)\left(m_x\left(x^2-y^2\right)+2xym_y\right)}{kr^3} + \frac{yJ_0(kr)(ym_x-xm_y)}{r^2} \\ \frac{J_1(kr)\left(m_y\left(y^2-x^2\right)+2xym_x\right)}{kr^3} + \frac{xJ_0(kr)(xm_y-ym_x)}{r^2} \\ 0 \end{pmatrix}\right] \frac{e^{-i\tilde{q}_z(z-h)}}{2|\tilde{q}_z|}\Bigg\}, \end{aligned} \tag{A.22}$$

where $k = \sqrt{k_x^2+k_y^2}$, $r = \sqrt{x^2+y^2}$, $\tilde{q}_z := \mathrm{sign}(h-z)\sqrt{(\omega/c)^2-k^2}$, and the column elements are the Cartesian x, y, z components of the field. Note that the first term in the square brackets corresponds to P polarization, and the second term gives the S polarization.

For the case of a vertically-oriented dipole ($\boldsymbol{m} = m\hat{\boldsymbol{z}}$), the S polarization component vanishes, and the p polarization component becomes substantially more tractable:

$$\boldsymbol{E} = -\frac{1}{\epsilon_0}\frac{im}{(2\pi)^2}\int k^2\,dk\left[\frac{\tilde{q}_z}{r}(x\hat{\boldsymbol{x}}+y\hat{\boldsymbol{y}})iJ_1(kr) + kJ_0(kr)\hat{\boldsymbol{z}}\right]\frac{e^{-i\tilde{q}_z(z-h)}}{2|\tilde{q}_z|}. \tag{A.23}$$

(Note that from this point onwards we will drop the delta function term at the location of the dipole, since we are interested in fields elsewhere.)

Although the resulting expression appears considerably simpler, there remain certain difficulties when treating this integral numerically. First, the integrand is a diverging oscillatory function in the plane of the dipole, $z = h$. It is therefore necessary to compute the integral for $z = h + \epsilon$ and follow a limiting procedure as $\epsilon \to 0$. Second, the integrand oscillates rapidly for $kr \gg 1$; as a result, standard numerical integration algorithms fail or suffer inaccuracies. This problem can be avoided with a change of variables, effectively integrating over the quantity kr. In particular, using $I_1(a, b)$ to denote the integral in Eq. (A.23) with integration limits a and b, we obtain

$$\begin{aligned}\boldsymbol{E} =& \frac{1}{\epsilon_0}\frac{im}{(2\pi)^2}[I_1(0,\omega/c) + I_1(\omega/c,\infty)] \\ =& \frac{1}{\epsilon_0}\frac{im}{(2\pi)^2}\left\{ I_1(0,\omega/c) + \int_{\xi_0}^{\infty} \frac{\xi^2}{r^2}\, d\xi \;\times \right. \\ & \left. \times \left[\mathrm{sign}(h-z)\frac{\sqrt{\xi_0^2-\xi^2}}{r}(x\hat{\boldsymbol{x}} + y\hat{\boldsymbol{y}})iJ_1(\xi) + \frac{\xi}{r}J_0(\xi)\hat{\boldsymbol{z}} \right] \frac{e^{i\sqrt{\xi_0^2-\xi^2}|z-h|/r}}{\sqrt{\xi_0^2-\xi^2}} \right\},\end{aligned} \tag{A.24}$$

where $\xi \equiv kr$, $\xi_0 \equiv r\omega/c$.

A.2 Reflection and transmission of dipole radiation

We now consider the problem of a dipole radiating above a homogeneous half-infinite medium with the boundary at $z = 0$, as illustrated in Fig. A.1. If the plane wave reflection and transmission coefficients at the boundary are known, with the help of Eq. (A.20) we can compute the field everywhere in space. (This approach works not just for a half-infinite medium, but in fact for any stratified planar structure with a well-defined transfer function.) The exact expression is

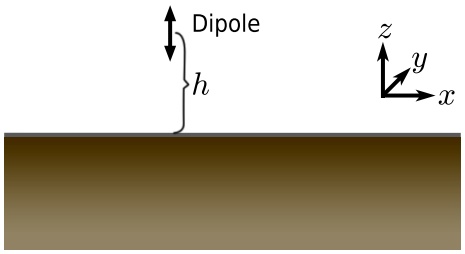

Figure A.1: Geometry of the problem. The dipole is situated in vacuum in the vicinity of a planar substrate, with $z = 0$ as the boundary.

$$\begin{aligned}\boldsymbol{E} =& \frac{i}{2(2\pi)^2}\int d\boldsymbol{k}_\perp e^{i\boldsymbol{k}_\perp\cdot\boldsymbol{r}_\perp}\frac{1}{\epsilon_0}\frac{(\boldsymbol{m}\cdot\boldsymbol{p}_i)}{q_z^{(1)}}\Big\{\Big[\boldsymbol{p}_i e^{iq_z^{(1)}|z-h|}+ \\ &+\ r_p\boldsymbol{p}_r e^{iq_z^{(1)}(z+h)}\Big]\theta(-z)+\boldsymbol{\epsilon}^{-1}t_p\boldsymbol{p}_t e^{-iq_z^{(2p)}z}e^{iq^{(1)}h}\theta(z)\Big\},\end{aligned} \tag{A.25}$$

where $q_z^{(1)}$ and $q_z^{(2p)}$ denote the propagation vector in medium 1 and 2 respectively, $\boldsymbol{\epsilon}$ (assumed to be diagonal) is the dielectric tensor in medium 2, and $\theta(z)$ is the step function. We have, furthermore,

$$\begin{aligned}\boldsymbol{p}_i =& k_\perp\hat{\boldsymbol{z}} + q_z^{(1)}\mathrm{sign}(h-z)\hat{\boldsymbol{k}}_\perp \\ \boldsymbol{p}_r =& k_\perp\hat{\boldsymbol{z}} - q_z^{(1)}\hat{\boldsymbol{k}}_\perp \\ \boldsymbol{p}_t =& k_\perp\hat{\boldsymbol{z}} + q_z^{(2p)}\hat{\boldsymbol{k}}_\perp.\end{aligned} \tag{A.26}$$

A very similar expression can be written for the S polarization:

$$\begin{aligned}\boldsymbol{E} =& \frac{i}{2(2\pi)^2}\int d\boldsymbol{k}_\perp e^{i\boldsymbol{k}_\perp\cdot\boldsymbol{r}_\perp}\frac{1}{\epsilon_0}\frac{(\boldsymbol{m}\cdot\boldsymbol{s}_i)}{q_z^{(1)}}\Big\{\Big[\boldsymbol{s}_i e^{iq_z^{(1)}|z-h|}+ \\ &+\ r_s\boldsymbol{s}_r e^{iq_z^{(1)}(z+h)}\Big]\theta(-z)+\boldsymbol{\epsilon}^{-1}t_s\boldsymbol{s}_t e^{-iq_z^{(2s)}z}e^{iq^{(1)}h}\theta(z)\Big\},\end{aligned} \tag{A.27}$$

with $\boldsymbol{s}_i = \boldsymbol{s}_r = (\hat{\boldsymbol{z}}\times\hat{\boldsymbol{k}}_\perp)\sqrt{k_\perp^2+[q_z^{(1)}]^2}$; $\boldsymbol{s}_t = (\hat{\boldsymbol{z}}\times\hat{\boldsymbol{k}}_\perp)\sqrt{k_\perp^2+[q_z^{(2s)}]^2}$.

Specifically, we would like to return to the case of a vertically-oriented dipole and consider its field in the vicinity of a uniaxial anisotropic material. The dielectric tensor of this material is

$$\boldsymbol{\epsilon} = \begin{pmatrix} \epsilon_x & 0 & 0 \\ 0 & \epsilon_x & 0 \\ 0 & 0 & \epsilon_z \end{pmatrix}, \tag{A.28}$$

and the propagation vectors in this material are

$$q_z^{(2p)} = \sqrt{\epsilon_x \mu \left(\frac{\omega}{c}\right)^2 - \frac{\epsilon_x}{\epsilon_z} k_\perp^2} \tag{A.29}$$

$$q_z^{(2s)} = \sqrt{\epsilon_x \mu \left(\frac{\omega}{c}\right)^2 - k_\perp^2}. \tag{A.30}$$

The reflection and transmission coefficients are given by the standard formulas:

$$r_p = \frac{\epsilon_x^{(2)} q_z^{(1)} - \epsilon_x^{(1)} q_z^{(2)}}{\epsilon_x^{(2)} q_z^{(1)} + \epsilon_x^{(1)} q_z^{(2)}} \qquad t_p = \frac{2\epsilon_x^{(1)} q_z^{(1)}}{\epsilon_x^{(2)} q_z^{(1)} + \epsilon_x^{(1)} q_z^{(2)}} \tag{A.31}$$

As before, we can introduce polar coordinates and integrate over the angular dimension. With this approach, we can write the electric field of a z-oriented dipole

over an anisotropic half-space as

$$\boldsymbol{E} = \frac{1}{\epsilon_0}\frac{im}{2(2\pi)^2}\int k^2\,dk \frac{1}{q_z^{(1)}}\frac{1}{r}\left\{\left[\left(\begin{array}{c}\tilde{q}_z^{(1)} xiJ_1(kr)\\ \tilde{q}_z^{(1)} yiJ_1(kr)\\ krJ_0(kr)\end{array}\right)e^{-i\tilde{q}_z(z-h)} + \right.\right.$$
$$\left.\left. + \; r_p\left(\begin{array}{c}-q_z^{(1)} xiJ_1(kr)\\ -q_z^{(1)} yiJ_1(kr)\\ krJ_0(kr)\end{array}\right)e^{iq_z^{(1)}(z+h)}\right]\theta(-z) + \right. \qquad \text{(A.32)}$$
$$\left. + \; t_p\left(\begin{array}{c}q_z^{(2p)} xiJ_1(kr)/\epsilon_x\\ q_z^{(2p)} yiJ_1(kr)/\epsilon_x\\ krJ_0(kr)/\epsilon_z\end{array}\right)e^{-iq_z^{(2p)}z}e^{iq^{(1)}h}\theta(z)\right\}$$

(as before, column vectors correspond to the Cartesian components of the field).

This integral can be readily computed numerically using methods described above.

Appendix B

Dirac trick

In order to obtain a clear distinction between the behaviors of different systems we consider, and to fully understand the effect of losses it is sometimes desirable to perform computations while setting losses to zero. This presents problems when equations of interest feature resonant denominators, as in the Eq. (3.19).

The situation is remedied by the observation that in the limit as losses approach zero, the resonant peaks resemble delta functions, which greatly simplifies the integration procedure. This result (sometimes called the "Dirac trick") is known as the Sokhotsky-Weierstrass theorem, which, in its simple form, states:

$$\lim_{\epsilon \to 0^+} \int_a^b \frac{f(x)}{x \pm i\epsilon} dx = \mp i\pi f(0) + P \int_a^b \frac{f(x)}{x} dx. \tag{B.1}$$

Note that since all the quantities are assumed to be real, we trivially obtain the imaginary part of the integral via delta-function integration. For more complex denominators, such as the ones treated here, the theorem can be rewritten as

$$\lim_{\epsilon \to 0^+} \int_a^b \frac{g_1(x)}{g_2(x) \pm i\epsilon} dx = \mp i\pi \sum_{\{x_0\}} \frac{g_1(x_0)}{|g_2'(x_0)|} + P \int_a^b \frac{g_1(x)}{g_2(x)} dx, \tag{B.2}$$

where x_0 are the roots of $g_2(x)$. Once again, the imaginary part of the integral is obtained by an algebraic evaluation – provided the roots of $g_2(x)$ are known. For the systems described above, these roots had to be determined numerically – however, the problem of root finding is more easily tractable than that of numerical integration over very sharp resonances. Moreover, once these roots have been found, it is straightforward to adapt numerical integration algorithms for considering small finite losses, e.g. by changing variables to effectively "stretch" the integrand in the vicinity of resonances, or by guiding singularity handlers in commercial computer algebra packages.

Appendix C

Transfer matrix formalism for the slab lens problem

C.1 Transfer matrix analysis

A slab lens can be thought of as a generalization of an n-layer planar stack with n=1. Let us consider a symmetric slab lens with TM-polarized plane waves impinging upon it. We choose the propagation vector to be in the z direction, and assume material parameters in region 1 and 3 are identical ($\epsilon_1 = \epsilon_3$; $\mu_1 = \mu_3$). Let the transverse wave vector $\vec{k}_{\|} = k_x\hat{\mathbf{x}}$. Because $\vec{k}_{\|}$ is conserved across planar interfaces, we have $k_x^{(1)} = k_x^{(2)} = k_x^{(3)} := k_x$. For the z component of the wave vector we have

$$k_z = \sqrt{\epsilon\mu\left(\frac{\omega}{c}\right)^2 - k_x^2}, \tag{C.1}$$

thus we also write $k_z^{(1)} = k_z^{(3)} := k_z^{(1)}$.

Because we are treating TM modes only here, we can define the fields in the structure in terms of a single transverse component of the magnetic field. For the field in the i^{th}region we write the field as a sum of forward- and backwards- propagating

waves:

$$\vec{B}^{(i)} = -e^{i(k_x x + k_y y)} \left(a^{(i)} e^{i k_z^{(i)} z} + b^{(i)} e^{-i k_z^{(i)} z} \right) \hat{\mathbf{x}}. \tag{C.2}$$

In what follows we will often write $a^{(i)}$and $b^{(i)}$ as a vector:

$$A^{(i)} := \begin{pmatrix} a^{(i)} \\ b^{(i)} \end{pmatrix}. \tag{C.3}$$

Let's also assume that the system admits uniaxial anisotropy, where $(\epsilon_x = \epsilon_y := \epsilon_\parallel) \neq \epsilon_z$, and similarly with μ. Note that for TM modes, only $\mu_\parallel$ plays a role, so in the context of the TM mode discussion we will use $\mu := \mu_\parallel$.

Given Eq. C.2 we can write the expression for the E-field from Maxwell's equations:

$$-i\omega \boldsymbol{\epsilon}^{(i)} \cdot \vec{E}^{(i)} = \overrightarrow{\nabla} \times \frac{\vec{B}^{(i)}}{\mu^{(i)}} = \frac{1}{\mu^{(i)}} \begin{pmatrix} 0 \\ \partial_z B_x^{(i)} \\ -\partial_y B_x^{(i)} \end{pmatrix} = -\frac{i}{\mu^{(i)}} \begin{pmatrix} 0 \\ k_z^{(i)} \left(a^{(i)} - b^{(i)} \right) \\ -k_y \left(a^{(i)} + b^{(i)} \right) \end{pmatrix};$$

$$\vec{E}^{(i)} = \frac{1}{\omega} \begin{pmatrix} 0 \\ k_z^{(i)} \left(a^{(i)} - b^{(i)} \right) / \epsilon_y^{(i)} \\ -k_y \left(a^{(i)} + b^{(i)} \right) / \epsilon_z^{(i)} \end{pmatrix} \frac{\vec{B}^{(i)}}{\mu^{(i)}}.$$

At this point it becomes convenient to rewrite Eq. C.2 in regions (1) and (3) as follows:

$$\vec{B}^{(1)} = -e^{i(k_x x + k_y y)} \left(\widetilde{a}^{(1)} e^{i k_z^{(1)} (z - z_1)} + \widetilde{b}^{(1)} e^{-i k_z^{(1)} (z - z_1)} \right) \hat{\mathbf{x}}, \text{ and}$$

$$\vec{B}^{(3)} = -e^{i(k_x x + k_y y)} \left(\widetilde{a}^{(3)} e^{i k_z^{(1)} (z - z_2)} + \widetilde{b}^{(3)} e^{-i k_z^{(1)} (z - z_2)} \right) \hat{\mathbf{x}},$$

where $z_1$and z_2 are the coordinates of the first and the second interface of the slab lens. We further define

$$\widetilde{a}_{-}^{(2)} = a^{(2)} e^{ik_z^{(2)} z_1} \text{ and } \widetilde{b}_{-}^{(2)} = b^{(2)} e^{-ik_z^{(2)} z_1};$$

$$\widetilde{a}_{+}^{(2)} = a^{(2)} e^{ik_z^{(2)} z_2} \text{ and } \widetilde{b}_{+}^{(2)} = b^{(2)} e^{-ik_z^{(2)} z_2},$$

as well as the propagation matrix

$$T_P^{(2)}(z_2 - z_1) = \begin{pmatrix} e^{ik_z^{(2)}(z_2 - z_1)} & 0 \\ 0 & e^{-ik_z^{(2)}(z_2 - z_1)} \end{pmatrix}.$$

(Note that using notation of Eq. C.3, we have $\tilde{A}_{+}^{(2)} = T_P^{(2)} \cdot \tilde{A}_{-}^{(2)}$).

Continuity of E_y and B_x/μ across the first interface give, respectively,

$$k_z^{(1)} \left(\widetilde{a}^{(1)} - \widetilde{b}^{(1)} \right) / \epsilon_y^{(1)} = k_z^{(2)} \left(\widetilde{a}_{-}^{(2)} - \widetilde{b}_{-}^{(2)} \right) / \epsilon_y^{(2)} \text{ and}$$

$$\widetilde{a}^{(1)} + \widetilde{b}^{(1)} = \widetilde{a}_{-}^{(2)} + \widetilde{b}_{-}^{(2)}.$$

We can rewrite this as

$$\frac{1}{2} \begin{pmatrix} 1 + K^{(12)} & 1 - K^{(12)} \\ 1 - K^{(12)} & 1 + K^{(12)} \end{pmatrix} \begin{pmatrix} \widetilde{a}^{(1)} \\ \widetilde{b}^{(1)} \end{pmatrix} = \begin{pmatrix} \widetilde{a}_{-}^{(2)} \\ \widetilde{b}_{-}^{(2)} \end{pmatrix},$$

where $K^{(ij)} := k_z^{(i)} \epsilon_y^{(j)} / k_z^{(j)} \epsilon_y^{(i)}$. Denoting the interface matching matrix on the left-hand side as $T_I^{(12)}$, we write the above equation as

$$\tilde{A}_{-}^{(2)} = T_I^{(12)} \cdot \tilde{A}^{(1)}.$$

Similarly, we have

$$\tilde{A}^{(3)} = T_I^{(21)} \cdot \tilde{A}_+^{(2)},$$

and combining this with the propagation matrix we obtain

$$\tilde{A}^{(3)} = T_I^{(21)} \cdot T_P^{(2)}(z_2 - z_1) \cdot T_I^{(12)} \tilde{A}^{(1)}.$$

Finally, let us choose to compare the fields a distance h from the slab interfaces. We have

$$\vec{B}^{(1)}(z_1 - h) = -e^{i(k_x x + k_y y)} \left(\widetilde{a}^{(1)} e^{-ik_z^{(1)} h} + \widetilde{b}^{(1)} e^{ik_z^{(1)} h} \right) \hat{\mathbf{x}} := -e^{i(k_x x + k_y y)} \left(\widetilde{a}^{(o)} + \widetilde{b}^{(o)} \right) \hat{\mathbf{x}}, \text{ and}$$

$$\vec{B}^{(3)}(z_2 + h) = -e^{i(k_x x + k_y y)} \left(\widetilde{a}^{(3)} e^{ik_z^{(1)} h} + \widetilde{b}^{(3)} e^{-ik_z^{(1)} h} \right) \hat{\mathbf{x}} := -e^{i(k_x x + k_y y)} \left(\widetilde{a}^{(i)} + \widetilde{b}^{(i)} \right) \hat{\mathbf{x}}$$

– here (o) and (i) stand for object and image. We define the transfer matrix T between the object and the image point as

$$\tilde{A}^{(i)} = T_P^{(1)}(h) \cdot T_I^{(21)} \cdot T_P^{(2)}(z_2 - z_1) \cdot T_I^{(12)} \cdot T_P^{(1)}(h) \cdot \tilde{A}^{(o)} := T(d, \boldsymbol{\epsilon}, \boldsymbol{\mu}, h) \cdot \tilde{A}^{(o)},$$

where $d = z_2 - z_1$. Performing the matrix multiplications, we obtain the following result:

$$T(d, \boldsymbol{\epsilon}, \boldsymbol{\mu}, h) = \frac{1}{2} \sin\left(k_z^{(2)} d\right) \times$$
$$\times \begin{pmatrix} e^{i2hk_z^{(1)}} \left[2\cot\left(k_z^{(2)} d\right) + i\left(\frac{\epsilon_1 k_z^{(2)}}{\epsilon_2 k_z^{(1)}} + \frac{\epsilon_2 k_z^{(1)}}{\epsilon_1 k_z^{(2)}} \right) \right] & i\left(\frac{\epsilon_1 k_z^{(2)}}{\epsilon_2 k_z^{(1)}} - \frac{\epsilon_2 k_z^{(1)}}{\epsilon_1 k_z^{(2)}} \right) \\ -i\left(\frac{\epsilon_1 k_z^{(2)}}{\epsilon_2 k_z^{(1)}} - \frac{\epsilon_2 k_z^{(1)}}{\epsilon_1 k_z^{(2)}} \right) & e^{-i2hk_z^{(1)}} \left[2\cot\left(k_z^{(2)} d\right) - i\left(\frac{\epsilon_1 k_z^{(2)}}{\epsilon_2 k_z^{(1)}} + \frac{\epsilon_2 k_z^{(1)}}{\epsilon_1 k_z^{(2)}} \right) \right] \end{pmatrix}.$$

We note that the determinant of the matrix is 1.

Reflection and transmission coefficients for the fields are defined as

$$r = \frac{\widetilde{b}^{(o)}}{\widetilde{a}^{(o)}} = -\frac{T_{21}}{T_{22}} \text{ and } t = \frac{\widetilde{a}^{(i)}}{\widetilde{a}^{(o)}} = \frac{\det T}{T_{22}} = \frac{1}{T_{22}}.$$

When expressed as a function of transverse wave vector k_x, the field transmission coefficient t can be thought of as a spatial frequency transfer function. For high values of k_x (in particular, values so high that in the absense of losses $k_z^{(i)}$ becomes purely imaginary and the wave becomes evanescent) it is convenient to define

$$k_z^{(i)} = i\widetilde{k}_z^{(i)}, \;\; \widetilde{k}_z^{(i)} \in \Re \text{ (for the lossless case).}$$

(The definition is made largely for the sake of convenience; using Eq. C.4 as originally written is just as valid – one simply needs to deal with many complex quantities.) With this substitution, we have

$$t = e^{-2h\tilde{k}_z^{(1)}} \left[\cosh\left(\tilde{k}_z^{(2)} d\right) + \frac{1}{2}\left(\frac{\epsilon_1 \tilde{k}_z^{(2)}}{\epsilon_2 \tilde{k}_z^{(1)}} + \frac{\epsilon_2 \tilde{k}_z^{(1)}}{\epsilon_1 \tilde{k}_z^{(2)}} \right) \sinh\left(\tilde{k}_z^{(2)} d\right) \right]^{-1}. \tag{C.4}$$

In the case $\epsilon_1 = \mu_1 = 1$; $\epsilon_2 = \mu_2 = -1$ we get $\tilde{k}_z^{(1)} = \tilde{k}_z^{(2)}$, and the transfer function expressed as a function of spatial frequency becomes

$$t(k_x) = \frac{e^{-2h\tilde{k}_z^{(1)}}}{\cosh\left(\tilde{k}_z^{(1)} d\right) - \sinh\left(\tilde{k}_z^{(1)} d\right)} = e^{(d-2h)\sqrt{k_x^2 - (\omega/c)^2}}. \tag{C.5}$$

C.2 Superlens and its limitations

By inspection of Eq. (C.5), we conclude that for $h = d/2$ we get $t = 1$ everywhere. This is precisely the superlensing condition as described by Pendry [2]. More generally, we use the identity

$$2\coth(x) = \tanh\left(\frac{x}{2}\right) + \coth\left(\frac{x}{2}\right)$$

to write the transfer function as

$$
\begin{aligned}
&t(k_x) = \\
&= e^{-2h\tilde{k}_z^{(1)}} \left\{ \frac{1}{2} \sinh\left(\tilde{k}_z^{(2)} d\right) \left[\left(\tanh\left(\tilde{k}_z^{(2)} \frac{d}{2}\right) + \frac{\epsilon_2 \tilde{k}_z^{(1)}}{\epsilon_1 \tilde{k}_z^{(2)}} \right) + \left(\coth\left(\tilde{k}_z^{(2)} \frac{d}{2}\right) + \frac{\epsilon_1 \tilde{k}_z^{(2)}}{\epsilon_2 \tilde{k}_z^{(1)}} \right) \right] \right\}^{-1} \\
&= e^{-2h\tilde{k}_z^{(1)}} \left\{ \frac{1}{2} \sinh\left(\tilde{k}_z^{(2)} d\right) \left[\left(\tanh\left(\tilde{k}_z^{(2)} \frac{d}{2}\right) + \frac{\epsilon_1 \tilde{k}_z^{(2)}}{\epsilon_2 \tilde{k}_z^{(1)}} \right) + \left(\coth\left(\tilde{k}_z^{(2)} \frac{d}{2}\right) + \frac{\epsilon_2 \tilde{k}_z^{(1)}}{\epsilon_1 \tilde{k}_z^{(2)}} \right) \right] \right\}^{-1}.
\end{aligned}
\tag{C.6}
$$

The transfer function has two poles: one where $\tanh\left(\tilde{k}_z^{(2)} \frac{d}{2}\right) = -\frac{\epsilon_2 \tilde{k}_z^{(1)}}{\epsilon_1 \tilde{k}_z^{(2)}}$ is satisfied, and another where $\coth\left(\tilde{k}_z^{(2)} \frac{d}{2}\right) = -\frac{\epsilon_2 \tilde{k}_z^{(1)}}{\epsilon_1 \tilde{k}_z^{(2)}}$ is satisfied. It is important to note that the first equality is exactly the dispersion relation for symmetric plasmons, while the second one is the dispersion relation for antisymmetric plasmons. The peaks of the transfer function, thus, are determined by the location of plasmon resonances. For a perfect superlens, we see that both of the plasmon resonance poles move to $+\infty$ in spatial frequency.

What happens to the not-so-perfect superlens? We take $\epsilon_1 = \mu_1 = 1$, $\epsilon_2 = -1 + \delta\epsilon$, and expand the term in front of sinh in Eq. C.4 in powers of k_x^{-1} and $\delta\epsilon$. Retaining terms up to $k_x^{-4}$and collecting the powers of $\delta\epsilon$, we get

$$
\begin{aligned}
t(k_x) &= \frac{e^{-2h\tilde{k}_z^{(1)}}}{\cosh\left(\tilde{k}_z^{(2)} d\right) - \left[1 + \frac{1}{2}\left(\frac{(1+\mu_2)^2}{4k_x^4} + \frac{\delta\epsilon(1+\mu_2)}{k_x^2} + \delta\epsilon^2\right)\right] \sinh\left(\tilde{k}_z^{(2)} d\right)} \\
&\simeq \frac{1}{1 - \frac{1}{4}\left(\frac{(1+\mu_2)^2}{4k_x^4} + \frac{\delta\epsilon(1+\mu_2)}{k_x^2} + \delta\epsilon^2\right)\left(e^{2d\tilde{k}_z^{(2)}} - 1\right)} \quad \text{for } h = d/2
\end{aligned}
\tag{C.7}
$$

Note that for $\mu_2 = -1$, $\delta\epsilon = 0$ we get back the usual $t(k_x) = 1$ of the ideal superlens. For $\mu_2 = -1$, $\delta\epsilon \neq 0$, we have a pole at $k_x = \frac{1}{2d} \log \frac{4}{\delta\epsilon^2} \simeq \frac{1}{2d}(1 - 2\log|\delta\epsilon|)$. For larger values of k_x exponential decay takes over. Taken another way, if we would like to retain the passband of the transfer function up to a particular value $k_x^{\max}$, the

maximum allowed deviation from the ideal case is

$$|\delta\epsilon| = 2\exp(-dk_x^{\max}).$$

Note that this equation is valid for complex values of $\delta\epsilon$: when losses are present, the spikes of the transfer function corresponding to real-ϵ poles get smoothed out, however the transfer function still decays exponentially past the location of the poles. This means that the superlens is exponentially sensitive to losses.

Suppose now that $\epsilon_2 = -1$, $\mu_2 = 1$, $\delta\epsilon = 0$ – an ideal "poor man's" superlens. What are its fundamental limitations? We find from the denominator of Eq. C.7 that having $\mu_2 = 1$, $\delta\epsilon = 0$ is approximately equivalent to having $|\delta\epsilon| = 1/k_x^2$ in the $\mu_2 = -1$ case (the slight difference in $\tilde{k}_z^{(2)}$ between the two cases is immaterial). As before, to find the cut-off frequency of this lens we need to determine the values of k_x for which $\frac{1}{4k_x^4}\left(e^{2dk_x} - 1\right) \gg 1$.

The general form of the curve reflects the fact that for small values of k_x, the $1/k_x^4$ term dominates, while for larger values the growing exponent takes over. Furthermore, can see that there are two regimes: for small enough values of d, the function becomes 1 in two places, resulting in poles in the transmission function Eq. C.7. After the right-most pole, exponential decay would dominate the transfer function. The poles, however, are not always present: for larger values of d, the function never crosses 1 and thus the poles never materialize. The general behavior of the function remains the same, however: the denominator starts growing exponentially, and the transfer function once again undergoes cutoff. To quantify the cut-off point in this case instead of finding the right-most pole, one can examine e.g. the local minimum of the function, which can serve as a good proxy for the point at which the exponent takes over the $1/k_x^4$ term. The solutions for cut-off points can be obtained numerically.

We find that the cut-off frequency becomes large for thin slabs – largely due to the fact that for $d/\lambda <\approx 0.16$ the transfer function has poles corresponding to symmetric plasmon polaritons, and the resonant frequency of the plasmon responsible for the right-most pole becomes larger as the slab becomes thinner.

Bibliography

[1] D. Smith, W. Padilla, D. Vier, S. Nemat-Nasser, and S. Schultz, "Composite medium with simultaneously negative permeability and permittivity," *Physical Review Letters*, vol. 84, pp. 4184–7, May 2000.

[2] J. Pendry, "Negative Refraction Makes a Perfect Lens," *Physical Review Letters*, vol. 85, no. 18, pp. 3966–3969, 2000.

[3] R. Merlin, "Radiationless electromagnetic interference: evanescent-field lenses and perfect focusing.," *Science (New York, N.Y.)*, vol. 317, pp. 927–9, Aug. 2007.

[4] Z. Jacob, L. V. Alekseyev, and E. Narimanov, "Optical Hyperlens: Far-field imaging beyond the diffraction limit.," *Optics Express*, vol. 14, pp. 8247–56, Sept. 2006.

[5] E. E. Narimanov and A. V. Kildishev, "Optical black hole: Broadband omnidirectional light absorber," *Applied Physics Letters*, vol. 95, no. 4, p. 041106, 2009.

[6] I. Smolyaninov and E. Narimanov, "Metric Signature Transitions in Optical Metamaterials," *Physical Review Letters*, vol. 105, pp. 1–4, Aug. 2010.

[7] D. R. Smith, D. Schurig, and J. B. Pendry, "Negative refraction of modulated electromagnetic waves," *Applied Physics Letters*, vol. 81, no. 15, p. 2713, 2002.

[8] J. B. Pendry and D. R. Smith, "Reversing Light With Negative Refraction," *Physics Today*, vol. 57, no. 6, p. 37, 2004.

[9] H. Lamb, "On Group - Velocity," *Proceedings of the London Mathematical Society*, vol. s2-1, pp. 473–479, Jan. 1904.

[10] A. Schuster, *An Introduction to the Theory of Optics*. London: Arnold, 1904.

[11] V. G. Veselago, "The Electrodynamics Of Substances With Simultaneously Negative Values Of epsilon and mu," *Soviet Physics Uspekhi*, vol. 10, pp. 509–514, Apr. 1968.

[12] V. G. Veselago and E. E. Narimanov, "The left hand of brightness: past, present and future of negative index materials.," *Nature materials*, vol. 5, pp. 759–62, Oct. 2006.

[13] N. Garcia and M. Nieto-Vesperinas, "Left-Handed Materials Do Not Make a Perfect Lens," *Physical Review Letters*, vol. 88, pp. 1–4, May 2002.

[14] G. 't Hooft, "Comment on "Negative Refraction Makes a Perfect Lens"," *Physical Review Letters*, vol. 87, pp. 249701–249701, Nov. 2001.

[15] R. A. Shelby, D. R. Smith, and S. Schultz, "Experimental verification of a negative index of refraction.," *Science (New York, N.Y.)*, vol. 292, pp. 77–9, Apr. 2001.

[16] G. W. Milton and N.-A. P. Nicorovici, "On the cloaking effects associated with anomalous localized resonance," *Proceedings of the Royal Society A: Mathematical, Physical and Engineering Sciences*, vol. 462, no. 2074, pp. 3027–3059, 2006.

[17] J. B. Pendry, D. Schurig, and D. R. Smith, "Controlling electromagnetic fields.," *Science (New York, N.Y.)*, vol. 312, no. 5781, pp. 1780–2, 2006.

[18] U. Leonhardt, "Optical conformal mapping.," *Science (New York, N.Y.)*, vol. 312, no. 5781, pp. 1777–80, 2006.

[19] V. M. Shalaev, W. Cai, U. K. Chettiar, H.-K. Yuan, A. K. Sarychev, V. P. Drachev, and A. V. Kildishev, "Negative index of refraction in optical metamaterials.," *Optics letters*, vol. 30, pp. 3356–8, Dec. 2005.

[20] S. Zhang, W. Fan, N. Panoiu, K. Malloy, R. Osgood, and S. Brueck, "Experimental Demonstration of Near-Infrared Negative-Index Metamaterials," *Physical Review Letters*, vol. 95, pp. 1–4, Sept. 2005.

[21] U. K. Chettiar, A. V. Kildishev, H.-K. Yuan, W. Cai, S. Xiao, V. P. Drachev, and V. M. Shalaev, "Dual-band negative index metamaterial: double negative at 813 nm and single negative at 772 nm.," *Optics letters*, vol. 32, pp. 1671–3, June 2007.

[22] V. A. Podolskiy and E. E. Narimanov, "Near-sighted superlens.," *Optics letters*, vol. 30, pp. 75–7, Jan. 2005.

[23] M. Notomi, "Theory of light propagation in strongly modulated photonic crystals: Refractionlike behavior in the vicinity of the photonic band gap," *Physical Review B*, vol. 62, pp. 10696–10705, Oct. 2000.

[24] C. Luo, S. Johnson, J. Joannopoulos, and J. Pendry, "All-angle negative refraction without negative effective index," *Physical Review B*, vol. 65, pp. 2–5, May 2002.

[25] P. V. Parimi, W. T. Lu, P. Vodo, and S. Sridhar, "Photonic crystals: imaging by flat lens using negative refraction.," *Nature*, vol. 426, p. 404, Nov. 2003.

[26] E. Schonbrun, T. Yamashita, W. Park, and C. Summers, "Negative-index imaging by an index-matched photonic crystal slab," *Physical Review B*, vol. 73, pp. 1–6, May 2006.

[27] J. A. Kong, *Electromagnetic Wave Theory*. Cambridge: EMW, 2000.

[28] P. Belov, "Backward waves and negative refraction in uniaxial dielectrics with negative dielectric permittivity along the anisotropy axis," *Microwave and Optical Technology Letters*, vol. 37, pp. 259–263, May 2003.

[29] D. R. Smith, P. Kolinko, and D. Schurig, "Negative refraction in indefinite media," *Journal of the Optical Society of America B*, vol. 21, no. 5, p. 1032, 2004.

[30] V. A. Podolskiy and E. Narimanov, "Strongly anisotropic waveguide as a nonmagnetic left-handed system," *Physical Review B*, vol. 71, pp. 2–5, May 2005.

[31] T. Dumelow, J. da Costa, and V. Freire, "Slab lenses from simple anisotropic media," *Physical Review B*, vol. 72, pp. 1–8, Dec. 2005.

[32] I. Shadrivov, A. Sukhorukov, and Y. Kivshar, "Guided modes in negative-refractive-index waveguides," *Physical Review E*, vol. 67, pp. 1–4, May 2003.

[33] L. V. Alekseyev and E. Narimanov, "Slow light and 3D imaging with nonmagnetic negative index systems," *Optics Express*, vol. 14, no. 23, p. 11184, 2006.

[34] T. M. Grzegorczyk, Z. M. Thomas, and J. A. Kong, "Inversion of critical angle and Brewster angle in anisotropic left-handed metamaterials," *Applied Physics Letters*, vol. 86, no. 25, p. 251909, 2005.

[35] L. D. Landau, E. M. Lifshitz, and L. P. Pitaevskii, *Electrodynamics of Continuous Media*. Oxford: Reed Ltd., second ed., 1984.

[36] R. Merlin, "Metamaterials and the LandauâĂŞLifshitz permeability argument: Large permittivity begets high-frequency magnetism," *Proceedings of the National Academy of Sciences*, vol. 106, p. 1693, Feb. 2009.

[37] V. M. Agranovich, Y. Shen, R. Baughman, and A. Zakhidov, "Linear and nonlinear wave propagation in negative refraction metamaterials," *Physical Review B*, vol. 69, pp. 1–7, Apr. 2004.

[38] V. M. Agranovich and Y. N. Gartstein, *Spatial Dispersion, Polaritons, and Negative Refraction*, pp. 95–132. Springer, 2007.

[39] E. Shamonina, V. Kalinin, K. Ringhofer, and L. Solymar, "Imaging, compression and Poynting vector streamlines for negative permittivity materials," *Electronics Letters*, vol. 37, no. 20, p. 1243, 2001.

[40] S. A. Ramakrishna, J. B. Pendry, M. C. K. Wiltshire, and W. J. Stewart, "Imaging the near field," *Journal of Modern Optics*, vol. 50, pp. 1419–1430, Jan. 2003.

[41] X. Chen, M. He, Y. Du, W. Wang, and D. Zhang, "Negative refraction: An intrinsic property of uniaxial crystals," *Physical Review B*, vol. 72, pp. 1–4, Sept. 2005.

[42] Y. Du, M. He, X. Chen, W. Wang, and D. Zhang, "Uniaxial crystal slabs as amphoteric-reflecting media," *Physical Review B*, vol. 73, pp. 1–5, June 2006.

[43] J. W. Goodman, *Introduction to Fourier Optics*. San Francisco: McGraw-Hill, second ed., 1996.

[44] R. Fisher and R. Gould, "Resonance Cones in the Field Pattern of a Short Antenna in an Anisotropic Plasma," *Physical Review Letters*, vol. 22, pp. 1093–1095, May 1969.

[45] E. Arbel and L. B. Felsen, *Electromagnetic Theory and Antennas*. New York: Pergamon Press, 1963.

[46] P. Belov and Y. Hao, "Subwavelength imaging at optical frequencies using a transmission device formed by a periodic layered metal-dielectric structure operating in the canalization regime," *Physical Review B*, vol. 73, pp. 1–4, Mar. 2006.

[47] A. Hadni and X. Gerbaux, "Far IR excitation of longitudinal optical phonons in triglycine sulphate," *Ferroelectrics*, vol. 248, pp. 15–26, Oct. 2000.

[48] X. Gerbaux, M. Tazawa, and A. Hadni, "Far IR transmission measurements on triglycine sulphate (TGS), at 5K," *Ferroelectrics*, vol. 215, pp. 47–63, July 1998.

[49] M. Schubert, T. Tiwald, and C. Herzinger, "Infrared dielectric anisotropy and phonon modes of sapphire," *Physical Review B*, vol. 61, pp. 8187–8201, Mar. 2000.

[50] W. Boyle, A. Brailsford, and J. Galt, "Dielectric Anomalies and Cyclotron Absorption in the Infrared: Observations on Bismuth," *Physical Review*, vol. 109, pp. 1396–1398, Feb. 1958.

[51] W. Boyle and A. Brailsford, "Far Infrared Studies of Bismuth," *Physical Review*, vol. 120, pp. 1943–1949, Dec. 1960.

[52] V. D. Kulakovskii and V. D. Egorov, "Plasma reflection in bismuth and bismuth-antimony alloys," *Sov. Phys. Solid State*, vol. 17, no. 7, pp. 1368–1371, 1974.

[53] V. S. Edelman, "Electrons in bismuth," *Adv. Phys.*, vol. 25, p. 555, 1976.

[54] F. Y. Yang, K. Liu, K. Hong, D. H. Reich, P. C. Searson, and C. L. Chien, "Large magnetoresistance of electrodeposited single-crystal bismuth thin films," *Science*, vol. 284, p. 1335, 1999.

[55] E. Gerlach, P. Grosse, M. Rautenberg, and W. Senske, "Dynamical conductivity and plasmon excitation in bi," *Phys. Stat. Sol. (b)*, vol. 75, p. 553, 1976.

[56] G. Shvets, "Photonic approach to making a material with a negative index of refraction," *Physical Review B*, vol. 67, pp. 1–8, Jan. 2003.

[57] D. Korobkin, Y. Urzhumov, and G. Shvets, "Enhanced near-field resolution in midinfrared using metamaterials," *Journal of the Optical Society of America B*, vol. 23, no. 3, p. 468, 2006.

[58] M. Born and E. Wolf, *Principles of Optics*, ch. 15. New York, NY: Pergamon, 6 ed., 1980.

[59] V. A. Podolskiy, L. V. Alekseyev, and E. E. Narimanov, "Strongly anisotropic media: the THz perspectives of left-handed materials," *Journal of Modern Optics*, vol. 52, pp. 2343–2349, Nov. 2005.

[60] R. Wangberg, J. Elser, E. E. Narimanov, and V. A. Podolskiy, "Nonmagnetic nanocomposites for optical and infrared negative-refractive-index media," *Journal of the Optical Society of America B*, vol. 23, no. 3, p. 498, 2006.

[61] D. O. S. Melville and R. J. Blaikie, "Experimental comparison of resolution and pattern fidelity in single- and double-layer planar lens lithography," 2006.

[62] A. J. Hoffman, L. Alekseyev, S. S. Howard, K. J. Franz, D. Wasserman, V. A. Podolskiy, E. E. Narimanov, D. L. Sivco, and C. Gmachl, "Negative refraction in semiconductor metamaterials.," *Nature materials*, vol. 6, pp. 946–50, Dec. 2007.

[63] P. B. Johnson and R. W. Christy, "Optical Constants of the Noble Metals," *Physical Review B*, vol. 6, pp. 4370–4379, Dec. 1972.

[64] F. Gervais, "Sapphire (Al_2O_3)," in *Handbook of Optical Constants of Solids II* (E. D. Palik, ed.), pp. 761–775, San Diego: Academic Press, 1991.

[65] L. V. Alekseyev, E. E. Narimanov, T. Tumkur, H. Li, Y. A. Barnakov, and M. A. Noginov, "Uniaxial epsilon-near-zero metamaterial for angular filtering and polarization control," *Applied Physics Letters*, vol. 97, no. 13, p. 131107, 2010.

[66] F. D. M. Haldane, "Electromagnetic Surface Modes at Interfaces with Negative Refractive Index make a "Not-Quite-Perfect" Lens," *Interfaces*, vol. 0708, p. 4, June 2002.

[67] P. Belov, C. Simovski, and P. Ikonen, "Canalization of subwavelength images by electromagnetic crystals," *Physical Review B*, vol. 71, pp. 1–4, May 2005.

[68] K. J. Webb and M. Yang, "Subwavelength imaging with a multilayer silver film structure.," *Optics letters*, vol. 31, pp. 2130–2, July 2006.

[69] A. Salandrino and N. Engheta, "Far-field subdiffraction optical microscopy using metamaterial crystals: Theory and simulations," *Physical Review B*, vol. 74, pp. 1–5, Aug. 2006.

[70] E. Purcell, "Spontaneous emission probabilities at radio frequencies," *Phys. Rev.*, vol. 69, p. 681, 1946.

[71] R. McPhedran, L. Botten, J. McOrist, a. Asatryan, C. de Sterke, and N. Nicorovici, "Density of states functions for photonic crystals," *Physical Review E*, vol. 69, pp. 1–16, Jan. 2004.

[72] E. Yablonovitch, T. J. Gmitter, and R. Bhat, "Inhibited and Enhanced Spontaneous Emission from Optically Thin AlGaAs/GaAs Double Heterostructures," *Physical Review Letters*, vol. 61, pp. 2546–2549, Nov. 1988.

[73] G. Nienhuis and C. Alkemade, "Atomic radiative transition probabilities in a continuous medium," *Physica B+C*, vol. 81, pp. 181–188, Jan. 1976.

[74] G. Ford and W. Weber, "Electromagnetic interactions of molecules with metal surfaces," *Physics Reports*, vol. 113, no. 4, pp. 195–287, 1984.

[75] W. Lukosz and R. E. Kunz, "Light emission by magnetic and electric dipoles close to a plane interface I: Total radiated power," *Journal of the Optical Society of America*, vol. 67, p. 1607, Dec. 1977.

[76] I. Pockrand, A. Brillante, and D. M\"obius, "Decay of excited molecules near a metal surface," *Chemical Physics Letters*, vol. 69, no. 3, pp. 499–504, 1980.

[77] W. L. Barnes, "Fluorescence near interfaces: The role of photonic mode density," *Journal of Modern Optics*, vol. 45, no. 4, pp. 661 – 699, 1998.

[78] Z. Jacob, I. Smolyaninov, and E. Narimanov, "Broadband Purcell effect: Radiative decay engineering with metamaterials," pp. 1–13, 2009.

[79] R. R. Chance, A. Prock, and R. Silbey, *Molecular Fluorescence and Energy Transfer Near Interfaces*, vol. 37 of *Advances in Chemical Physics*, pp. 1–65. Hoboken, NJ, USA: John Wiley & Sons, Inc., Jan. 1978.

[80] J. D. Jackson, *Classical electrodynamics*. New York, NY: Wiley, 3rd ed. ed., 1999.

[81] A. Alu and N. Engheta, "Guided Modes in a Waveguide Filled With a Pair of Single-Negative (SNG), Double-Negative (DNG), and/or Double-Positive (DPS) Layers," *IEEE Transactions on Microwave Theory and Techniques*, vol. 52, pp. 199–210, Jan. 2004.

[82] W. Spitzer, D. Kleinman, and D. Walsh, "Infrared Properties of Hexagonal Silicon Carbide," *Physical Review*, vol. 113, pp. 127–132, Jan. 1959.

[83] A. Karalis, E. Lidorikis, M. Ibanescu, J. Joannopoulos, and M. Soljačić, "Surface-Plasmon-Assisted Guiding of Broadband Slow and Subwavelength Light in Air," *Physical Review Letters*, vol. 95, pp. 1–4, Aug. 2005.

[84] J. E. Sipe and G. I. Stegeman, *Nonlinear optical response of metal surfaces*, p. 661. Amsterdam: North-Holland, 1982.

[85] J. B. Khurgin, "Optical buffers based on slow light in electromagnetically induced transparent media and coupled resonator structures: comparative analysis," *Journal of the Optical Society of America B*, vol. 22, no. 5, p. 1062, 2005.

[86] M. Kafesaki, I. Tsiapa, N. Katsarakis, T. Koschny, C. M. Soukoulis, and E. N. Economou, "Left-handed metamaterials: The fishnet structure and its variations," *Physical Review B*, vol. 75, pp. 1–9, June 2007.

[87] H. Liu and K. J. Webb, "Subwavelength imaging with nonmagnetic anisotropic bilayers," *Optics Letters*, vol. 34, no. 14, pp. 2243–2245, 2009.

[88] N. Fang, H. Lee, C. Sun, and X. Zhang, "Sub-diffraction-limited optical imaging with a silver superlens.," *Science (New York, N.Y.)*, vol. 308, pp. 534–7, Apr. 2005.

[89] G. Dolling, C. Enkrich, M. Wegener, C. M. Soukoulis, and S. Linden, "Simultaneous negative phase and group velocity of light in a metamaterial.," *Science (New York, N.Y.)*, vol. 312, pp. 892–4, May 2006.

[90] S. Durant, Z. Liu, J. M. Steele, and X. Zhang, "Theory of the transmission properties of an optical far-field superlens for imaging beyond the diffraction limit," *Journal of the Optical Society of America B*, vol. 23, no. 11, p. 2383, 2006.

[91] M. Tonouchi, "Cutting-edge terahertz technology," *Nature Photonics*, vol. 1, pp. 97–105, Feb. 2007.

[92] A. Zumbusch, G. Holtom, and X. Xie, "Three-Dimensional Vibrational Imaging by Coherent Anti-Stokes Raman Scattering," *Physical Review Letters*, vol. 82, pp. 4142–4145, May 1999.

[93] S. W. Hell, "Far-field optical nanoscopy.," *Science (New York, N.Y.)*, vol. 316, pp. 1153–8, May 2007.

[94] R. W. Boyd, *Nonlinear Optics*. San Diego: Academic Press, second ed., 2003.

[95] J. W. Goodman, "Digital Image Formation From Electronically Detected Holograms," *Applied Physics Letters*, vol. 11, no. 3, p. 77, 1967.

[96] U. Schnars and W. Jüptner, "Direct recording of holograms by a CCD target and numerical reconstruction.," *Applied optics*, vol. 33, pp. 179–81, Jan. 1994.

[97] E. Cuche, P. Marquet, and C. Depeursinge, "Simultaneous amplitude-contrast and quantitative phase-contrast microscopy by numerical reconstruction of Fresnel off-axis holograms.," *Applied optics*, vol. 38, pp. 6994–7001, Dec. 1999.

[98] R. Lanz and P. Muralt, "Bandpass filters for 8 GHz using solidly mounted bulk acoustic wave resonators.," *IEEE transactions on ultrasonics, ferroelectrics, and frequency control*, vol. 52, pp. 936–46, June 2005.

[99] M. B. Assouar, O. Elmazria, P. Kirsch, P. Alnot, V. Mortet, and C. Tiusan, "High-frequency surface acoustic wave devices based on AlN/diamond layered structure realized using e-beam lithography," *Journal of Applied Physics*, vol. 101, no. 11, p. 114507, 2007.

[100] X. Chen and S. R. Brueck, "Imaging interferometric lithography: approaching the resolution limits of optics.," *Optics letters*, vol. 24, pp. 124–6, Feb. 1999.

[101] Y. Kuznetsova, A. Neumann, and S. R. Brueck, "Imaging interferometric microscopy-approaching the linear systems limits of optical resolution.," *Optics express*, vol. 15, pp. 6651–63, May 2007.

[102] P. Bhattacharya, X. H. Su, S. Chakrabarti, G. Ariyawansa, and A. G. U. Perera, "Characteristics of a tunneling quantum-dot infrared photodetector operating at room temperature," *Applied Physics Letters*, vol. 86, no. 19, p. 191106, 2005.

[103] R. M. Williams, J. F. Kelly, J. S. Hartman, S. W. Sharpe, M. S. Taubman, J. L. Hall, F. Capasso, C. Gmachl, D. L. Sivco, J. N. Baillargeon, and A. Y. Cho, "Kilohertz linewidth from frequency-stabilized mid-infrared quantum cascade lasers," *Optics Letters*, vol. 24, p. 1844, Dec. 1999.

[104] C.-A. Guérin, B. Gralak, and A. Tip, "Singularity of the dyadic Green's function for heterogeneous dielectrics," *Physical Review E*, vol. 75, pp. 0–4, May 2007.

[105] S. Lee, J. Boersma, C. Law, and G. Deschamps, "Singularity in Green's function and its numerical evaluation," *IEEE Transactions on Antennas and Propagation*, vol. 28, pp. 311–317, May 1980.

[106] G. Gao, C. Torres-Verdin, and T. M. Habashy, "Analytical techniques to evaluate the integrals of 3d and 2d spatial dyadic Green's functions," *Progress In Electromagnetics Research*, vol. 52, pp. 47–80, 2005.

[107] N. N. Boustany, R. Drezek, and N. V. Thakor, "Calcium-induced alterations in mitochondrial morphology quantified in situ with optical scatter imaging.," *Biophysical journal*, vol. 83, pp. 1691–700, Sept. 2002.

[108] C. S. Mulvey, A. L. Curtis, S. K. Singh, and I. J. Bigio, "Elastic Scattering Spectroscopy as a Diagnostic Tool for Apoptosis in Cell Cultures," *IEEE Journal of Selected Topics in Quantum Electronics*, vol. 13, no. 6, pp. 1663–1670, 2007.

[109] F. Ignatovich and L. Novotny, "Real-Time and Background-Free Detection of Nanoscale Particles," *Physical Review Letters*, vol. 96, pp. 1–4, Jan. 2006.

[110] N. I. Zheludev, "A Roadmap for Metamaterials," *Optics and Photonics News*, vol. 22, p. 30, Mar. 2011.

[111] L. Novotny and B. Hecht, *Principles Of Nano-optics*. New York: Cambridge University Press, 2006.

[112] R. J. Glauber and M. Lewenstein, "Quantum optics of dielectric media," *Physical Review A*, vol. 43, no. 1, pp. 467–491, 1991.